Modelling of the interaction between radiation and the atmospheric composition with ICON-ART

Zur Erlangung des akademischen Grades eines

DOKTORS DER NATURWISSENSCHAFTEN

von der Fakultät für Physik des
Karlsruher Instituts für Technologie

genehmigte

DISSERTATION

von

Jennifer Jasmin Schröter
aus Duisburg

Referent: Prof. Dr. Peter Braesicke

Korreferent: Prof. Dr. Johannes Orphal

Tag der mündlichen Prüfung: 22.12.2017

Abstract

This thesis presents the modelling of the interaction of radiation and the composition of the Earth's atmosphere with the next generation modelling system ICON-ART. The ICOsahedral Non hydrostatic model with Aerosols and Reactive Trace gases (ICON-ART) provides a suitable environment for atmospheric composition studies on weather and climate time scales.

Most global climate models or numerical weather prediction models use simplifications in solving the radiative transfer equation to save computational time. In this thesis, the validation of a more advanced module for solving the radiative transfer equation is presented. This module allows a consistent treatment of the actinic flux calculation and also the radiative net flux calculation. For the first time, photolysis rate calculations are performed with the technique of local grid refinement of ICON. For validation, aircraft campaign data are compared to ICON-ART simulations on a statistical basis. Furthermore, the question on the quantification of the radiative impact of clouds on photolysis rates is addressed.

The second part of this thesis focuses on the radiative impact of water vapour and ozone on the atmosphere. Here, AMIP type integrations using a simplified chemistry scheme in conjunction with the climate physics configuration are performed and analysed in comparison to ERA-Interim. Two different simulations are used: The interactive simulation, where modelled ozone is coupled back to the radiation scheme and the non-interactive simulation that uses a default background climatology of ozone. Additionally, a chemical source term for water vapour for the interactive simulation is introduced. For the interactive and non-interactive simulation, the water vapour tape recorder is investigated as a measure of tropical upwelling changes in the atmospheric dynamics. Additionally, the seasonal evolution and latitudinal distribution of age of air is studied.

Net flux, calculated with the validated module for photolysis rate calculations is used for shortwave heating rate calculations in a consistent way. The further development of ICON-ART allows for the usage of these calculations in climate integrations. The results for the standard radiation module of ICON are compared to the results of this advanced approach. Changes in the age of air tracer indicate that the ICON-ART model benefits from this development. The improved representation of the stratospheric overturning circulation by interactive heating rate calculations is discussed in the last chapter of this thesis.

Contents

1 Introduction

Over the past decades, much effort has been undertaken to achieve a better understanding of the changing climate of the Earth's atmosphere (IPCC, 2013; Kley et al., 2000). The climate is influenced by the fundamental physical principle of the global radiative energy balance. Over the last decades, changes in the global climate result from a small imbalance ($0.58 \pm 0.15\,\mathrm{W\,m^{-2}}$ for the years 2005–2010) in the incoming solar radiation and the emitted thermal radiation of $240\,\mathrm{W\,m^{-2}}$ (e.g. Hansen et al., 2011; Loeb et al., 2012; Stephens et al., 2012). The atmosphere is an important component for the radiative balance of the Earth system. The atmospheric composition, the thermal and chemical structure of the atmosphere interacts with downwelling radiation reaching the surface and upwelling radiation, originating from terrestrial emission.

Modelling the Earth's atmosphere with the individual components of radiation and trace gas constituents has always been challenging (Arblaster et al., 2014, WMO Assessment 2014). Both components are closely connected to each other. Each component is constraint by the main physical laws of radiation, motion and thermodynamics. However, the connection between radiation and the atmospheric composition are of such high complexity that an answer to the prominent question on "why, exactly, do models respond differently when forced similarly" is still not fully answered (Taylor et al., 2012). A similar question on how the UTLS region is able to affect the climate variability is also under current discussion (Gerber and Manzini, 2016). Most atmospheric models underestimate global mean cooling rates in the lower stratosphere, (Arblaster et al., 2014). Deviations are caused by biases in the ozone trends (e.g. Solomon et al., 2012; Santer et al., 2013) as well as errors in the stratospheric water vapour distribution (e.g. Gettelman et al., 2010; Maycock et al., 2014). The third source of possible errors lies within the radiation codes used by the different models, e.g. Forster et al. (2011).

Water vapour and ozone are two of the most important trace gases in the atmosphere with feedback on the radiation and dynamics. Both substances play a major role in the upper troposphere and lower stratosphere (UTLS) region. Water vapour shows strong absorption bands in the infrared wavelength region and influences the temperature throughout all layers of the atmosphere. For example, if water vapour concentrations change, temperature changes are induced and thus a pressure gradient force is evoked. The thermal wind induction and

conservation of the continuity equation leads to changes in the wind fields. Consequently, water vapour has a strong impact on the dynamics and vice versa. Observations have shown that the volume mixing ratio of stratospheric water vapour increased by 2 ppmv since 1950 (e.g. Rosenlof et al., 2001). Nowadays, mean volume mixing ratios of stratospheric water vapour reach about 4 ppmv to 6 ppmv (e.g. Kley et al., 2000; de Forster and Shine, 1999). This increase is still subject of extensive observations and model studies. Water vapour can enter the stratosphere in many different ways, but large scale circulation patterns, including upwelling air in the tropics and poleward circulations of the Brewer-Dobson circulation have the largest contribution.

Furthermore, deep convection of water vapour leads to cloud formation. Clouds also strongly influence the radiation budget of the Earth's atmosphere. Nevertheless, the quantification of enhancing and shielding effects of radiation due to presence of clouds at different wavelengths is still unclear and under current discussion and investigation (e.g. Erle et al., 1995; Trenberth et al., 2009; Kato et al., 2016). The solution of the radiative transfer equation is strongly influenced by the presence of clouds. However, in the past years, only a few studies focused on the reduction and enhancement effects of clouds in the atmosphere and on radiative quantities like the actinic flux (e.g. Kley et al., 2000; Tie et al., 2003; Liu et al., 2006, 2009). The major chemical source of stratospheric water vapour is the photodissociation of methane. Chemical processes in the UTLS region are also strongly affected by water vapour itself. Water vapour is a key chemical constituent determining the concentration of stratospheric ozone by catalytic loss cycles (e.g. Arblaster et al., 2014). Ozone in the UTLS region has also a strong influence on the radiation budget. Ozone shows strong absorption bands in the infrared wavelength region, similar to water vapour. Additionally, the photodissociation of ozone in the ultraviolet wavelength region determines many chemical processes in the stratosphere (e.g. Kley et al., 2000). Intensive model comparison studies, e.g. Eyring et al. (2006), have shown that it is of high importance to include feedback processes of chemical composition changes on the radiation and dynamics. The close connection of water vapour and ozone to chemical mechanisms, radiation and dynamics is important for the understanding of past and future climate changes.

Weather and climate modelling systems like ICON-ART (Rieger et al., 2015; Weimer et al., 2017) are an important tool to address these kind of questions and to investigate not fully understood mechanisms. ICON (Zängl et al., 2015) is a joint development of the Deutscher Wetterdienst (DWD) and the Max Planck Institute for Meteorology (MPI-M). The dynamical core of ICON is based on the non-hydrostatic formulation of the vertical momentum equation. ART is an additional module for ICON, developed at the Karlsruhe Institute of Technology. It contributes to the goal of a unified global next generation modelling system with a variety of applications in the field of atmospheric composition

sciences. ICON-ART extends the numerical weather and climate prediction system ICON with (gas phase) chemistry, aerosol dynamics and related feedback processes (Schröter et al., 2018).

The development of ICON-ART started on the basis of a next generation weather forecasting system. Two physics configurations can be used for ICON-ART. One configuration is designed for the short time scales, the other for climate integrations. Both configurations share the same dynamical core. Thus, simulations ranging from a few hours to hundreds of years are more consistent. The flexible tracer framework is an essential technical achievement to ensure features of ART to be combined with the weather and the climate physics configurations. Further scientific developments of ICON-ART which were performed in the scope of this thesis include tracer parameterisations and the coupling between the ART module and the climate physics configuration. Now it is possible to use the physical configuration for short term numerical weather predictions and the climate configuration with the ART module. Both developments, the physics coupling and the new tracer framework were also mandatory for other studies, e.g. Eckstein et al. (2017); Eckstein (2017) and Diekmann (2017). Within the scope of this thesis, the interaction between radiation and the atmospheric composition is investigated with ICON-ART. The interaction is addressed by the two radiative quantities of the actinic flux and net flux. The first one determines the frequency of photodissociation of molecules, the photolysis rate. These photolysis rates have a strong impact on the chemical composition of the Earth's atmosphere. The interactive calculation of photolysis rates connects aspects of the radiation budget and the chemical composition.

This introduction is followed by the theoretical background for atmospheric radiation and feedbacks in chapter two. In chapter three, a brief technical description of ICON-ART with the main focus of the new developments and composition modules is given. Chapter four presents a new way to quantify enhancement and reduction effects of photolysis rates by clouds with ICON-ART. For the first time, photolysis rates are simulated by ICON-ART, including the technique of local grid refinement in a global domain. ICON-ART photolysis rate calculations are validated with measurements of the TORERO aircraft campaign. This part of the thesis not only discusses the quantification of the cloud impact on the radiation but also shows the applicability of simulated photolysis rates in the model. The reasonable calculation of photolysis rate calculation is a prerequisite for global chemistry composition modelling. Chapter five investigates the interaction between the chemical composition and atmospheric dynamics. This part focuses on determining effects of water vapour and ozone on large scale dynamics within the Earth's atmosphere. Here, climate integrations, similar to AMIP experiments (Gates et al., 1999), are performed including the time span from 1979 to 2009. Furthermore, the interaction between radiation and the atmospheric composition

is addressed by the investigation of the impact of changing short wave heating rates. Here, the same module used for photolysis rate calculations provides the simulation of short wave heating rates. By the deposited amount of radiation in the different model layers, also defined as the convergence of the radiative net flux, temperatures change. The last chapter of this thesis discusses the influence of altered heating rates on the stratospheric dynamics. This thesis concludes with a summary and an outlook.

2 Theoretical background

2.1 Radiation budget and trace gas impact

The Earth's radiation budget is of high importance regarding many questions from weather to climate phenomena. Source of most of the energy that reaches the Earth's surface originates from the Sun. The incoming total solar irradiance (TSI) at the top of the atmosphere (TOA) can be measured and is about $1360\,\mathrm{W\,m^{-2}}$ (IPCC, 2013). This value is called the solar constant S_0. Assuming the Earth's surface is a sphere, the annual mean irradiance is about $340\,\mathrm{W\,m^{-2}}$, where the TSI is homogeneously distributed over the area of $4\pi R_{\mathrm{E}}^2$, with R_{E} is the Earth's radius.
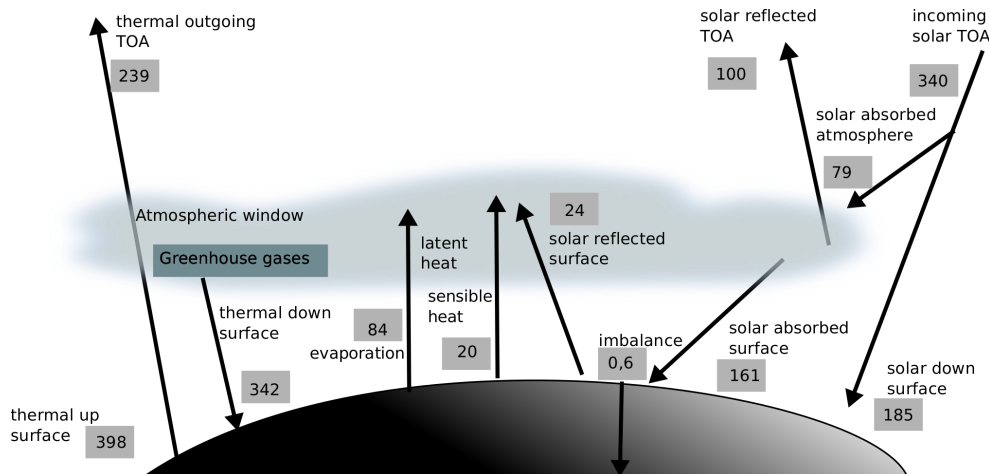
Figure 2.1: Radiation budget of the Earth's atmosphere. This figure is adapted from IPCC (2013).

Figure 2.1 summarises schematically the absorption and emission processes in the Earth's atmosphere and at the surface. The immediate backscattering process accounts for approximately $100\,\mathrm{W\,m^{-2}}$. The global mean surface temperature can be estimated to be $288\,\mathrm{K}$ ($\approx 15\,^{\circ}\mathrm{C}$) (Hansen et al., 2010). Assuming the Earth's surface being a black body, the

theoretically governed temperature of $-18\,^{\circ}\text{C}$ differs nearly by $30\,^{\circ}\text{C}$ with respect to the measured one. For black body emissions, Planck's law is applied:

$$B\left(T,\nu\right) = \frac{8\pi h\nu^3}{c^2} \frac{1}{\exp\left(\frac{h\nu}{k_{\text{B}}T}\right) - 1} \tag{2.1}$$

Here, k_{B} is the Boltzmann constant, h the Planck constant, ν the frequency of the radiation, T the temperature of the black body and c the speed of light.

The radiation of a black body is defined by the Stefan-Boltzmann law:

$$\kappa = \epsilon_S\,\sigma\,T_S^4 \tag{2.2}$$

With ϵ_S the emissivity ($\epsilon_S = 1$ for a black body), σ the Stefan-Boltzmann constant and T_S the black body's temperature. With the assumption of energy conservation of the radiation budget, neglecting the influence of the atmosphere, the energy balance is described by the following equation:

$$\epsilon_S\,\sigma\,T_S^4 = (1 - A)\frac{S_0}{4} \tag{2.3}$$

with A as the albedo. By using the albedo for grassland with $A = 0.3$, $S_0 = 1360$, equation 2.3 leads to a surface temperature of about $T_{\text{S}} = 255\,\text{K}$. In contrast to that, the measured surface temperature is approximately $288\,\text{K}$ (e.g. Hansen et al., 2010). This leads to the conclusion that an additional heating term is needed for a realistic calculation of the surface temperature. The theoretical sketch shows the importance of the Earth's atmosphere for the global energy budget and especially the surface temperature. Trace gases in the atmosphere accounting for longwave radiation interaction are combined in the term greenhouse gases (GHG). Longwave radiation emitted by the surface is absorbed and re-emitted by GHG. This process leads again to emission in all directions. Additional heating is gained from the downward oriented longwave emission of GHG, leading to an increase of the Earth's surface temperature by $30\,\text{K}$.

2.1.1 Importance of greenhouse gases

The trace gases carbon dioxide (CO_2), methane (CH_4) and nitrous oxide (N_2O) are the major contributors to the defined GHG. The institution of Intergovernmental Panel on Climate Change (IPCC) introduced radiative forcing (RF) as a measure for the (anthropologically) induced radiative heating, given in units of $\text{W}\,\text{m}^{-2}$. The highest RF is estimated for CO_2 to be $(1.82 \pm 0.19)\,\text{W}\,\text{m}^{-2}$, the highest contribution to the total RF for all well mixed GHG, which is estimated to be $(2.83 \pm 0.29)\,\text{W}\,\text{m}^{-2}$ (IPCC, 2013). The estimates for CH_4 and N_2O are smaller, $(0.48 \pm 0.05)\,\text{W}\,\text{m}^{-2}$ and $(0.17 \pm 0.03)\,\text{W}\,\text{m}^{-2}$ respectively. Tropospheric

ozone (O_3) contributes with $(0.35 \pm 0.25)\,\text{W}\,\text{m}^{-2}$ and water vapour with $(0.07 \pm 0.02)\,\text{W}\,\text{m}^{-2}$. The measure is defined relatively to a pre-industrial setting of the atmospheric conditions in order to determine anthropogenic effects to the greenhouse effect. Both species, ozone and water vapour, are not defined as classical GHG, also represented by relatively small measures of the anthropogenic RF. But despite the anthropogenically induced increase of both substances and the resulting RF, both species do contribute to the global radiation budget significantly due to the strong longwave absorption bands.

2.1.2 Longwave absorption of ozone and water vapour

The following theoretical overview is mainly based on Petty (2004). The absorption of electromagnetic radiation follows quantum mechanical rules of selection. Based on the electron configuration of an atom or molecule, radiation of a specific wavelength can induce transitions in the electronic state, rotational changes, vibrational changes of energy or a combination of these. The dominant vibrational transitions for longwave absorption and emission are between $1\,\mu\text{m}$ and $20\,\mu\text{m}$. The theoretical model that holds for diatomic molecules is the model of a non-rigid rotor. The restoring force F between two atoms is given by:

$$F = -k(r - r')$$

(2.4)

with k an analogue to a classical spring constant and $r - r'$ the relative separation to equilibrium. In classical mechanics, the vibration frequency ν' is derived from the model of an harmonic oscillator:

$$\nu' = \frac{1}{2\pi}\sqrt{\frac{k}{m'}}$$

(2.5)

with m' the reduced mass. However, in the quantum mechanical model the energy states are quantised, thus the vibrational quantum number becomes

$$\nu = (j_\nu \pm \frac{1}{2})\nu'$$

(2.6)

$$j_\nu \in \mathbb{N}$$

(2.7)

with j_ν the vibrational quantum number.

For polyatomic molecules, this model still applies but gets more complicated. The possible vibrational motions are increased with respect to a diatomic molecule. For water vapour and ozone, there are three modes leading to three vibrational quantum numbers. Transitions induced by an electromagnetic field can change all three quantum numbers simultaneously. The three possible modes, symmetric stretching, bending and asymmetric string are depicted

in Figure 2.2. Due to this quantum mechanical characterisation, both molecules are strong absorbers and emitters in the thermal infrared (IR) band. For water vapour, the strong thermal infrared bands lay between 2 µm and 12 µm. The bending mode is located at 6.3 µm and the asymmetric stretch at 2.1 µm. The fundamental vibrational bands of ozone are located at 9 µm, 14.27 µm, and 9.6 µm. The region between 8 µm to 12 µm is also called the atmospheric window since the Planck function of the terrestrial thermal emission is peaking in this wavelength region. Since both molecules do have strong absorption lines in that region, both play an important role in the atmospheric radiation budget.

symmetric stretch **(a)**   asymmetric stretch **(b)**   bending **(c)**
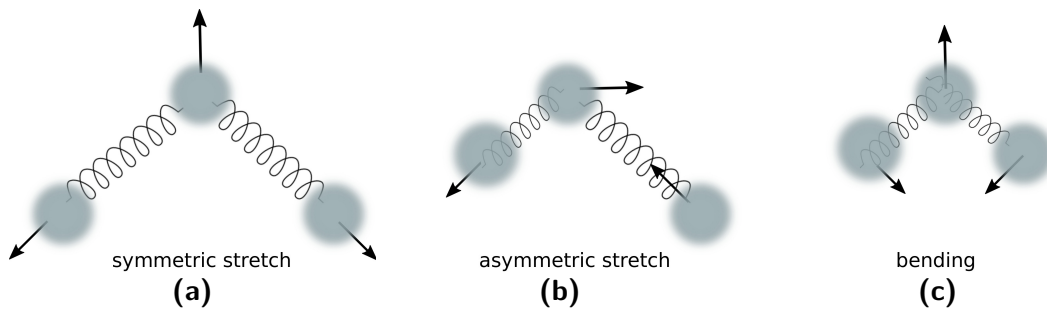
Figure 2.2: Schematic description of the three different vibrational modes of nonlinear triatomic molecules like H_2O and O_3.

The impact of the important absorbers water vapour and ozone is shown in the absorption spectra in Figure 2.3 and Figure 2.4. Without the absorption spectra shown in the bottom of Figure 2.3 and Figure 2.4, the Earth's surface temperature would approximately be 250 K, derived from the mean annual solar irradiance as seen before.

The Earth's atmosphere is transparent for the majority of visible wavelengths from 0.4 µm to 0.7 µm, expect for narrow absorption bands of oxygen and ozone. Water vapour absorbs between 5 µm to 8 µm and wavelengths higher than 20 µm. The weak absorption window between 8 µm to 12 µm is also called water vapour window. This short sketch of absorption spectra in the Earth's atmosphere shows again the high importance of water vapour and ozone for the described natural greenhouse effect.
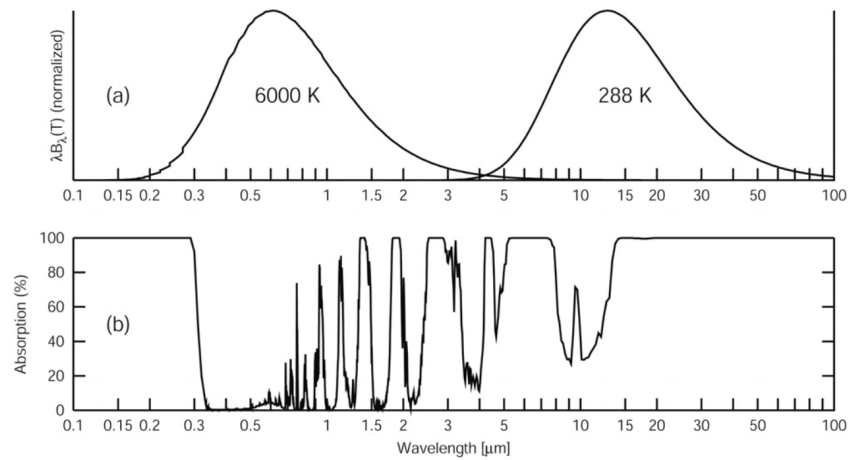
Figure 2.3: Planck functions of the TOA (left part of a) and the Earth's surface (right part of a). The bottom panel represents the clear sky absorptivity without CO_2 absorption. This figure is taken from Petty (2004).
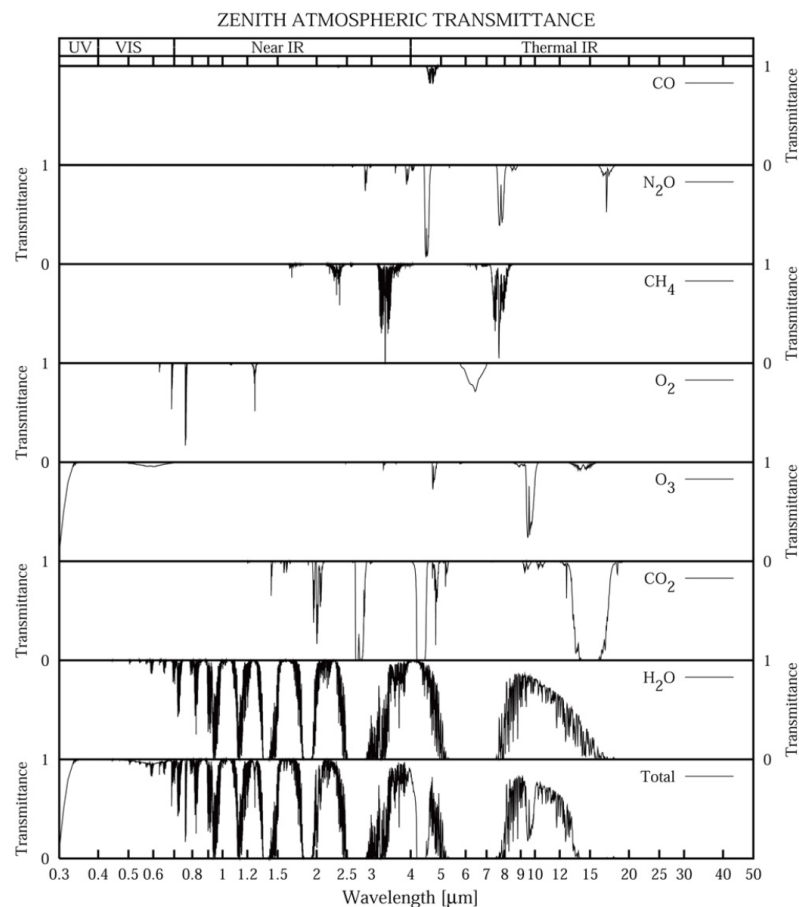
Figure 2.4: Transmittance contribution of selected trace gases, correspondent to the total absorptivity shown in Figure 2.3. This figure is taken from Petty (2004).

2.1.3 Thermal structure of the Earth's atmosphere

The vertical structure of the Earth's atmosphere is mainly defined by its vertical temperature dependency. Additionally, the atmosphere can be distinguished into two parts as depicted in Figure 2.5. These two parts are called homosphere and heterosphere. Within the homosphere, reaching up to approximately $100\,\mathrm{km}$, trace gases are assumed to be well mixed. Above, within the heterosphere, trace gases are being separated due to their different molecular mass. The homosphere can be separated into sublayers. The lowermost layer is called the troposphere. About $80\,\%$ of the total mass of the atmosphere is located in the troposphere. The troposphere is also characterised by rapid vertical mixing (Seinfeld and Pandis, 2006).

Additionally, the troposphere shows a vertical temperature profile which decreases with altitude with about $10\,\mathrm{K\,km^{-1}}$. This gradient, as well as the average height, depends on latitude. This gradient is also called adiabatic lapse rate. Following López-Puertas and Taylor (2001), the adiabatic lapse rate can be calculated with the hydrostatic assumption for dry air to:

$$\frac{g}{c_\mathrm{P}} = -\frac{\mathrm{d}T}{\mathrm{d}z} \tag{2.8}$$

with g the gravitational constant and $c_\mathrm{P} = 1000\,\mathrm{J\,K^{-1}\,kg}$ the heat capacity of dry air. Within the troposphere, convection takes place. Above the troposphere, in the stratosphere, convection stops and the adiabatic lapse rate tends to zero. Atmospheric layers are no longer cooled by water vapour absorption from the layer above since convection is the major source for high water vapour concentrations. However, an increase of the temperature within the stratosphere up to approximately $50\,\mathrm{km}$ can be observed. Photons are no longer absorbed by water vapour and propagate towards higher altitudes. The region between troposphere and stratosphere is called tropopause. Layers above the tropopause are layers which re-emit the absorbed upwelling radiation, mainly due to ozone absorption. For the emission, the black body equation can be used. Since layers above the tropopause are emitting in upward and downward direction, assuming a plane parallel atmosphere, the black body equilibrium reads as follows:

$$\epsilon T_\mathrm{Earth}^4 = 2\epsilon T_\mathrm{strat}^4 \tag{2.9}$$

with ϵ as the emissivity.

This would lead with the Earth's black body temperature of $T_\mathrm{Earth} = 250\,\mathrm{K}$ and to a temperature of the stratosphere of $T_\mathrm{strat} = 210\,\mathrm{K}$. At this point it should be noted that T_Earth is not the equivalent to the average surface temperature. It is the equivalent

temperature for the emitted infrared flux, heating the stratosphere from below. Taking only equation 2.9 into account would lead to the argument that the temperature in the stratosphere remains constant with increasing altitude. However, this is not the case in reality.

The vertical profile of the ozone concentration in the atmosphere peaks around $20\,\mathrm{km}$ due to photochemical production. As described above, ozone absorbs in the infrared spectral region. Between $0.2\,\mathrm{\mu m}$ and $0.3\,\mathrm{\mu m}$, the so called Hartley Band of ozone absorption is located. Thus, below an altitude of about $70\,\mathrm{km}$, the solar energy is converted to heat due to ozone absorption. The heating rate, following López-Puertas and Taylor (2001), can be calculated at an altitude z to

$$c_{\mathrm{P}}(z)\rho(z)\frac{\mathrm{d}T(z)}{\mathrm{d}t} = \int\limits_{0.2}^{0.3}\frac{\mathrm{d}F_\lambda(z,\Theta)}{\mathrm{d}z}\mathrm{d}\lambda \tag{2.10}$$

with $\rho(z)$ the air density, Θ the solar zenith angle and $F_\lambda(z,\Theta)$ the spectral flux of radiant energy. This flux is dependent on the ozone number density n_{O_3} by:

$$F_\lambda(z,\Theta) = F_\lambda(\infty)\exp -\int\limits_{z}^{\infty}\sigma_\lambda n_{\mathrm{O}_3}(z)\mathrm{d}z' \tag{2.11}$$

with σ_λ, the absorption cross section at wavelength λ.

This leads to a maximum of the solar heating rate by ozone absorption at $50\,\mathrm{km}$. This theoretical sketch shows one aspect on the importance of stratospheric ozone, as well as of tropospheric water vapour in the Earth's atmosphere. Following Petty (2004), water vapour contributes in the tropopause region with a cooling rate of about $0.2\,\mathrm{K\,d^{-1}}$, much smaller than the cooling rate of CO_2 of about $10\,\mathrm{K\,d^{-1}}$. The warming contribution of ozone is estimated to be about $0.5\,\mathrm{K\,d^{-1}}$ between $20\,\mathrm{km}$ and $30\,\mathrm{km}$.

This composition of cooling and heating rates due to different molecular absorption spectra, is of high importance for the understanding of the Earth's atmosphere and many processes within.

2.2 Solving the radiation field in planetary atmospheres

The description of the radiative transfer in planetary atmospheres is introduced in this section. Radiative processes which affect the transfer of energy are single scattering, multiple scattering and absorption. For the Earth's atmosphere we assume a plane parallel geometry. The following description is mainly based on Chandrasekhar (1960) and Liou (2002).

2.2.1 Beer-Bouger-Lambert Law

The radiant intensity or radiance $I_\lambda(x_1)$ which is transferred through a medium with thickness $\mathrm{d}x$, decreases if the medium is a homogeneously absorbing medium. Here λ denotes the wavelength and x_1 the location in the medium. The decrease is described by an exponential function:

$$I_\lambda(x_1) = I_\lambda(0) \exp\left(-\sigma_{a,\lambda}\right)n \tag{2.12}$$

where

$$n = \int\limits_0^{x_1} \rho \mathrm{d}s \tag{2.13}$$

with $\sigma_{a,\lambda}$ as the mass absorption cross section and ρ the column density of the material. In this case processes of scattering and absorption are neglected.
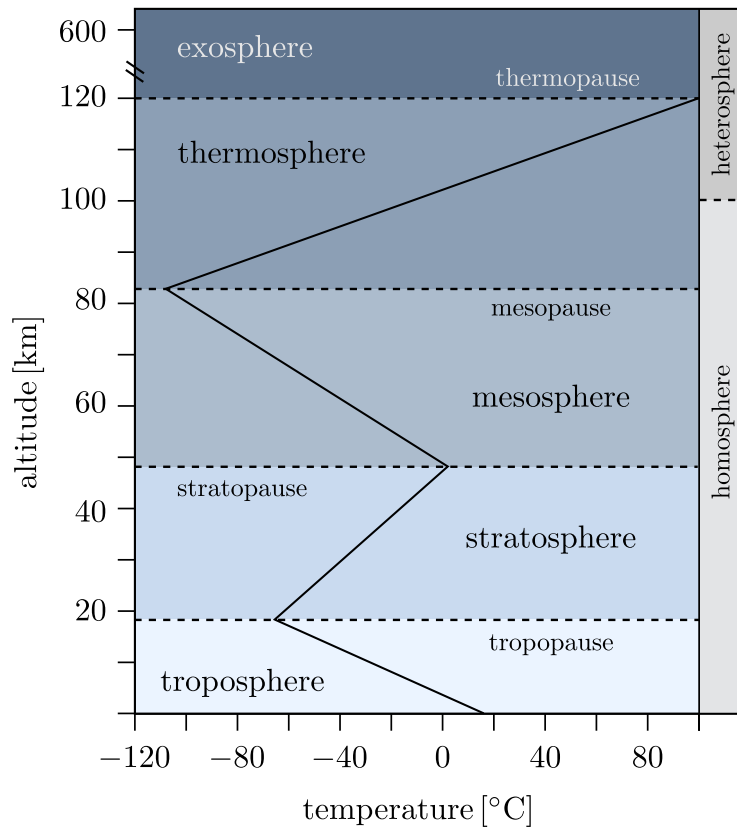
Figure 2.5: This figure is originally adapted from Dörnbrack (2012) and taken from Kiel (2016)

2.2.2 Schwarzschild equation

Assuming a beam which is propagating through a non-scattering medium, the radiant intensity is absorbed and re-emitted at the same time. If the medium is represented by a black body in thermal equilibrium, we can express the radiant intensity at location x_1 in the medium using

$$I_\lambda(x_1) = I_\lambda(0) \exp\left(-\tau_\lambda(x_1)\right) + \int\limits_0^{x_1} B_\lambda(T(x)) \exp\left(-\tau_\lambda(x_1, x)\right) \sigma_\lambda \rho \mathrm{d}x \tag{2.14}$$

gained from the so called Schwarzschild equation:

$$\frac{\mathrm{d}I_\lambda}{\lambda \rho \mathrm{d}x} = -I_\lambda + B_\lambda(T) \tag{2.15}$$

where $B_\lambda(T)$ denotes Planck's function of a black body with a given temperature T. The variable $\tau(x_1, x)$ defines the monochromatic optical thickness between to points x_1 and x in the medium. The optical thickness is defined by:

$$\tau(x_1, x) = \int\limits_x^{x_1} \sigma_\lambda \rho \mathrm{d}x' \tag{2.16}$$

2.2.3 Phase functions and scattering cross sections

The phase function is a non-dimensional parameter, which describes the radiative transfer in planetary atmospheres. The phase function $P(\cos(\theta))$ is normalised to:

$$\int\limits_0^{2\pi} \int\limits_0^{2\pi} \frac{P(\cos(\theta))}{4\pi} \sin(\theta) \mathrm{d}\theta \mathrm{d}\phi = 1 \tag{2.17}$$

with ϕ the scattering angle, the angle between the incident beam and the scattered beam. Assuming that the particle size distribution in a cloud can be described by $\frac{\mathrm{d}n(r_c)}{\mathrm{d}r_c}$ with r_c the particle size and $n(r_c)$ the number of particles with this size, one can derive the total number of particles using

$$N = \int\limits_{r_{c,1}}^{r_{c,2}} \frac{\mathrm{d}n(r_c)}{\mathrm{d}r_c} \tag{2.18}$$

The respective extinction coefficient β_e is calculated by:

$$\beta_\text{e} = \int\limits_{r_{c,1}}^{r_{c,2}} \sigma_\text{e}(r_c)\frac{\mathrm{d}n(r_c)}{\mathrm{d}r_c}\mathrm{d}r_c \tag{2.19}$$

with σ_e as the extinction cross section. In an analogous way, the scattering coefficient β_s is given by:

$$\beta_\text{s} = \int\limits_{r_{c,1}}^{r_{c,2}} \sigma_\text{s}(r_c)\frac{\mathrm{d}n(r_c)}{\mathrm{d}r_c}\mathrm{d}r_c \tag{2.20}$$

The single scattering albedo $\tilde{\omega}$ is defined as the division of the scattering coefficient and the extinction coefficient:

$$\tilde{\omega} = \frac{\beta_\text{s}}{\beta_\text{e}} \tag{2.21}$$

The single scattering albedo gives the function of an incident beam which is scattered once. In general, the extinction itself represents the loss through scattering and absorption. Thus, the relation

$$\sigma_\text{a} = \sigma_\text{s} - \sigma_\text{e} \tag{2.22}$$

holds. Here, σ_a is the total cross section, the difference of the extinction cross section and the scattering cross section.

2.2.4 Extinction of sunlight in the presence of clouds

Assuming an ideal plane parallel cloud, consistent of equally sized cloud droplets with a radius r, the extinction coefficient is calculated by:

$$\beta_\text{e} = NQ_\text{e}\pi r^2 \tag{2.23}$$

with Q_e as the extinction efficiency and N the concentration. The optical thickness of this cloud type is derived by

$$\tau^\star = \int\limits_{z_\text{bot}}^{z_\text{top}} \beta_\text{e}\mathrm{d}z \tag{2.24}$$

with z_bot and z_top as the cloud bottom and cloud top altitude. Since both, the concentration and radius of a cloud droplet are not easy to measure, the value of the liquid water path is

used instead of estimating the cloud extinction coefficient. The liquid water path is defined as

$$\text{LWP} = \int\limits_{z_\text{bot}}^{z_\text{top}} \rho_\text{w}(z)\text{d}z \tag{2.25}$$

with ρ_w the cloud water density. Following Petty (2004), the optical thickness can be approximated by

$$\tau^\star \approx \frac{3\text{LWP}}{2\rho_\text{l}r} \tag{2.26}$$

with ρ_l the density of pure water.

Since most clouds in reality show a distribution of cloud droplets with different radii, the effective cloud droplet radius is defined as

$$r_\text{eff} = \frac{\int\limits_0^\infty n(r)r^3\text{d}r}{\int\limits_0^\infty n(r)r^2\text{d}r} \tag{2.27}$$

where $n(r)$ is the number of droplets of a specific radius. The effective optical depth is then

$$\tau^\star \approx \frac{3\text{LWP}}{2\rho_\text{l}r_\text{eff}} \tag{2.28}$$

For clouds, not only containing water but also ice particles, a similar approximation can be performed using the ice water path IWP instead of the liquid water path.

2.2.5 Scattering of sunlight in plane-parallel atmospheres

Figure 2.6 represents an atmospheric grid box where a plane-parallel atmosphere is assumed. The incoming solar flux of radiation is represented by πF_0. Three beams are sketched within the grid box, marked by a, b and c. Beam a is the representation of extinction within the box:

$$\left.\frac{\text{d}I(z,\Omega)}{\text{d}z}\right|_\text{e} = \frac{-\bar{\sigma}_\text{e}NI(z,\Omega)}{\cos(\theta)} \tag{2.29}$$

with Ω the vector pointing in source direction, $-\bar{\sigma}_\text{e}$ as the mean extinction cross section and N the total number of particles.

The second beam (b) describes the multiple scattering process by

$$\frac{\mathrm{d}I(z,\Omega)}{\mathrm{d}z}\bigg|_{\mathrm{s}} = \frac{-\bar{\sigma}_{\mathrm{s}}N}{\cos(\theta)}\int_{4\pi}I(z,\Omega')\frac{P(\Omega,\Omega')}{4\pi}\mathrm{d}\Omega' \tag{2.30}$$

for scattering with the probability function P leading from direction Ω' to Ω and $\bar{\sigma}_{\mathrm{s}}$ as the mean scattering cross section. Thus, the intensity is represented by the integration over the solid angle for all possible multiple scattering radiant energies from Ω' to Ω.

The last processes which has to be considered is the diffusive intensity change, marked by the beam c.

$$\frac{\mathrm{d}I(z,\Omega)}{\mathrm{d}z}\bigg|_{\mathrm{d}} = \frac{-\bar{\sigma}_{\mathrm{s}}N}{\cos(\theta)}\pi F_0\frac{P(\Omega,-\Omega_0)}{4\pi}\exp\left(-\frac{1}{\cos(\theta_0)}\int_0^\infty\bar{\sigma}_{\mathrm{e}}N(z')\mathrm{d}z'\right) \tag{2.31}$$

$$\Rightarrow\frac{\mathrm{d}I(z,\Omega)}{\mathrm{d}z}\bigg|_{\mathrm{d}} = \frac{-\bar{\sigma}_{\mathrm{s}}N}{\cos(\theta)}\pi F_0\frac{P(\Omega,-\Omega_0)}{4\pi}\exp\left(-\frac{1}{\cos(\theta_0)}\tau\right) \tag{2.32}$$

where the definition of the optical thickness τ from equation 2.16 has been used.

It seems reasonable to switch the coordinate system from Cartesian coordinates to spherical coordinates for a shorter description of Equation 2.32. In addition to that, the abbreviation $\mu = \frac{1}{\cos(\theta)}$ is used in the following.

The source function J can be written as follows:

$$J = \frac{\mathrm{d}I(z,\Omega)}{\mathrm{d}z}\bigg|_{\mathrm{e}} + \frac{\mathrm{d}I(z,\Omega)}{\mathrm{d}z}\bigg|_{\mathrm{s}} + \frac{\mathrm{d}I(z,\Omega)}{\mathrm{d}z}\bigg|_{\mathrm{d}} \tag{2.33}$$

$$\Rightarrow J = -\frac{I(z,\Omega)}{\mu} + \frac{\tilde{\omega}}{\mu}\int_{4\pi}I(z,\Omega')\frac{P(\Omega,\Omega')}{4\pi}\mathrm{d}\Omega'$$

$$+ \frac{\tilde{\omega}}{\mu_0}\exp\left(-\frac{\tau}{\mu_0}\right)\frac{P(\Omega,-\Omega_0)}{4\pi}\pi F_0 \tag{2.34}$$

In this example, the following differential equation has to be solved:

$$\mu\frac{\mathrm{d}I(\tau,\mu,\phi)}{\mathrm{d}\tau} = I(\tau,\mu,\phi) - \frac{\tilde{\omega}}{4\pi}\int_{-1}^{1}\mathrm{d}\mu'\int_0^{2\pi}\mathrm{d}\phi'P(\mu,\phi,\mu',\phi')I(\tau,\mu',\phi') +$$

$$\frac{\tilde{\omega}}{4\pi}\pi F_0 I(\tau,\mu,-\mu_0,\phi_0)\exp\left(-\frac{\tau}{\mu_0}\right) \tag{2.35}$$

Equation 2.35 is known as the basic equation of radiative transfer in the example of the scattering phase function. This equation can be analytically solved by for example the two-stream procedure (e.g. Meador and Weaver, 1980). This is an approximation which leads to large errors in the simulation of radiation transport in models. Therefore, it is reasonable to

use a numerical solving procedure like the discrete ordinates method (e.g. Chandrasekhar, 1960; Stamnes et al., 1988). The discrete ordinates method describes the discretisation of the spatial components of the radiative transfer equation using Gauss-Legendre quadrature points (e.g. Abramowitz et al., 1972).

2.2.6 Scattering properties of clouds in the atmosphere

The optical properties of a cloud, the cloud optical depth $\tau^\star$, the single scattering albedo $\tilde{\omega}$ and scattering phase function $P(\mu, \phi, \mu', \phi')$ define the absorption, scattering and reflection of radiation. The cloud optical thickness is approximately independent of the incoming wavelength. The same holds for particles with a size parameter $\hat{x}$ around 10, where $\hat{x}$ is defined as

$$\hat{x} = \frac{2\pi r}{\lambda} \tag{2.36}$$

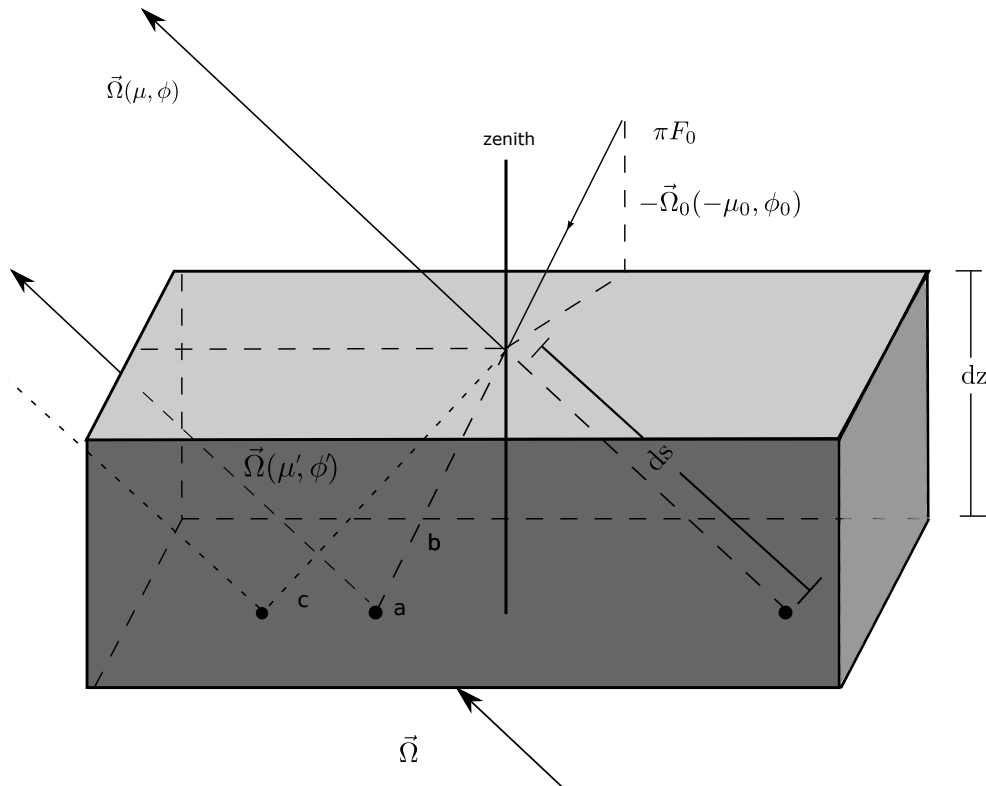Only the single scattering albedo shows a wavelength dependence.

Figure 2.6: The figure shows a box, like it can be assumed in an atmospheric model. The transfer of the solar flux is separated into three parts: a) extinction, b) multiple scattering and c) single scattering. This figure is adopted from Liou (2002).

For cloud droplets with a small radius compared to the incoming wavelength, scattering can be described through Rayleigh scattering. Here the single scattering albedo shows the following wavelength dependency:

$$\tilde{\omega} = \frac{Q_s}{Q_e} = \frac{\sigma_s}{Q_e} \; \propto \frac{r^6}{\lambda^4} \tag{2.37}$$

For particle sizes outside the Rayleigh regime, the Mir theory for scattering is applied. Here, the Maxwell Equations are solved for a three dimensional space in polar coordinates. Boundary conditions for solving the resulting set of partial differential equations are defined by the properties of the cloud particles. For example, if the cloud is consistent of mainly ice particles, the boundary conditions are defined by the geometrical properties of the sphere, representing the ice crystal. The solution of this set of differential equations is non trivial but an important factor for a reasonable simulation of the radiative properties of a cloudy atmosphere.

2.2.7 Calculation of photolysis rates

All components of the Earth's atmosphere are permanently exposed to the radiation emitted by the Sun. The physical characterisation of radiation is done by the quantisation of the emitted photon energy:

$$E = h\nu = {hc}/{\lambda} \tag{2.38}$$

with $h =$ as the Planck constant, c the speed of light, and λ the wavelength. Atoms and molecules are able to absorb radiation for specific amounts of energy depending on their rotational, vibrational and electronic states. Transitions between rotational, vibrational and electronic states are discrete, following quantum mechanic laws and its selection rules. Energy absorption by molecules can generate heat through collisions of the absorbing molecule with its surrounding medium. In addition to that, the absorbed energy changes the electronic state of the molecule through electronic excitation. An excited molecule does not remain in this state, it returns back to its ground state by emitting a photon corresponding to the energy gap between the ground and excited state. If the incoming energy is high enough, it is possible that the molecule is moved to the excited state by photon absorption and then dissociates, if the absorbed energy is higher than the bonding energy. This process is called photodissociation or further on called photolysis. Due to the relative high energy for ionisation or dissociation, only photons of the Sun's spectrum in the wavelength region between $10\,\text{nm}$ to $800\,\text{nm}$ can initiate photolysis processes. The photolysis rate is defined by:

$$\frac{d[X]}{dt} = -j_x[X] \tag{2.39}$$

with $[X]$ the molecule concentration, given in cm^{-3} and j_X the photolysis rate in s^{-1}. The photolysis rate is calculated by:

$$j_{\mathrm{X}}(\tau) = \int_{\lambda_{\min}}^{\lambda_{\max}} \underbrace{\sigma_{\mathrm{X}}(\lambda)}_{\text{cross section}} \underbrace{\Phi_{\mathrm{X}}(\lambda)}_{\text{quantum yield}} \underbrace{I_{\mathrm{A}}(\tau, \mu, \phi, \lambda)}_{\text{actinic flux}} \mathrm{d}\lambda \qquad (2.40)$$

The actinic flux I_A is defined as the amount of energy given in $\mathrm{W\,m^{-2}}$ penetrating a unit volume of space at point r.

$$I_{\mathrm{A}}(\tau, \mu, \phi, \lambda) = \int_{0}^{2\pi} \int_{-1}^{1} I(\tau, \mu, \phi, \lambda) \mathrm{d}\phi \mathrm{d}\mu \qquad (2.41)$$

with I: radiance, $\mu = \cos\theta$, θ: zenith angle, ϕ: azimuth angle. The spectral radiance is gained by solving the differential equation given in equation 2.35. The dependence on the given wavelength λ is an additional factor which has to be taken into account for the photolysis rate calculation. The wavelength dependence of the spectral radiance is mainly caused by the wavelength dependence of the single scattering albedo $\tilde{\omega}$ and scattering phase function P.

Working with a three dimensional atmospheric chemical transport model, the radiance I has to be calculated for each point within the model by solving the non-trivial radiation transfer equation. In most models, the assumption is made that the atmosphere has an plane-parallel geometry relative to the ground of the Earth. For further details see Liou (2002), Chandrasekhar (1960), Bian and Prather (2002). It is important that the actinic flux is strongly altitude dependent as depicted in Figure 2.7.
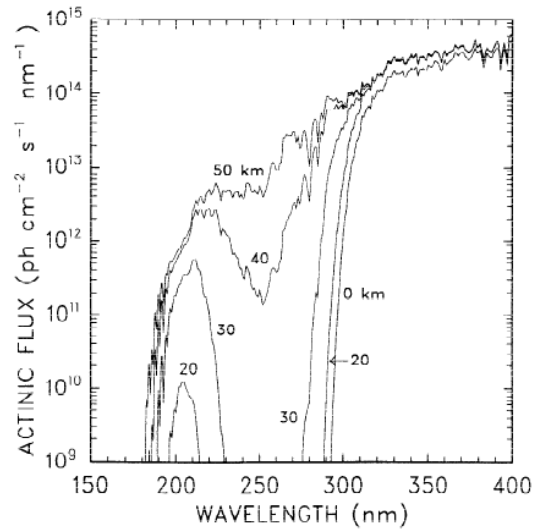

Figure 2.7: Actinic flux with altitude and wavelength dependence (DeMore et al., 1997)

2.3 Photochemical reactions with relevance for the chemical composition in the UTLS

The Earth's atmosphere is cleaned by oxidising chemical processes. Cleaning means that chemical compounds are removed or destroyed by oxidation. Oxidation in the UTLS region is mostly induced by the hydroxyl radical OH, ozone O_3 and nitrate NO_3. Oxidation via chlorine and bromine radicals are less important. In addition, the ground state of atomic oxygen O^3P also accounts only for a small part. The photolysis reactions

$$O_3 + h\nu \quad \rightarrow \quad O_2 + O^3P \tag{2.42}$$

$$O_3 + h\nu \quad \rightarrow \quad O_2 + O^1D \tag{2.43}$$

play an important role in the UTLS region. The photolysis rate of reaction 2.43 only occurs for wavelengths $\lambda < 320\,\text{nm}$, whereas reaction 2.42 is possible for $\lambda > 320\,\text{nm}$. The excited oxygen state O^1D is quenched by the collision with either N_2 or O_2 - represented by M:

$$O^1D + M \quad \rightarrow \quad O^3P + M \tag{2.44}$$

The ground state oxygen atom reacts with molecular oxygen by

$$O^3P + O_2 + M \quad \rightarrow \quad O_3 + M \tag{2.45}$$

forming O_3 again. Additionally, the excited O^1D atom has the ability to break the bond of water vapour leading to:

$$O^1D + H_2O \quad \rightarrow \quad 2OH \tag{2.46}$$
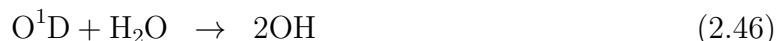
The analysis of these reactions leads to a steady state of ozone in the UTLS during daylight time. Taking another photolysis rate in the wavelength region $\lambda < 240\,\text{nm}$ into account, the so called steady state Chapman cycle is formed:

$$O_2 + h\nu \quad \rightarrow \quad O^3P + O^3P \tag{2.47}$$

The steady state Chapman cycle is formed by the reactions 2.47, 2.45, 2.44 and 2.43. This cycle is sufficient for the explanation of the observed ozone maximum concentration location inbetween $20 - 30$km. Moreover, in contrast to observations, this steady state overestimates the maximum ozone concentration by a factor of two (Jacob, 1999).

At this point, atmospheric water vapour gains importance as a significant sink of strato-spheric O_3. Starting with reaction 2.46, the catalytic loss cycle of HO_x (OH, HO_2) is induced:

$$OH + O_3 \rightarrow HO_2 + O_2 \tag{2.48}$$
$$HO_2 + O_3 \rightarrow OH + 2O_2 \tag{2.49}$$
$$\tag{2.50}$$

Together with 2.46 and

$$OH + HO_2 \rightarrow H_2O + O_2 \tag{2.51}$$

the chain reaction loss of ozone is formed (Jacob, 1999).

The second catalytic loss cycle for stratospheric ozone is triggered by the photolysis

$$NO_2 + h\nu \rightarrow NO + O^3P \tag{2.52}$$

for $\lambda > 390\,\text{nm}$ and

$$NO + HO_2 \rightarrow NO_2 + OH \tag{2.53}$$

The main part of the NO_x (NO, NO_2) cycle is formed by:

$$NO_2 + O^3P \rightarrow NO + O_2 \tag{2.54}$$
$$NO_2 + OH + M \rightarrow HNO_3 + M \tag{2.55}$$
$$NO_2 + O_3 \rightarrow NO_3 + O_2 \tag{2.56}$$
$$NO_3 + NO_2 + M \rightarrow N_2O_5 + M \tag{2.57}$$

Reservoirs of NO_x are formed by the photolysis rates

$$NO_3 + h\nu \rightarrow NO_2 + O^3P \tag{2.58}$$
$$HNO_3 + h\nu \rightarrow NO_2 + OH \tag{2.59}$$
$$N_2O_5 + h\nu \rightarrow NO_3 + NO_2 \tag{2.60}$$
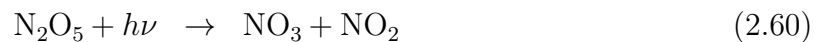
where reaction 2.58 in only one of two possible photolysis channels.

Together with

$$HNO_3 + OH \rightarrow NO_3 + H_2O \tag{2.61}$$

the reactions 2.55, 2.56 and 2.57 represent the oxidation process of NO_x. The oxidation products HNO_3 and N_2O_5 can be converted back to NO_x by reaction 2.59, 2.60, 2.58. It can be concluded that the catalytic loss cycle by NO_x is strongly connected to the NO_y cycle. Thus, the important value for the O_3 loss is the ratio of NO_x and NO_y (Jacob, 1999). The source of NO_y is the oxidation of N_2O:

$$N_2O + O^1D \quad \rightarrow \quad 2NO \tag{2.62}$$

This brief overview, mainly summarised from Jacob (1999) and Wahner and Moortgat (2007), shows the importance of photolysis rates in the UTLS region and below. These photolysis rates have high influence on the ozone concentration from the troposphere up to the stratosphere.

Since the radiation budget of the atmosphere is dependent on the ozone concentration, it is necessary to have a realistic simulation of photolysis rates to get a reasonable simulation of chemistry processes in the Earth's atmosphere. However, the sensible simulation of stratospheric ozone is a challenging task on its own. Additionally, the radiation budget itself is not only dependent on the chemical composition but also on the radiative impact of clouds.

2.4 Description of the polar vortex

The concept of the Earth's energy balance has been introduced in section 2.1. The model showed that long wave radiation emitted by the Earth's surface can be represented by a black body of a constant temperature. The global mean surface temperature stays constant throughout the year (Schumann, 2012). However, due to the Earth's rotation and propagation around the sun, temperature differences occur. The temperature difference and the Coriolis force induce momentum in the atmosphere, forming a complex system of propagating waves of different kind (Holton and Hakim, 2013). Besides the horizontal motion, vertical motion is also present. In the tropical troposphere, air parcels are lifted upwards due to deep convection. This motion is the first of three parts of the so called Brewer-Dobson Circulation (BDC). If the rising tropical air has no interaction through mixing with mid latitude stratospheric air, this motion is referenced as the tropical pipe (e.g. Seinfeld and Pandis, 2006). The shallow and deep branch of the Brewer-Dobson Circulation transport the tropical air masses polewards, as depicted in Figure 2.8. The poleward flow of mass can be explained by the concept of Rossby wave propagation (Roedel, 2013). Since the continuity equation of mass holds, the upward transported air descends again at high latitudes.
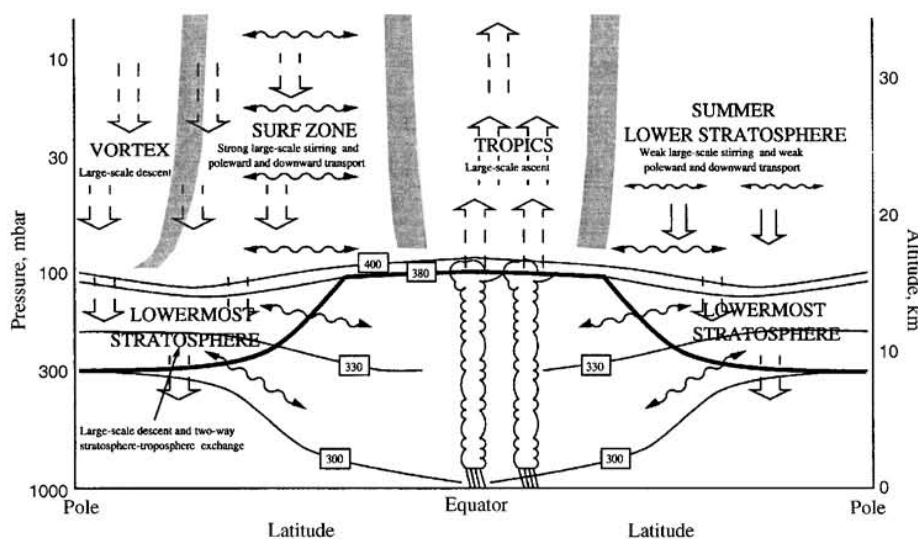
Figure 2.8: Schematic altitude-latitude cross section of atmospheric transport and mixing. Horizontal lines represent temperature isotherm, labelled with the respective potential temperature. This Figure is taken from Seinfeld and Pandis (2006) .

During the southern hemisphere (SH) winter, temperatures are decreasing. Due to the high solar zenith angle, no radiation reaches the Earth's surface at high southern latitudes. A development of a stable westerly circulation can be observed at the beginning of every winter. This stable circulation is called *polar vortex* (Seinfeld and Pandis, 2006). The polar vortex remains its stability from winter to early spring. When the sun starts to rise again, temperature increases and the vortex breaks. For chemistry climate models it is of high importance to capture the dynamical properties of the polar vortex correctly. This ability is highly constraint by the understanding of the dynamics itself and climate forcing that controls stratospheric temperatures (Newman and Nash, 2005).

Since the air within the vortex is highly encapsulated, high levels of ozone concentration remain during southern hemisphere polar winter. The high values are reached by transported ozone through the BDC. Springtime ozone levels are observed to decrease significantly. This is known as the *ozone hole*. This decrease can not only be explained by atmospheric dynamics. An absence of photodissociation due to the high SZA is also present. Thus, no atomic oxygen (O) is produced through photolysis of O_2. The catalytic depletion of ozone by atomic oxygen is also not present. By the work of Molina and Molina (1987), the activation of chlorine and bromine reservoirs (e.g. ClO and BrO) has been introduced as an additional catalytic cycle of ozone distribution. Nevertheless, taking only the gas phase reactions into account, levels of calculated ozone concentrations would still be higher than observations.

Since the polar stratosphere shows very low temperatures ($< 195\,\mathrm{K}$), so called polar stratospheric clouds (PSCs) are formed. Heterogeneous reactions on the surface of PSC

particles are the most important chlorine-activating reactions. When the sun is rising again, the produced chlorine and bromine molecules undergo photolysis, forming Cl and Br. These atoms react with ozone and result in ozone depletion of a realistic amount.

Thus, the combination of low temperatures, heterogeneous reactions on the surface of PSCs and photolysis, are able to explain the southern hemisphere ozone hole. The description of the ozone hole and underlying mechanism is mainly based on Seinfeld and Pandis (2006). Figure 2.9 depicts the temporal evolution of the processes described above.
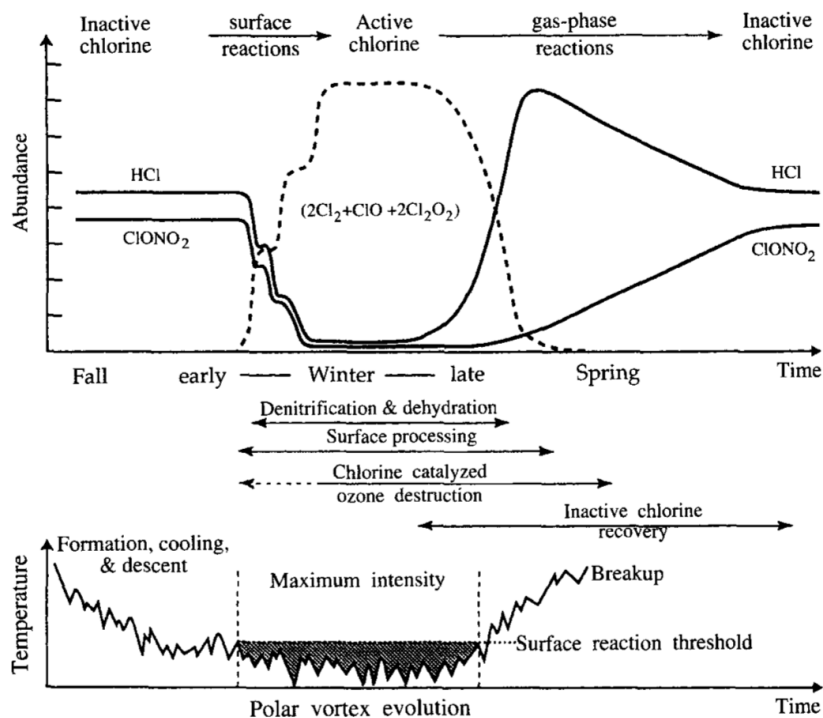

Figure 2.9: The upper panel focuses on the schematic description of the chlorine reservoir activation as a function of time. The corresponding polar vortex temperature is depicted in the lower panel as a function of time. Taken from Seinfeld and Pandis (2006).

Finally, as shown in Section 2.1.2, it should be kept in mind that stratospheric ozone shows a strong heating capability. The ozone depletion results in a temperature decreases. The stronger the ozone hole gets, the stronger the temperature decrease. Consequently, these changes result in changes of global dynamics.

3 The modelling system ICON-ART

The development of the ICON (ICOsahedral Non-hydrostatic modelling framework) has started as a joint development project of the Deutscher Wetterdienst (DWD) and the Max Planck Institute of Meteorology. This project was initialised for developing a next generation modelling system. ICON can be used for short term numerical weather prediction as well as for global climate simulations. In the following section, the basic description in terms of equations sets is briefly given. A special focus on the tracer transport is set in section 3.1.4 and in section 3.2 in the description of the ART extension (Aerosols and Reactive Trace gases Rieger et al. (2015).

3.1 Technical description of ICON

3.1.1 Horizontal grid structure

The equation of motion, or also called momentum equation, is the main equation to be solved in atmospheric models. For the horizontal discretisation for which the model equation is solved can be a Cartesian coordinate or spherical coordinate system. In both systems, singularities can occur, e.g. at the Earth's poles. Both, spherical and Cartesian grids, represent regular grids. In regular grids the cells are aligned in a fixed pattern. The second type is an irregular grid type which allows to overcome the singularity problem as well as problems with boundary conditions, e.g. coastlines. In this grid type, the cells are not aligned in a fixed lattice. In ICON, an icosahedral-triangular C grid is used (e.g. Staniforth and Thuburn, 2012). This grid type allows a very natural way of implementing local grid refinement. This can easily be seen by the general definition of this grid structure. The icosahedral grid is an unstructured triangular grid. A spherical icosahedron (see Figure 3.1) is refined in successive way, to construct the horizontal grid structure of ICON. For the root division (Rn), following Sadourny et al. (1968), the triangle edges are divided in n equal parts. The connection of the division points constructs new triangles. In those triangles a section division, the k bisection division (Bk), is performed. The total number of cells can be calculated by

$$n_{\text{cell}} = 20n^2 4^k \tag{3.1}$$

The resulting grid is called RnBk grid and the effective grid resolution $\overline{\Delta x}$ is defined as:

$$\overline{\Delta x} = \sqrt{\overline{a_c}} = \sqrt{\frac{\pi}{5} \frac{r_e}{n 2^k}} \tag{3.2}$$

with $\overline{a_c}$ the average cell area and r_e the Earth's radius. An overview for the effective horizontal grid resolution, used in this thesis is given in Table 3.1.

Grid	n_{cell}	$\overline{\Delta x}$ [km]
R2B4	20480	157.8
R2B5	81920	78.9
R2B6	327690	39.5
R2B7	1310720	19.7

Table 3.1: Total number of cells and effective grid resolution of the grids used in this work.

This horizontal grid type addresses the need of mass-conservation in multi-resolution modelling and efficiency in the performance on massively parallel computing architectures (Wan et al., 2013).

3.1.2 Vertical grid

Like most atmospheric modelling systems, the vertical coordinate system in ICON is chosen to be a terrain following system. More precisely, the SLEVE system (smooth level vertical) is used, based on Schär et al. (2002) and Leuenberger et al. (2010). To provide intersection of model levels at steep orography regions, a lower boundary for the model level distance is defined to be 400 m.
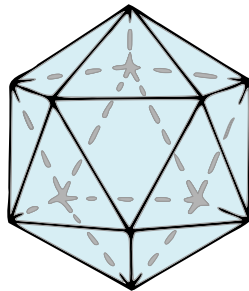

Figure 3.1: Geometric representation of an icosahedron, the basis of the ICON horizontal grid structure.

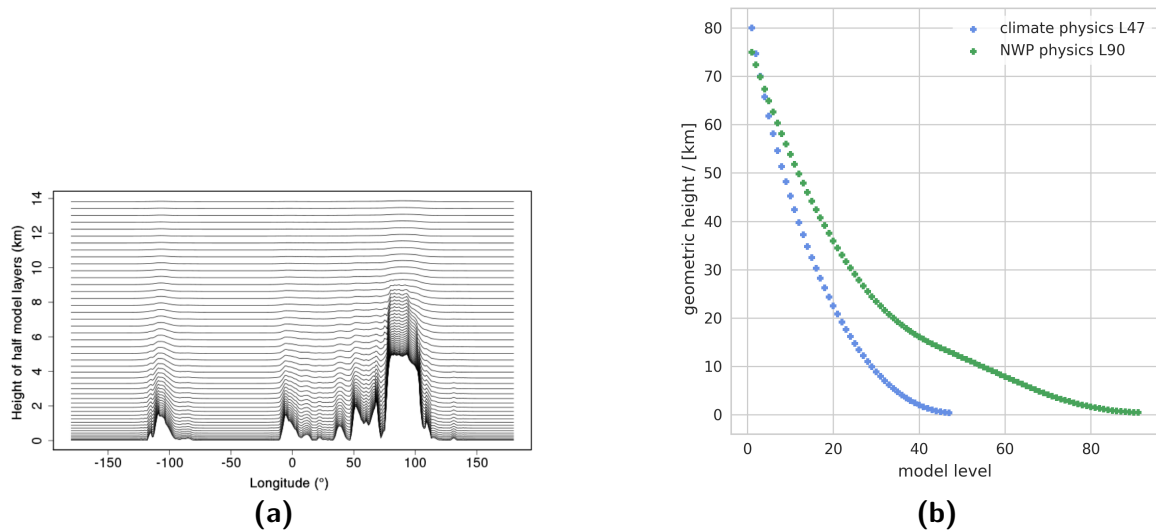**(a)**   **(b)**

Figure 3.2: a) Height of the lowest 46 ICON model levels at 33°N in the configuration with 90 total model levels. Taken from Weimer et al. (2017); b) Vertical levels of both physics configurations, NWP and climate physics configuration. For the NWP physics configuration 90 levels are used, for the climate configuration 47 levels.

3.1.3 Dynamical core

The main development goals of ICON are (following Zängl et al. (2015)):

- Improvement of conservation properties, compared to GME (Globales Modell) and COSMO (Consortium for small scale modelling) . This includes energy, local mass and potential vorticity conservation. Additionally, mass consistent tracer transport should be achieved.

- Improvement of scaling behaviour on massive parallel computing systems.

- Static grid refinement which includes one- and two-way nesting. Nesting can result in more precise simulation of atmospheric processes and computational time reduction on the other hand.

The definition of the dynamical core, the set of equations for solving the fluid and thermodynamic equations of motion if ICON is based on Gassmann and Herzog (2008). In general, the dynamical core does not include sub-grid scale parameterisations or other physical processes like radiative transfer. The dynamical core consists of a set of equations of the non-hydrostatic formulation and Reynolds-averaged Navier-Stokes equation. Thus the set of equations is a system of non-linear partial differential equations, which are read like following:

$$\frac{\partial v_{\mathrm{n}}}{\partial t} + \frac{\partial K_{\mathrm{h}}}{\partial n} + (\zeta + f)v_{\mathrm{t}} + w\frac{\partial v_{\mathrm{n}}}{\partial z} = -c_{\mathrm{pd}}\theta_v\frac{\partial \pi}{\partial n} + F(v_{\mathrm{n}}) \tag{3.3}$$

$$\frac{\partial w}{\partial t} + \mathbf{v}_{\mathrm{h}} \cdot \nabla w + w\frac{\partial w}{\partial z} = -c_{\mathrm{pd}}\theta_v\frac{\partial \pi}{\partial z} - g \tag{3.4}$$

$$\frac{\partial \rho}{\partial t} + \nabla \cdot (\mathbf{v}\rho) = 0 \tag{3.5}$$

$$\frac{\partial \rho\theta_v}{\partial t} + \nabla \cdot (\mathbf{v}\rho\theta_v) = \tilde{Q} \tag{3.6}$$

$$\frac{\partial \pi}{\partial t} + \frac{R_{\mathrm{d}}}{c_{\mathrm{vd}}}\frac{\pi}{\rho\theta_v}\nabla \cdot (\mathbf{v}\rho\theta_v) = \hat{Q} \tag{3.7}$$

with

$$\pi = \left(\frac{R_{\mathrm{d}}}{p_{00}}\rho\theta_v\right)^{\frac{R_{\mathrm{d}}}{c_{\mathrm{vd}}}} \tag{3.8}$$

the Exner function.

The prognostic variables are the horizontal wind component v_{n}, the vertical wind component w, virtual potential temperature θ_v and density ρ. The index n of v_{n} denotes the component of v normal to the triangle edges of the triangular horizontal grid. The horizontal wind component is denoted as $\mathbf{v}_{\mathrm{h}}$ and the three dimensional wind as $\mathbf{v}$. The symbol p_{00} represents the reference pressure of 1000 hPa, conventionally used for the potential temperature definition. The symbol ζ is the vertical vorticity component, f the Coriolis parameter, K_{h} the kinetic energy. The heat capacity for constant pressure and constant volume are denoted as c_{pd} and c_{vd}, leading to the gas constant of dry air, defined as $R_{\mathrm{d}} = (c_{\mathrm{pd}} - c_{\mathrm{vd}})$. The diabatic heat-source terms are represented by $\tilde{Q}$ and $\hat{Q}$. The source term for the horizontal momentum is represented by $F(v_{\mathrm{n}})$ The main coordinates, defined by the partial differentials are the time t and height z. The partial differential $\frac{\partial}{\partial n}$ denotes the horizontal derivative in triangle-edge normal direction.

The differential equation 3.5 represents the equation for momentum conservation. The contribution of the viscosity momentum term is neglected, compared to the turbulent momentum flux. Additionally, molecular heat flux is neglected, compared to turbulent heat flux. A more detailed description of the dynamical core of ICON can be found in Zängl et al. (2015).

3.1.4 Tracer transport system

The species continuity equation is a non-linear partial differential equation which needs to be solved to simulate the transport of chemical species in an atmospheric model. In

addition, the momentum is gained from the directional momentum equation. The local acceleration is defined as

$$\vec{a} = \frac{\mathrm{d}\hat{v}}{\mathrm{d}t} = \frac{\partial \hat{v}}{\partial t} + \hat{v} \cdot \nabla \hat{v} \tag{3.9}$$

where $\hat{v}$ is the barycentric mean of the three dimensional velocity. The continuity equation is defined as

$$\frac{\mathrm{d}\bar{\rho}}{\mathrm{d}t} = -\bar{\rho}\nabla\hat{v} \tag{3.10}$$

with $\bar{\rho}$ as the averaged air density. The Reynolds averaging is applied since ICON represents a model which is able to treat turbulence and accounts for subgrid-scale disturbances, like turbulence. With the barycentric mean, a mass specific variable ψ represents a tracer in the model as follows:

$$\hat{\psi} = \frac{\bar{\rho}\psi}{\bar{\rho}} \tag{3.11}$$

and

$$\hat{\psi} = \hat{\psi} + \psi'' \tag{3.12}$$

with $\hat{\psi}$ defined like above, representing the slow varying mean value of ψ and ψ'' the representation of the fluctuating component.

For gaseous chemical species, the tracer $\hat{\psi}_{\mathrm{g},i}$ can be expressed by

$$\hat{\psi}_{\mathrm{g}} = \frac{\overline{\rho\frac{\rho_i}{\rho}}}{\bar{\rho}} = \frac{\bar{\rho}_i}{\rho} \tag{3.13}$$

with ρ_i the partial density of the gaseous tracer i.

The equation of motion can be written as follows:

$$\rho\frac{\hat{\mathrm{d}}\hat{\psi}_{\mathrm{g},i}}{\mathrm{d}t} = -\nabla\left(\hat{v}\bar{\rho}\hat{\psi}_{\mathrm{g},i}\right) - \nabla\overline{\rho v\psi''_{\mathrm{g},i}} + P_i + L_i + E_i \tag{3.14}$$

where the additional terms, compared to the basic continuity equation 3.10, denote the production P_i, loss L_i and emission E_i induced changes in the mass specific amount of a chemical tracer. The term $\nabla\overline{\rho v\psi''_{\mathrm{g},i}}$ describes the changes due to turbulent fluxes. Turbulence in general is treated by an one dimensional TKE (Turbulent Kinetic Energy) turbulence scheme (Raschendorfer, 2001).

3.1.5 Nesting technique

With ICON-ART it is possible to use the so called *nesting technique*. The model is setup with a global grid, e.g. R2B6. It is possible to define a finer and smaller grid, which is a subdomain of the global grid. In this case, the grid size would be R2B7. The bisection, marked by the capital B, can only be increased by one. The nested domain is also called *child domain*. The global domain is referred as the *parent domain*. The interaction between child and parent domain can be either be one-way or two-way. For the one-way feedback, variables from the parent domain are used as boundary conditions for the child domain. The simulated variables in the child domain have no influence on the variables of the parent domain. For the two-way interaction, the solution of the primitive equations in the parent domain is relaxed towards the result of the child domain. This relaxation technique is applied to the prognostic variables of $v_{\mathrm{n}}, w, \Theta_{\mathrm{v}}$ and ρ. In addition, the relaxation technique is applied to the prognostic tracers $q_{\mathrm{v}}, q_{\mathrm{i}}$ and q_{c}.

The relaxation itself is the last step of three major steps in the two-way nesting process. The other two steps are the upscaling process and the increment solution. Since the child domain has a smaller grid spacing, the named variables have to be interpolated to the grid of the parent domain. The interpolation is done in a predefined communication zone, usually 2 grid boxes of the parent grid. If Φ_{p}^{n} is one of the named variables in the parent domain, the solution of this variable, at the next time step, Φ_{p}^{n+1} has to be calculated. The solution also depends on the upscaled solution $\Phi_{\mathrm{c}\to\mathrm{p}}^{n+1}$.

3.2 The ART extension

The main goal of the development of the ART module is to provide a flexible model with a full representation of the interaction between the atmospheric composition, radiation and dynamics. New processes should be easy to be added to the existing ones. The first stage of flexibility is realised by the usage of a compile directive. As shown in Rieger et al. (2015), this directive allows the compilation of the model ICON without the ART module. The second stage of flexibility has been developed in the scope of this thesis. The next section describes the second stage, the development of a flexible tracer structure for ICON-ART in more detail. The description is mainly based on Schröter et al. (2018).

3.2.1 The flexible ART tracer framework

At one point in time, all numerical models need to find an answer to the question how to transfer text based information (e.g. tracer metadata) into the model's program code. The text based format XML - eXtensible Markup Language (see W3C), gives the developer and the user the ability to store and transport information in a structured way.

XML has only few mandatory rules, e.g. there has to be exactly one root-element. The framework in which the information is structured can be freely chosen. The structure itself allows for a human readable format. ICON-ART uses the Fortran interface TIXI (`https://software.dlr.de/p/tixi/home/`) to read the XML file. The TIXI interface includes a flexible mechanism for XML file read in. Since the scripting language of XPath is used, the navigation through an XML document is an easy task to perform. The XML reading routine can be structured in the same way like someone would read a document and would remember the content in a most natural way. An example structure of such an XML input file for the tracer structure is the following:

```xml
<?xml version="1.0" encoding="UTF-8"?>
<!DOCTYPE tracers SYSTEM "tracers_gp.dtd">


<tracers>

  <chemical id="TRO3">

   <mol_weight type="real"> 4.800E-2 </mol_weight>

   <lifetime type="real"> 2592000 </lifetime>

   <transport type="char"> stdchem </transport>

   <init_mode type="int"> 0 </init_mode>

   <unit type="char"> mol mol-1 </unit>

   <long_name type="char"> ozone </long_name>

  </chemical>

</tracers>
```

The XML file is scanned automatically. For the realisation of this feature, it is necessary to predefine the type of input. Every tag has a mandatory type definition, being `char, int` and `real`. The first word in brackets, `<tracers>` is called XML-tag. The tag `<chemical id="TRO3">` has the additional attribute `id` for the tag `chemical`. To identify a specific tracer, the system uses the given attribute (e.g. `id`). Tags are used to build up the metadata structure. It is a key-value storage where the tag (e.g. `mol_weight`) is the key with the value, e.g. `4.800E-2` for ozone. The number `4.800E-2` is then stored in the metadata structure of ICON-ART. At this point it should be noted that there are two kinds of metadata: necessary and optional metadata. Necessary metadata depend on the polymorphic type. Passive tracers do have different necessary metadata than chemical tracers. The optional metadata are read in automatically. Every tag in the XML file is translated into an entry in the key-value storage.

The structure of the ART tracer framework is shared with the core ICON tracer framework and only expanded in cases needed. In addition to that, tracers can share attributes, and

are distinguished by additional attributes. For example, ozone appears in two different subroutines for chemistry. The first, using a lifetime based mechanism, and the second, using a full gasphase approach.

The tag `<mol_weight>` can be used for unit conversion within a subroutine and is given in kgmol^{-1}. The tag `<lifetime>` is used for simplified integration methods for a given life time of a species, in seconds. Some chemical substances or passive tracers do not have to be transported thus the tag `<transport>` ensures that this information is transferred to the program code and the transport is switched on or off, respectively. In addition to that, templates can be defined. In this case, a template named `stdchem` is chosen. At model start up, this template is translated into a specific selection of horizontal and vertical transport schemes. Each scheme stands for a specific numerical discretisation of the mass continuity equation in horizontal or vertical directions. Currently, there are three different transport templates available: `off`, `stdaero` and `stdchem`. These templates avoid the necessity to add a tracer advection scheme and flux limiter for each single tracer in the namelist. Hence, the values of the ICON-ART namelist parameters `ihadv_tracer`, `ivadv_tracer`, `itype_hlimit` and `itype_vlimit` are overwritten by the template. Specific information concerning the advection schemes mentioned can be found in the official ICON documentation. Specifying `off` will deactivate advective transport for this tracer completely.

The transport template `stdchem` uses the same advection schemes as `stdaero`. However, the considerably faster positive definite flux limiters are used. The conservation of linear correlations is traded for a faster computation of the advection.

If chemical species need to be initialised, this is achieved via `<init_mode>` and a respective number corresponding to the initialisation scheme. If the `init_mode` is set to 0, no external initialisation data is used. With integers different from zero, data from other models, like EMAC (Jöckel et al., 2005) or MOZART (Emmons et al., 2010), interpolated on the horizontal icosahedral grid are read in and used. The vertical interpolation is performed online. Thus, the initialisation dataset stays unchanged, regardless of the choice of model levels for the simulation.

The structure of the key-value storage for every tracer is built up automatically. This feature allows for an extensive flexibility which has to be controlled. In our case, attributes are used in a fixed manner, they define our basic framework of the tracer structure. The full flexibility, direct access, control mechanisms and data type distinction, are only a few advantages of this XML based procedure against other currently used strategies.

3.2.2 Connection of ART to the ICON climate physics

By the concept of flexibility be conserved during the development process, it was not only possible to connect the NWP physics package, as described by Rieger et al. (2015). The

connection to the ECHAM physics configuration in ICON-ART is the second main technical achievement of this thesis. Figure 3.3 shows the calling structure for the example of the coupling of ART and the ECHAM physics configuration.
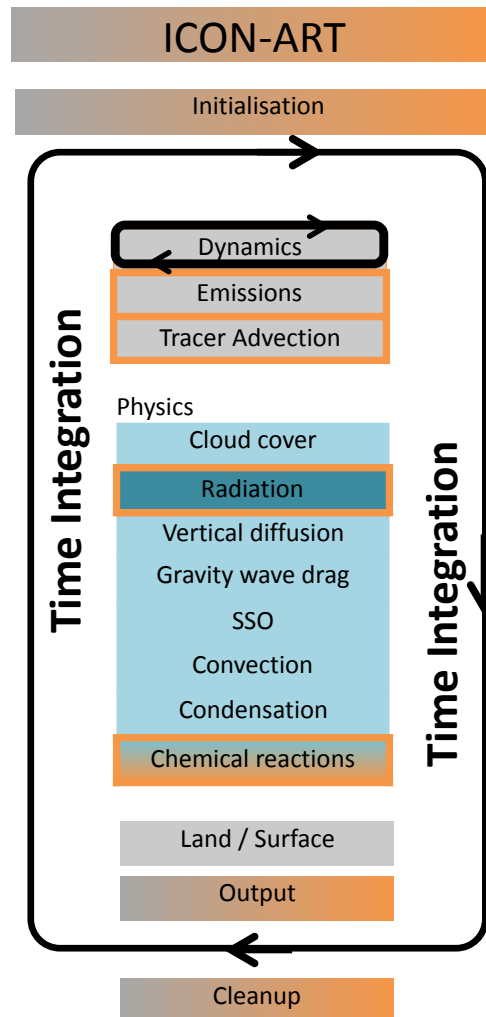

Figure 3.3: Schematic description of process calling structure in the climate configuration of ICON-ART.

Boxes marked partly orange are shared structures between ICON and ICON-ART. Boxes with an orange frame are processes affected by ART tracer tendencies. Boxes with an orange background are ART routines. The physics part is represented using different blue boxes. The radiation subprocess is depicted with a dark blue shaded box because the radiation process is called with a reduced frequency than other processes. Chemical reactions are part of the physics routine in climate configuration, but only effective if the compiler directive `D__ICON_ART` is used. All processes marked with a blue shade can have an individual calling frequency.

3.2.3 Radiation modules in ICON-ART

For the ICON-ART physics, there are two different realisations of radiation calculation. Both share the main basic properties. Therefore, the following description is focused on the radiation model used for climate integrations, namely PSRad-RRTMG (Pincus and Stevens, 2013). The part of RRTMG is based on the generalised parameterisations of the Rapid-Radiative-Transfer-Model for General Circulation Model (GCM) (Mlawer et al., 1997; Iacono et al., 2008). This package is originally designed for the ECMWF an is based on the correlated k approach. With this approach the connection of high-resolution radiance, line-by-line modules to coarser resolved absorption coefficients in the RRTM model. This technique accounts for fast but accurate calculation of the actinic flux and heating rates. The optical properties of gases, aerosols and clouds are calculated separately for determined wavelength bands ranging from shortwave to longwave wavelengths. An overview for the shortwave bands used in the RRTMG-package is given in Table 3.3. The RRTM-package is based on the two-stream approximation. This approximation is the simplest approximation possible for solving the radiation transfer equation (see Equation 2.35). This approximation lacks on accuracy but is still sufficient enough for GCMs with limited computational resources.

The radiation model for the physics configuration for NWP is also based on RRTM, only the cloud, gas and aerosol optical properties differ. Both modules have in common that they are using climatological values for aerosols and gases in standard configuration. With the development of ICON-ART, the possibility of replacing the values of trace gas concentrations and aerosol concentration has been created. Additionally, feedback processes of aerosols influencing the cloud optical properties are also under current development.

Additionally, with ICON-ART, the photolysis module CloudJ is included. This module is solving the radiation transfer equation in a more accurate way, than in the RRTMG package.

Table 3.2: Overview of shortwave bands in RRTMG

200 - 263	263 - 345	345 - 442	442 - 625	625 - 778	778 - 1242
1242 - 1298	1298 - 1626	1626 - 1942	1942 - 2151	2151 - 2500	2500 - 3076
2500 - 3.846					

Table 3.3: Table of wavelength bins used for RRTMG - shortwave from band 28 to band 14.

3.2.4 CloudJ module for ICON-ART

CloudJ (Bian and Prather, 2002) (here named FastJX) is an online photolysis module which provides accurate simulation of in- and below-cloud photolysis rates in tropospheric and stratospheric chemical models. CloudJ is operating on a wavelength region which is

valid for altitudes up to approximately 100 km. Besides that, CloudJ is chosen because it provides the potential of easily updating absorption cross sections and quantum yields for the predefined set of 72 photolysis rates. The number of species can be extended as well. The RTE is solved by expansion of the scattering phase function in Legendre and Associated Legendre Functions and then applying the discrete ordinate method by using eight Gauss-Points. This approach is a eight-stream scattering solution for the RTE. For further details see Bian and Prather (2002), Wild et al. (2000) (here named FastJ-2) and Hsu et al. (2017) (here named Solar-J). It is important, that due to computational time, the integration domain (solar spectrum) is binned into 18 main wavelength bins reaching from 170 nm up to 778 nm. Mean values of each bin are represented in Table 3.4.

187	191	193	196	202	208
211	214	261	267	277	295
303	310	316	333	380	574

Table 3.4: Wavelength bins used within CloudJ.

CloudJ 7.5	Bins 1 - 17 177 nm - 412 nm	Bin 18 442 nm - 778 nm including O2 + H2O in seperate sub-bins
RRTMG	Band no 26-26 (200-552nm)	Band no 24-25 (442-778nm)

Figure 3.4: Distribution of CloudJ and RRTM bins, Figure adopted from Hsu et al. (2017)

Since version 7.5, CloudJ is extended by additional wavelength bins up to 12 μm, in 27 wavelength bins. The wavelength bins are corresponding to those used in the RRTMG package. The schematic overlap is depicted in Figure 3.4. A more detailed description can be found in Hsu et al. (2017). With CloudJ, an independent actinic flux calculation for a semi-spherical geometry, besides the existing radiation scheme gets possible. The code of CloudJ is tailored to the specific needs for accurate photolysis rate calculations but is also capable to interact with an existing radiation module (e.g. PSRad-RRTMG). Within the scope of this thesis, CloudJ is mainly used in a standalone configuration without any interaction with the existing radiation module. However, possible ways of interaction could be e.g. the usage of pre-derived gas optical properties by the RRTMG scheme. A first step towards this direction has been shown by (Hsu et al., 2017) and can easily be adapted for ICON-ART as well.

3.2.5 Implementations of chemical tendency linearisation in ICON-ART

It is computational expensive to couple global tropospheric and stratospheric chemical models with global meteorological models. Therefore, it is reasonable, especially at the beginning of the development of a model like ICON-ART, to use simplified parameterisations for the description of selected chemical species. Parameterisations of chemical species can save computational costs and can give a first overview of the general applicability of the model. In addition to parameterisations for chemical tracers, it is useful to define artificial passive tracers to investigate, e.g. transport processes in the atmosphere. As mentioned in section 3.1.4, the equation of motion is written as:

$$\rho \frac{\hat{\mathrm{d}}\hat{\psi}_{\mathrm{g},i}}{\mathrm{d}t} = -\nabla\left(\hat{v}\bar{\rho}\hat{\psi}_{\mathrm{g},i}\right) - \nabla\overline{\rho v \psi''_{\mathrm{g},i}} + P_i + L_i + E_i \tag{3.15}$$

This equation is based on the general continuity equation. The loss L_i of a chemical tracer is defined as a negative tendency. At this point, the production and loss term P_i and L_i are combined in the chemical tendency Γ_i:

$$\rho \frac{\hat{\mathrm{d}}\hat{\psi}_{\mathrm{g},i}}{\mathrm{d}t} = -\nabla\left(\hat{v}\bar{\rho}\hat{\psi}_{\mathrm{g},i}\right) - \nabla\overline{\rho v \psi''_{\mathrm{g},i}} + \Gamma_i + E_i \tag{3.16}$$

where i stands for the respective gaseous chemical tracer in the model.

In the following, the parameterisations for the calculation of Γ_i is introduced for ozone and water vapour. The following descriptions are based on (Schröter et al., 2018).

3.2.6 Chemical tendency of ozone

The ansatz for a simplified description is based on McLinden et al. (2000). The linearisation of the ozone is developed with a special focus on the transport between troposphere and stratosphere. As stated in McLinden et al. (2000), the linearised ozone approach, called *Linoz*, accounts for a more realistic vertical gradient than the provided climatology in the UTLS region. Climatologies are missing chemical and transport tendencies. Thus, gradients that would be established by cross tropopause transport or photochemical losses are not present (e.g. McLinden et al., 2000). The linearised approach can be understood as a first order Taylor expansion of the stratospheric chemical rates. The ozone tendency is linearised with respect to the local ozone mixing ratio, temperature and overhead ozone column density. The algorithm accounts for a more realistic vertical gradient than the provided climatology. For the troposphere, we assume a constant lifetime of 30 days, based on Brasseur and Solomon (2006).

The following differential equation describes the linearised approach:

$$\Gamma_{O_3} = \Gamma_{O_3}^0 + \left.\frac{\partial \Gamma_{O_3}}{\partial \psi_{O_3}}\right|_0 (\psi_{O_3} - \psi_{O_3}^0)$$
$$+ \left.\frac{\partial \Gamma_{O_3}}{\partial T}\right|_0 (T - T^0)$$
$$+ \left.\frac{\partial \Gamma_{O_3}}{\partial c_{O_3}}\right|_0 (c - c_{O_3}^0) \tag{3.17}$$

Here, ψ describes the ozone volume mixing ratio, T the temperature in the respective grid box and c_{O_3} the overhead ozone column. The term $\Gamma_{O_3}(t)$ describes the ozone tendency, in units of ppmv/s at time step t. Climatological values are indicated with the upper script ^{0}. The partial derivative with evaluation at the respective climatological value is marked with a subscript $_0$.

In order to preserve a stable solution of the differential equation 3.17, it is preferable to introduce a steady state mixing ratio $\psi_{O_3}^{ss}$. For the steady state an absence of dynamical tendencies is assumed and the following equation holds:

$$\psi_{O_3}^{ss} = \psi_{O_3}^0 - \left[\Gamma_{O_3}^0 - \left.\frac{\partial \Gamma_{O_3}}{\partial T}\right|_0 (T - T^0) - \left.\frac{\partial \Gamma_{O_3}}{\partial c_{O_3}}\right|_0 (c - c_{O_3}^0)\right] \tau \tag{3.18}$$

with

$$\tau = \left[\left.\frac{\partial \Gamma_{O_3}}{\partial \psi_{O_3}}\right|_0\right]^{-1} \tag{3.19}$$

Thus, the differential equation is reduced to

$$\Gamma_{O_3}(t) = \frac{\psi_{O_3}^{ss} - \psi_{O_3}}{\tau} \tag{3.20}$$

The analytical solution for the tendency $\Gamma_{O_3}(t + \Delta t)$ is:

$$\Gamma_{O_3}(t + \Delta t) = \left(\psi_{O_3}^{ss} - \psi_{O_3}(t)\right)\left(1 - e^{-\frac{\Delta t}{\tau}}\right) \tag{3.21}$$

Values of $\psi_{O_3}^{ss}$ and climatological values are provided using look-up tables. The linearisation represents the photochemical relaxation time for the UTLS. Heterogeneous processes are not taken into account. To address the catalytic destruction by chlorine and bromine

radicals in the presence of polar stratospheric clouds, the linearised ansatz is expanded by an additional loss term:

$$\Gamma_{O_3,\text{psc}}(t + \Delta t) = \psi_{O_3}(t)\left(1 - e^{-\frac{\Delta t}{\tau_{\text{psc}}}}\right) \tag{3.22}$$

Here, τ_{psc} represents the lifetime of ozone in the region where polar stratospheric clouds occur.

For the definition of τ_{psc}, we are following Sinnhuber et al. (2003):

$$\tau_{\text{psc}} = \begin{cases} 10 \text{ days} & \text{for } \vartheta < 92.5° \text{ and } T < 195\text{K} \\ \infty \text{ days} & \text{else} \end{cases} \tag{3.23}$$

with ϑ the solar zenith angle.

3.2.7 Implementation of water vapour tendency due to methane oxidation

The implemented water vapour tendency parameterisation in ICON-ART is presented in this section and is mainly based on Dethof (2003). The study of Simmons et al. (1999) showed that the ECMWF system is capable of a reasonable upward transport velocity in the tropics. Nevertheless, total amounts of water vapour in the stratosphere were too low. Consequently, a parameterisation for the chemical tendency for water vapour was induced. Methane oxidation is a chemical source for stratospheric water vapour. The photodissociation, mainly located in the mesosphere, is an important sink for water vapour in the atmosphere. Observations, shown in Randel et al. (1998) give evidence that water vapour and methane show a constant relation given by:

$$2[CH_4] + [H_2O] = 6.8 \text{ ppmv} \tag{3.24}$$

with $[CH_4]$ and $[H_2O]$ the volume mixing ratios of methane and water vapour. This relation holds for major parts of the stratosphere. As an exception, the antarctic polar vortex should be noted. Very low temperatures are causing the condensation of H_2O (e.g. Bithell et al., 1994) and decrease the water vapour content. The tendency $\Gamma_{H_2O}^{CH_4}$ of water vapour by methane oxidation, given in kg s^{-1} is described by:

$$\Gamma_{H_2O}^{CH_4} = k_1(Q - q) \tag{3.25}$$

with q the specific humidity in kg kg^{-1} and $Q = 4.25 \times 10^{-10} \text{ kg kg}^{-1}$. The value of Q is derived by dividing equation 3.24 by the mol weight of methane (16 g mol^{-1}).

Based on the assumptions on the photochemical life time of water vapour, the variable k_1 can be defined as:

$$k_1 = \frac{1}{86400\tau_1} \tag{3.26}$$

with τ_1 given in days and k_1 in s^{-1}.

Further, τ_1 is defined as

$$\tau_1 = \begin{cases} 100 & p \leq 50 \text{ Pa} \\ 100 + \alpha \frac{\ln\left(\frac{p}{50}\right)^4}{\ln\left(\frac{10000}{p}\right)} & 50 \text{ Pa} < p < 10000 \text{ Pa} \\ \infty & p \geq 10000 \text{ Pa} \end{cases} \tag{3.27}$$

with p the pressure and $\alpha = \frac{19\ln(10)}{(\ln(20))^4}$.

In addition to the stratospheric source by methane oxidation, the mesospheric photodissociation of water vapour is an important sink for water vapour in the atmosphere. The photodissociation sets in for altitudes above $60\,\text{km}$ (or $0.1\,\text{hPa}$).

Based on Brasseur and Solomon (2006), the lifetime of water vapour τ_2 due to photodissociation can be calculated by:

$$\tau_2 = \begin{cases} 3 & p \leq 0.1 \text{ Pa} \\ 100 + 1 + \alpha \frac{\ln\left(\frac{p}{50}\right)^4}{\ln\left(\frac{10000}{p}\right)} & 0.1 \text{ Pa} < p < 20 \text{ Pa} \\ \infty & p \geq 20 \text{ Pa} \end{cases} \tag{3.28}$$

Taking both terms of production and loss into account, the volume mixing ratio of water vapour can be calculated by:

$$\Gamma_{\text{H}_2\text{O}} = \Gamma_{\text{H}_2\text{O}}^{\text{CH}_4} - k_2 q \tag{3.29}$$

with

$$k_2 = \frac{1}{86400\tau_2} \tag{3.30}$$

It can be seen that the large scale dynamics in the Earth's atmosphere, tropical tropopause temperatures, and lower stratospheric water vapour are closely linked to each other by complex feedback processes. By developing an extension of ICON-ART, we want to account for these mechanisms. To investigate the feedback processes of the ART water vapour tracer on, e.g. radiation, only the tendency from the methane oxidation and photodissociation are taken into account. At every model time step, the water vapour mass mixing ratio is set to

the value of the q_v tracer, which is affected by the micro physics routines of ICON. The q_v tracer is the standard water vapour tracer of ICON. Within the ICON-ART routine, the tendency due to methane oxidation and photodissociation can be added. In the last step, q_v is set to the value of ψ_{H_2O}. Within the ICON-ART routine, the tendency due to methane oxidation and photodissociation can be added to this tracer. The changed specific humidity then affects the respective radiation routine.

3.2.8 Description of the parameterisation for age of air tendencies

The characterisation of the BDC is of high importance to get a better understanding of the dynamics and chemical composition of the Earth's atmosphere (e.g Arblaster et al., 2014). It has been shown that temperature changes in the UTLS region seem to modulate the meridional circulation (e.g. Lin and Fu, 2013). The characterisation of stratospheric transport might be difficult since the velocity of the Brewer-Dobson Circulation cannot be accessed directly. It can only be reconstructed by investigating the volume mixing ratio of specific long lived trace gases with life times from a couple of months up to years (e.g. Rosenlof, 1995; Bönisch et al., 2011). One of these species is sulphur hexafluoride (SF_6), which is an anthropogenically emitted chemical compound with a long life time. The increase of the mixing ratio of SF_6 can be assumed as quasi-linear (Maiss and Levin, 1994). In addition, SF_6 has no significant chemical sink within the stratosphere. In the mesosphere, photolytic dissociation at the Lyman-α band and dissociative electron detachment should be taken into account (Ravishankara et al., 1993). We are focusing on the stratosphere and troposphere region, thus both effects are negligible. With this assumption, it is possible to access the quantity of age of air by calculating the difference of SF_6 at a specific model layer and horizontal location with respect to the values when the air has entered the stratosphere. The value of age of air represents the time that an air parcel needs to travel from the tropopause to a specific point in the stratosphere. This is the boundary condition for the value of age of air within the model and enables the calculation of the time-lag when the troposphere showed a specific mixing ratio in the past. Lower boundary conditions are updated every integration time step to simulate a linear increase of SF_6 with time. The increase corresponds to the value of 1 per year. This increase is prescribed for ICON-ART for pressure values above $950\,\text{hPa}$. Using the time lag technique (e.g. Schmidt and Khedim, 1991; Reddmann et al., 2001), one can calculate the age of air tendency as:

$$\psi_{\text{age}} = 7 \cdot 86400 \cdot 365.2425 + \Delta t_{\text{sim}} \tag{3.31}$$

with Δt_{sim} the integration time step of the model given in s. After initialisation, the passive tracer of ψ_{age} is transported. Since the tracer is passive, it shows no interaction with other

tracers or radiation. To neglect deviation from the initial assumption of a strictly linear growth of SF_6, the mean age of air is taken into account for further analysis. For the final calculation, the simulated values are merged with the simulated time to get the actual age of air in years (ψ'_{age}):

$$\psi'_{age} = \frac{t^\star_{sim} - (\frac{\psi_{age}}{86400} - 7 \cdot 365.2425) - t^\star_{init}}{365.2425} \qquad (3.32)$$

where $t^\star_{sim}$ is the simulated time, $t^\star_{init}$ the time of initialisation, both given in the representation of the Julian Day.

In the following, we refer to the mean age of air as the temporal and zonal mean over the age of air distribution.

3.2.9 Implementation of the full gas phase routine

In addition to the existing tracer parameterisations, a full gas phase chemistry approach was implemented for ICON-ART in the scope of this thesis.

Construction of the full gas phase chemistry approach is done using the comprehensive and flexible atmospheric chemistry module MECCA (Module Efficiently Calculating the Chemistry of the Atmosphere; Sander et al., 2011a). MECCA provides a set of chemical reactions covering the troposphere as well as the stratosphere. The base version of MECCA is extendable by own chemical reactions or an update of rate coefficients.

The MECCA preprocessing part has been extended by a routine constructing the XML file for the tracer module of ICON-ART. The numerical flexibility of MECCA is based on the KPP software (Kinetic PreProcessor; Sandu and Sander, 2006). KPP generates Fortran90 code which is used to solve the differential equations based on the given chemical reaction. This is the first step which is needed for KPP and thus for MECCA. In a second step, the numerical integrator is chosen. For our example, the Rosenbrock solver of the third order (Sandu et al., 1997) is used. In the third step, the driver part of MECCA is used. The driver stands for the main program which calls the integrator, reads input data sets, and writes the results in the original MECCA model. Within ICON-ART this step is replaced by routines of ICON and ICON-ART. Only the integrator call element is maintained. Technical work has been done to ensure that a dictionary, in the scope of the flexible tracer framework gets accessible for the translation between four dimensional chemical tracers in ICON-ART and one dimensional concentrations of chemical species in the KPP routines.

Additionally, other chemical reaction mechanisms provided by MECCA can be used within ICON-ART without changes in the program code itself. It is sufficient, to read the new tracer XML file generated by the MECCA preprocessor. Finally, all standard reactions
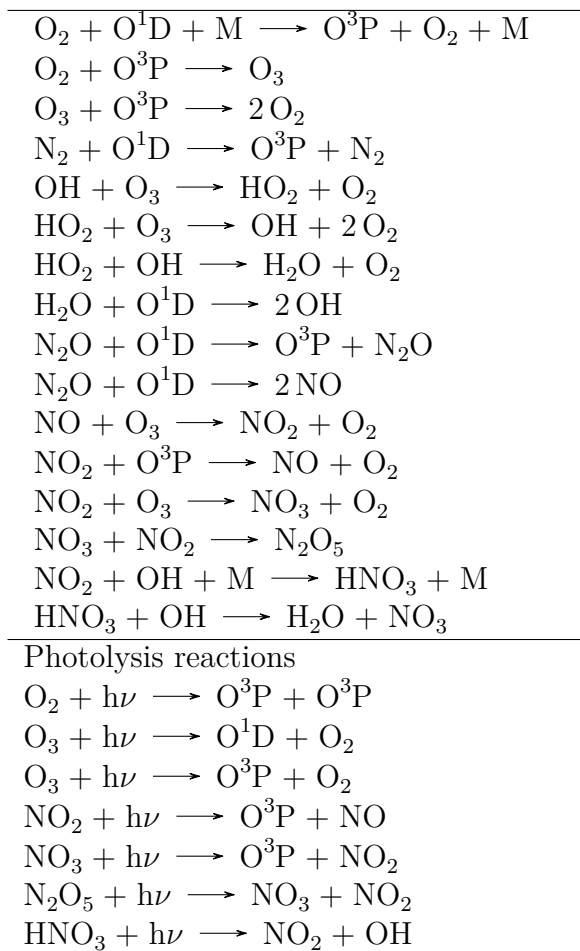
$$O_2 + O^1D + M \longrightarrow O^3P + O_2 + M$$
$$O_2 + O^3P \longrightarrow O_3$$
$$O_3 + O^3P \longrightarrow 2\,O_2$$
$$N_2 + O^1D \longrightarrow O^3P + N_2$$
$$OH + O_3 \longrightarrow HO_2 + O_2$$
$$HO_2 + O_3 \longrightarrow OH + 2\,O_2$$
$$HO_2 + OH \longrightarrow H_2O + O_2$$
$$H_2O + O^1D \longrightarrow 2\,OH$$
$$N_2O + O^1D \longrightarrow O^3P + N_2O$$
$$N_2O + O^1D \longrightarrow 2\,NO$$
$$NO + O_3 \longrightarrow NO_2 + O_2$$
$$NO_2 + O^3P \longrightarrow NO + O_2$$
$$NO_2 + O_3 \longrightarrow NO_3 + O_2$$
$$NO_3 + NO_2 \longrightarrow N_2O_5$$
$$NO_2 + OH + M \longrightarrow HNO_3 + M$$
$$HNO_3 + OH \longrightarrow H_2O + NO_3$$

Photolysis reactions
$$O_2 + h\nu \longrightarrow O^3P + O^3P$$
$$O_3 + h\nu \longrightarrow O^1D + O_2$$
$$O_3 + h\nu \longrightarrow O^3P + O_2$$
$$NO_2 + h\nu \longrightarrow O^3P + NO$$
$$NO_3 + h\nu \longrightarrow O^3P + NO_2$$
$$N_2O_5 + h\nu \longrightarrow NO_3 + NO_2$$
$$HNO_3 + h\nu \longrightarrow NO_2 + OH$$

Table 3.5: Summary of the chemical reactions used for the extended Chapman cycle simulation.

schemes provided by MECCA are accessible in ICON-ART, by only using MECCA as an external preprocessor. The model has to be recompiled once, but the user does not have to perform changes in the program code. Files that are changed by the preprocessor are copied to the respective ICON-ART source code directory automatically.

In the scope of this thesis, a chemical reaction mechanism based on the extended Chapman cycle is used to demonstrate the functionality of the ICON-ART gas phase routine. The reactions of the extended Chapman cycle are shown in Table 3.5.

4 The quantification of cloud impact on photolysis rates

For the near-realistic simulation of atmospheric chemistry it is of huge importance to get a better knowledge about the impact of clouds on photolysis rates. In general, photolysis rates play an important role for atmospheric chemistry, most importantly for ozone production in the upper troposphere. Tropospheric oxidation by the OH radical leads to an increase of ozone. The basic approach is to assume that in the ultraviolet region, the most important photochemical wavelength region for the UTLS region, radiation is reduced below clouds. Above the top of the cloud, radiation is assumed to be enhanced due to back-scattering by up to $12\% - 13\%$ (Tie et al., 2003). In contrast to the work of Tie et al. (2003), the studies of Liu et al. (2006, 2009) limit this strong influence on the total impact of clouds on photolysis rates. In this study, photolysis rates are reported to change less than 4% in case of JO^1D and JNO_2 when clouds are present. This leads to a variation of tropical tropospheric ozone of about 5%. The authors also point out that there are enormous differences between different model simulations (ranging from 5% up to 30% of cloud induced enhancement). Models used in both studies are GEOS-CHEM (Bey et al., 2001) with CloudJ (here named FastJX) (Bian and Prather, 2002) as the photolysis module and MOZART-2 (Brasseur et al., 1998) with FTUV (Madronich, 1987). The general knowledge about the influence of clouds on photolysis rates is not completely evolved, as stated by Tie et al. (2003). Only a few other studies by Thompson (1984); Madronich (1987) and Jacob et al. (1989) focus on the characterisation of cloud impact. Nevertheless, all studies agree on the high importance of the accurate simulation of the impact. The studies agree on the fundamental principle that regions below clouds show decreased photolysis rates. Cloud droplets of a big radius compared to the incoming wavelength and ice particles are highly scattering. The backscattering fraction of the incoming radiation enhances the photolysis rates above a cloud. However, the quantification of the actual amount of increase and enhancement of photolysis rates due to the cloud impact is still under recent discussion (Prather, 2015).

Due to the strong impact on different atmospheric conditions, the realistic simulation of atmospheric ozone concentrations requires an online photolysis module for model simulations. An online photolysis module takes the varying atmospheric conditions like, e.g. liquid water

path and overhead ozone column, into account. Offline modules often use tabulated clear sky photolysis rates and apply modifications in the presence of clouds by the multiplication with predefined factors from standard scenarios.

The most commonly used online photolysis rate modules in global models are the TUV model (Madronich, 1987) and CloudJ (Prather, 2015; Hsu et al., 2017). For the ICON-ART model, the CloudJ model has been included as the photolysis module. The original name of this model has been changed with every new version. Due to that, in the following, the latest version of this module is referenced as CloudJ. For the cloudy sky simulations with ICON-ART, the approach of Briegleb (1992) is used to simulate the impact overlapping cloud layers most efficiently (Feng et al., 2004). In this approach, the cloud fraction f is modified to $f^{3/2}$. Here, the cloud fraction is defined as the diagnosed fraction of a grid box in the model covered with clouds.

The development of the chemistry module of ICON-ART started with the development of the photolysis module. CloudJ was chosen, because this module provides the calculation of photolysis rates for the important wavelength region of the UTLS. Without a suitable module for photolysis rate calculation, the realistic simulation of the chemical composition of the atmosphere would be impossible.

The following sections focus on the validation of CloudJ in ICON-ART. In the first section the validation is performed for a standalone box model. In the second section, aircraft campaign data are used to show the reasonable photolysis rate calculation in the modelling system ICON-ART.

4.1 Evaluation of photolysis rate calculations with CloudJ

In order to classify the calculation of photolysis rates of selected species relevant in the troposphere and lower stratosphere, these rates are compared to those being calculated in a former photolysis rate comparison, performed by the MOD (IMK-ASF; KIT) group. For this study, different photolysis codes in 3D-CTMs are used. These are the following:

1. KASIMA – (Röth, 2002)

2. REPROBUS – (Madronich and Flocke, 1999)

3. SLIMCAT – (Lary and Pyle, 1991)

4. TM5 – (Landgraf and Crutzen, 1998)

Absorption cross sections and quantum yields in these models are mainly chosen from DeMore et al. (1997) for REPROBUS and TM5. Slimcat used cross sections and quantum yields mainly from JPL Sander et al. (2000) (SLIMCAT). For KASIMA, individual resources

were selected, for more information see e.g. Röth (2002). In addition to that, CloudJ data from Sander et al. (2006) with some custom adoptions is used. For all studies, the surface albedo was prescribed to 0.31, the albedo for grass land and ozone concentrations, temperature and pressure profiles were obtained from the US Standard Atmosphere (atm, 1976). This leads to a general independence of the result of the photolysis rate calculation from input values.
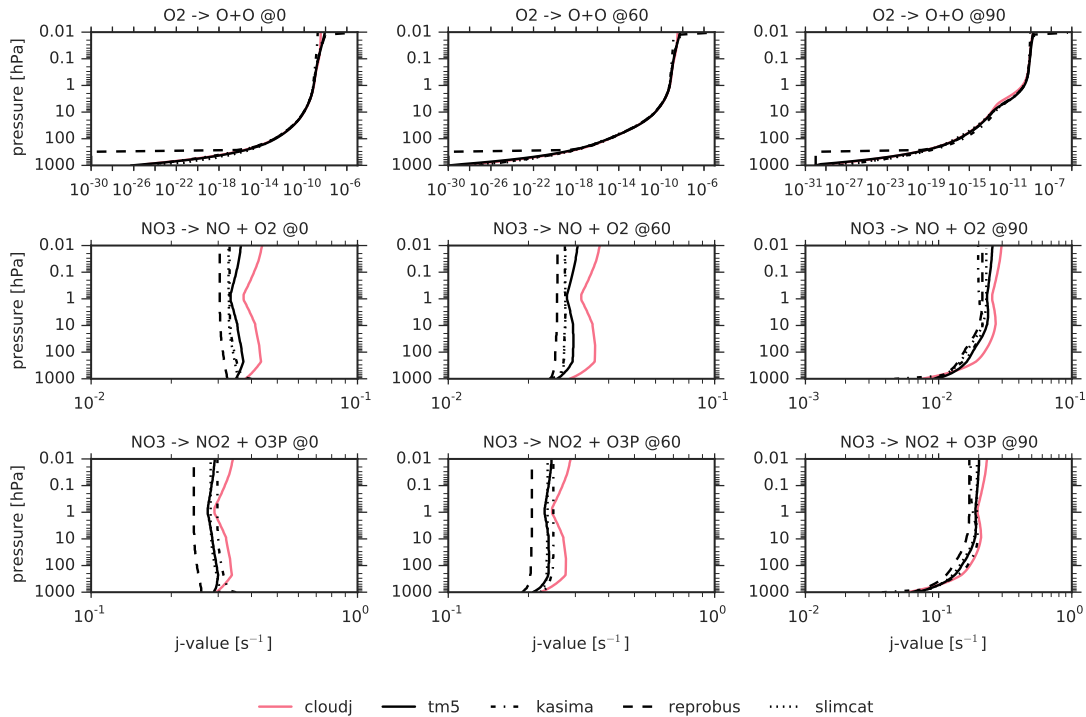

Figure 4.1: Pressure dependent photolysis rates (x-axis) calculated by four different photolysis codes within 3D-CTMs (black colour and different line styles) and CloudJ (red) with pressure dependence (y-axis). From left to right: increasing solar zenith angle (0°, 60° and 90°). Upper row: photolysis rate of O_2, middle row: photolysis rate of first channel of NO_3 and lower row: the second channel of NO_3.

Figure 4.1, 4.2 and Figure 4.3 show photolysis rate calculation for altitudes from ground to 100 km for six different photolysis rates, and for three selected solar zenith angles. Two of the photolysis rates show two different photolytic channels. The selected species represents discriminative altitude regions. For example, the photolytic dissociation of O_2 to O and O has a sufficient probability for a wavelength region smaller than 300 nm at 240 nm, which corresponds to altitudes above 20 km (for comparison see Figure 2.7). This is also reflected in the altitude dependence of the photolysis rate. One can see that for altitudes greater than 20 km the photolysis rate is rapidly increasing for higher altitudes for all shown solar zenith angles. The photolysis rates of O_2 represents the stratosphere region, as well as the O^1D channel of O_3 and N_2O. The other photolysis reactions may also occur in the troposphere region.
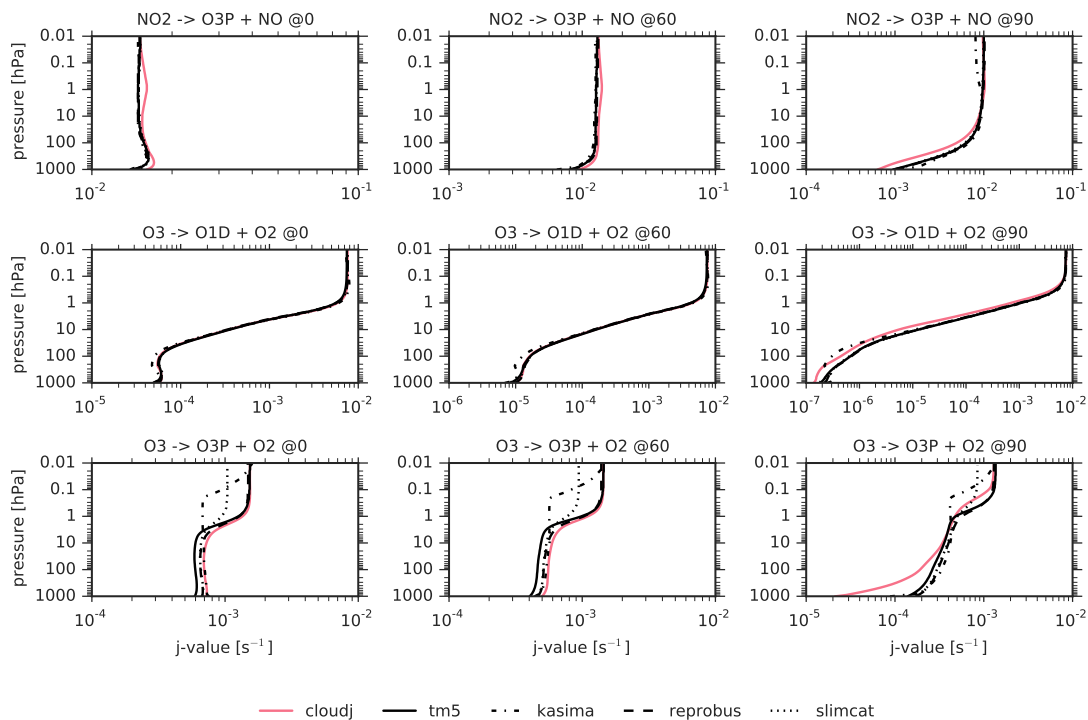
Figure 4.2: Same as Figure 4.1. Upper row: photolysis rate of NO_2, middle row: photolysis rate of O_3 to O^1D and lower row: O_3 to O^3P.
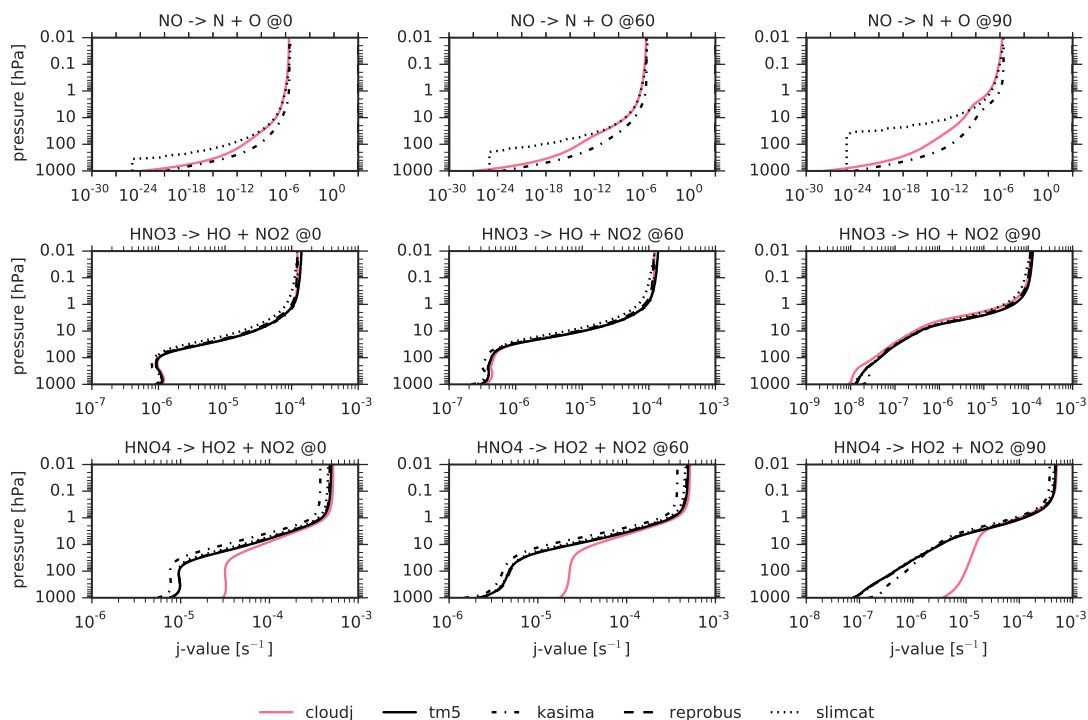
Figure 4.3: Same as Figure 4.1. Upper row: photolysis rate of NO, middle row: photolysis rate of HNO_3 and lower row: HNO_4

This comparison shows a general agreement of photolysis rates between the different models of most substances. Occurring deviations can be explained by differences within the radiation transfer models, the non-equal incoming solar flux on top of the model atmosphere, and especially the usage of different absorption cross sections and quantum yields. The latter contributes most to the observed deviation of photolysis rates. The photolysis rate of O_3, for the channel leading to O^3P shows much lower photolysis rates for CloudJ than the other models. This is only observed for high solar zenith angles. Figure 4.3 shows an overestimation of the photolysis rate of HNO_4, for all three solar zenith angles below the pressure of $10\,\mathrm{hPa}$. The latter deviation might be caused by a different absorption cross section or by the temperature dependence of CloudJ compared to the other models. The deviation for O_3 to O^3P can not be explained by that since the high difference to the other models only occurs for high solar zenith angles. However, at this point of this analysis, CloudJ seems to be capable of calculating photolysis rate in the UTLS region. All species, either representing the troposphere or the stratosphere, show an overall agreement in their photolysis rate profile for all altitudes.

4.2 Validation of ICON-ART photolysis rates

This section focuses on the validation of the online calculated photolysis rates within ICON-ART. The validation is performed using measurements of the TORERO campaign, conducted at the beginning of 2012 over the region of Costa Rica. TORERO stands for Tropical Ocean tRoposphere Exchange of reactive halogen species and Oxygenated VOC. In the months of January and February, the time of high biological ocean activity in the tropics, the instruments on the aircraft collected remote sensing and in-situ data. The aircraft was the NSF/NCAR with the Gulfstream-V High-performance Instrumented Airborne Platform for Environmental Research (GV HIAPER).

Photolysis rates were not measured directly. On the aircraft, actinic flux measurements were taken using the GV HARP instrument. HARP stands for HIAPER Airborne Radiation Package. It is used to measure spectrally resolved actinic flux and horizontally stabilised irradiance. Measurements of the spectroradiometers provide in situ down- and up-welling actinic flux density spectra. The wavelength range is approximately $280\,\mathrm{nm}$ to $680\,\mathrm{nm}$ at a sampling frequency of up to $1\,\mathrm{Hz}$. As noted in the data description, photolysis rates were calculated from the actinic flux data using a modified version of the ACD TUV model (Madronich, 1987). The calculation is performed using equation 2.40.

$$j_{\mathrm{X}}(\tau) = \int_{\lambda_{\min}}^{\lambda_{\max}} \underbrace{\sigma_{\mathrm{X}}(\lambda)}_{\text{cross section}} \cdot \underbrace{\Phi_{\mathrm{X}}(\lambda)}_{\text{quantum yield}} \cdot \underbrace{I_{\mathrm{A}}(\tau, \mu, \phi, \lambda)}_{\text{actinic flux}} \, \mathrm{d}\lambda \qquad (2.41)$$

Selection of photolysis rates for comparison

For the direct comparison between measurements and modelled results, one has to keep in mind, that even if the calculated actinic flux matches perfectly, cross sections and quantum yields can still differ. The TORERO data product only consists of the end product - the photolysis rates, not the actinic flux itself. The calculated photolysis rates are referred to as measurements, for simplicity. The list of measured photolysis rates is given in Table 4.1.

The uncertainty of the measured actinic flux can be estimated to be $5 - 7\%$ (e.g. Bohn et al., 2008). Accuracy is limited due to errors in the actinic flux calibration. This depends on the detector sensitivity and wavelength calibration. In addition to that, spectral properties of the spectrometer have to be taken into account, e.g. band-pass resolution, stray-light rejection and wavelength accuracy.

Since the photolysis rates $J[O_3 \longrightarrow O_2+O^1D]$, $J[NO_2 \longrightarrow NO+O^3P]$, $J[HNO_3 \longrightarrow OH+NO_2]$ and $J[N_2O_5 \longrightarrow NO_3+NO_2]$ are of high importance for the tropospheric and stratospheric chemical reactions containing OH radicals, the analysis in the following section is limited to these photolysis rates.

Table 4.1: Overview of measured photolysis rates, the term Products summarises all possible products of the photolysis reaction.

O_3	$\xrightarrow{h\nu}$	O_2	$+ O^1D$
NO_2	$\xrightarrow{h\nu}$	NO	$+ O^3P$
N_2O_5	$\xrightarrow{h\nu}$	NO_3	$+ NO_2$
H_2O_2	$\xrightarrow{h\nu}$	$2\,OH$	
HNO_2	$\xrightarrow{h\nu}$	OH	$+ NO$
HNO_3	$\xrightarrow{h\nu}$	OH	$+ NO_2$
CH_2O	$\xrightarrow{h\nu}$	H	$+ HCO$
CH_2O	$\xrightarrow{h\nu}$	$H2$	$+ CO$
CH_3CHO	$\xrightarrow{h\nu}$	CH_3	$+ HCO$
C_2H_5CHO	$\xrightarrow{h\nu}$	C_2H_5	$+ HCO$
$CHOCHO$	$\xrightarrow{h\nu}$	CH_2O	$+ CO$
$CHOCHO$	$\xrightarrow{h\nu}$	HCO	$+ HCO$
$CHOCHO$	$\xrightarrow{h\nu}$	H_2	$+ 2\,CO$
CH_3COCHO	$\xrightarrow{h\nu}$	Products	
CH_3COCH_3	$\xrightarrow{h\nu}$	CH_3CO	$+ CH_3$
CH_3OOH	$\xrightarrow{h\nu}$	CH_3O	$+ OH$
CH_3ONO_2	$\xrightarrow{h\nu}$	CH_3O	$+ NO_2$
PAN	$\xrightarrow{h\nu}$	CH_3COO_2	$+ NO_2$
$CH_3CH_2CH_2CHO$	$\xrightarrow{h\nu}$	C_3H_7	$+ HCO$
$CH_3CH_2CH_2CHO$	$\xrightarrow{h\nu}$	C_2H_4	$+ CH_2CHOH$
$CH_3COCH_2CH_3$	$\xrightarrow{h\nu}$	Products	
$CH_3CH_2ONO_2$	$\xrightarrow{h\nu}$	Products	
HO_2NO_2	$\xrightarrow{h\nu}$	HO_2	$+ NO_2$
HO_2NO_2	$\xrightarrow{h\nu}$	OH	$+ NO_3$
$BrCl$	$\xrightarrow{h\nu}$	Br	$+ Cl$
$HOBr$	$\xrightarrow{h\nu}$	HO	$+ Br$
BrO	$\xrightarrow{h\nu}$	Br	$+ O$
Br_2	$\xrightarrow{h\nu}$	$Br\ + Br$	
Br_2O	$\xrightarrow{h\nu}$	Products	
$BrONO_2$	$\xrightarrow{h\nu}$	Br	$+ NO_3$
$BrONO_2$	$\xrightarrow{h\nu}$	BrO	$+ NO_2$
$ClONO_2$	$\xrightarrow{h\nu}$	Cl	$+ NO_3$
$ClONO_2$	$\xrightarrow{h\nu}$	ClO	$+ NO_2$
Cl_2	$\xrightarrow{h\nu}$	Cl	$+ Cl$
$CHBr_3$	$\xrightarrow{h\nu}$	Products	

In addition to the importance of the selected photolysis reaction for the chemistry in the UTLS region, described in section 2.3, the cross sections of these photolysis rates cover up different wavelength regions of interest. Thus, the dependence of photolysis rates on the wavelength region can be further investigated.

The dependence of the cross sections on wavelengths is depicted in Figure 4.4, based on data used in Sander et al. (2011b). The four different species represent four different characteristics of wavelength dependence. Whereas N_2O_5 is characterised by a nearly exponential dependence for the region between 200 nm to 400 nm for 200 K to 400 K, the cross section of NO_2 shows a bell shape, with a peak at 400 nm. The most detailed characteristic is shown by the O_3 cross section dependence. The weaker Huggins band lies between 310 nm and 340 nm (Liou, 2002). The Huggins band is followed by the Chappuis Band, with a maximum around 575 nm.

A photolysis module for the accurate simulation of photolysis rates in the UTLS region, represented by these four, has to reproduce this dependence. The photolysis module CloudJ has the advantage compared to other photolysis routines that is includes the wavelength region from 170 nm up to 778 nm.
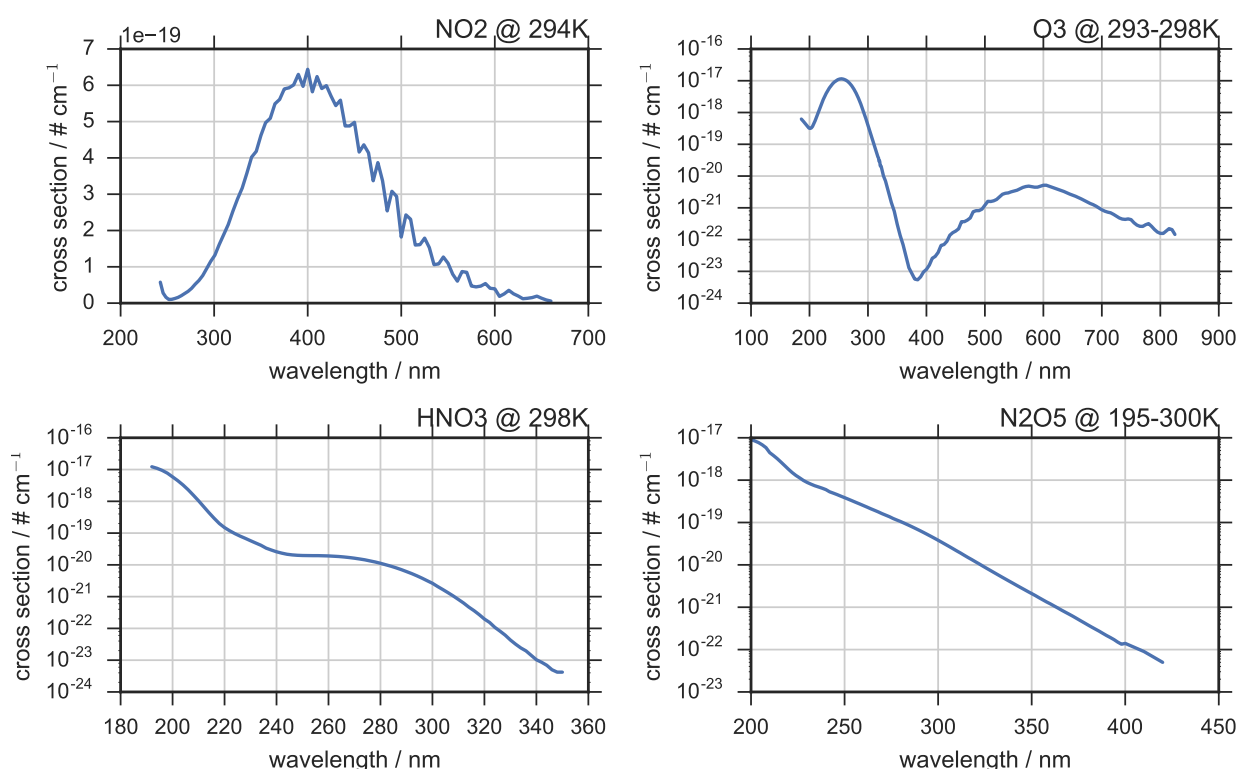
Figure 4.4: Overview of wavelength dependence of cross sections for four selected species. The data is mainly taken from Sander et al. (2011b). For every species, the respective wavelength region is depicted on the x-axis, different for every species. This is done to emphasise the difference between them.
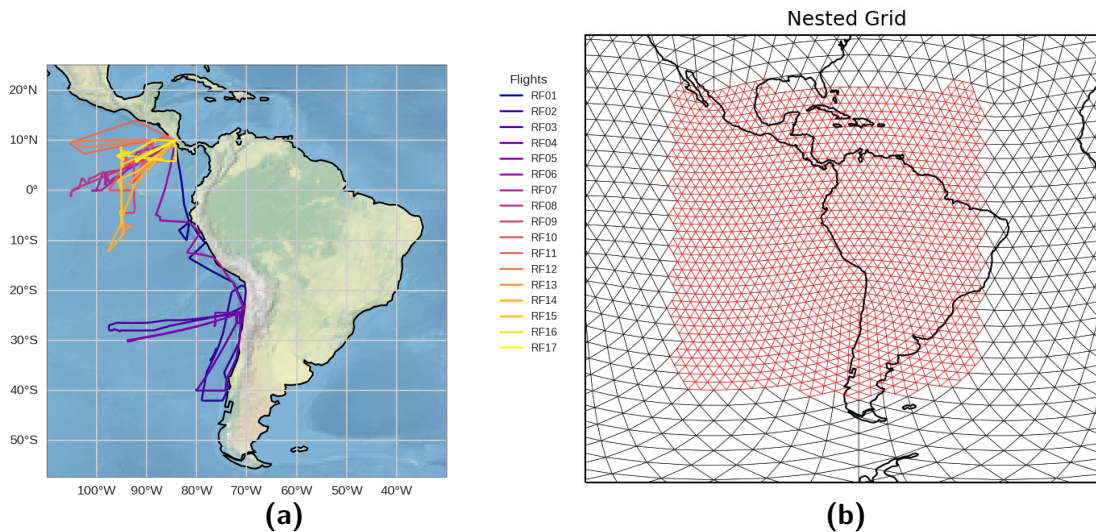
Figure 4.5: a) Overview of all TORERO flights between 2012-01-19 and 2012-02-26. Maximum (North) Latitude: 10.00°, Minimum (South) Latitude:−40.00° Minimum (West) Longitude: −105.00°, Maximum (East) Longitude: −70.00°; b) Schematic depiction of the location of the nest in the simulated model domain.

4.2.1 TORERO campaign overview and simulation setup

The aim of this investigation of photolysis rates against measurements is to answer the question: Are we able to simulate photolysis rates in a reasonable way? Reasonable means, that the algorithm is able to show the correct impact when clouds are present and a realistic solar zenith angle dependency. The simulations were performed on a R2B6 grid with a horizontal grid resolution of approximately $40\,km$. The aircraft had an average speed of $250\,m\,s^{-1}$. This means, that measurements can be assigned for at least $180\,s$ to one corresponding model grid box. In case of homogeneous cloud fields, it can be assumed that there is a one-to-one match between ICON-ART and the real situation during the measurement. This is not the case for fractional cloud fields. The presumption for an algorithm to calculate photolysis rates is the following: Above a cloud, photolysis rates are enhanced and below reduced. To test this presumption, two kind of simulations were performed:

- 1. clear-sky simulations

- 2. cloudy-sky simulations

In the clear-sky simulation, the influence of clouds was switched off. The cloudy-sky simulation takes optical properties, diagnosed by the respective routines of ICON into account. The overhead ozone column is taken from the standard ozone climatology of ICON. For both simulations, no aerosol impact was taken into account.

To investigate the influence of the horizontal resolution on the simulation of photolysis rates in different wavelength regimes, a nest in the region of interest is introduced. Thus, the simulations (clear sky and cloudy sky) are performed on the global R2B6 grid with a R2B7 nest (20 km horizontal grid spacing) The schematic depiction of this nest is shown in Figure 4.5b. The nest has the position and extent to fit the same region as covered during the campaign, depicted in Figure 4.5a. By the introduction of nesting, more accurate information about the cloud impact on photolysis rates should be gained within one model run. The location of clouds and their optical properties can vary with horizontal and vertical resolution. Especially in the tropical region, where the campaign took place, fractional cloud fields are expected. These fragments are smaller than the horizontal resolution of the global domain (40 km horizontal grid spacing). Thus, the higher resolution of the nested domain is more suitable for simulating the meteorological conditions during the campaign.

As an example, the timeseries of flight RF01 has been chosen. Between 14UTC and 16UTC, the plane was flying at a constant pressure altitude of about 200 hPa. The clear-sky photolysis rate, marked in solid blue, is about $1.2 \times 10^{-2}\,\mathrm{s}^{-1}$ during that episode. There is no significant variation during that time span. In the cloudy-sky simulation, marked in solid red, the photolysis rate is enhanced by about 100%. The cloudy-case results fit much better to the observation. Remaining differences can be explained by the fact that cloud optical properties between measurement and simulation do not fit completely. The previous prerequisite, for the algorithm to show a reasonable reaction in the presence of clouds, is fulfilled for flight RF01.

4.2.2 Construction of data categories

For the further investigation of the comparability between ICON-ART and the measurements, it is reasonable to introduce data categories. There are two main categories: The cloud free and the cloudy category. The cloud free or flagged category is constructed taking only points into account, where no clouds are present, neither in the measurement nor in the simulation. All other datapoints are assigned to the cloudy category. For the simulation, the presence of clouds is indicated by the diagnostic output for convective clouds. The value of the variable $htop\_conv = -500\,\mathrm{m}$ is set by the diagnostics interface of ICON-ART, where no convection is diagnosed. For the construction of the data category, the interpolation impact has to be taken into account. The value of the interpolated time series could slightly differ from the value of $-500\,\mathrm{m}$ but would always be negative. This is caused by the interpolation technique, described in the next section. In addition, there is a cloud flag product constructed from the measurement data. This cloud flag has values of zero for cloud free and one for cloudy conditions. The flag is constructed using the colour index of the forward viewing telescope on the aircraft and visual inspection of the video footage. During the flight, photographs were taken left, right, above and below the aircraft. If

the cloud flag is zero at a specific point and no cloud was diagnosed in the simulation, marked by a value of htop_conv$< 0\,$m, this data point falls into the cloud free category. All other datapoints are members of the cloudy category. An example of how to build
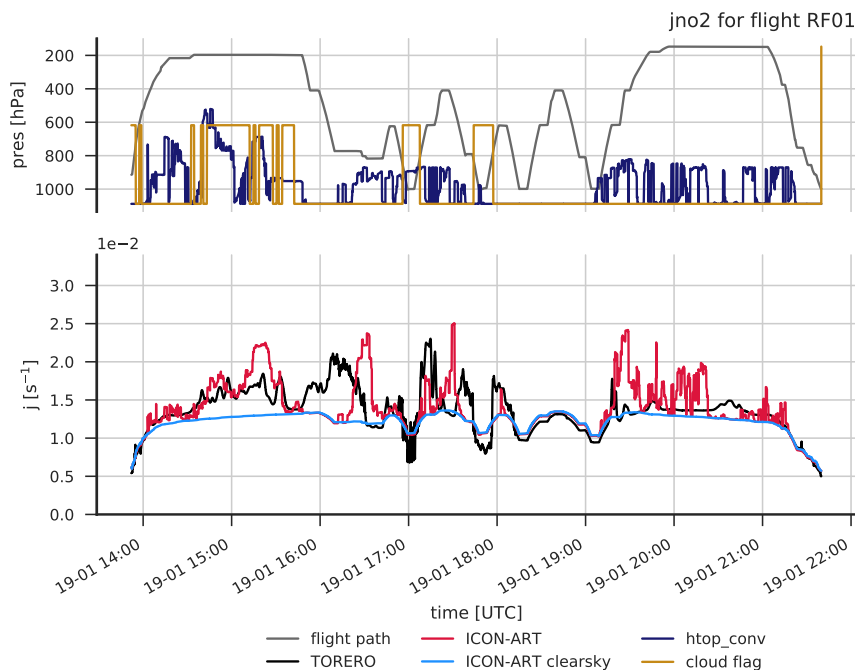

Figure 4.6: Timeseries of measured (solid black) and simulated photolysis rates for JNO_2. The upper panel shows the flight altitude in hPa of the aircraft, on the y-axis and the time is given in UTC on the x-axis. Additionally, the manually constructed cloud flag (orange), and the diagnostic cloud top height is shown (dark blue). The photolysis rates are given in units of $1 \times 10^{-2}\,s^{-1}$. The solid red line represents the timeseries for the cloudy-sky simulation, the light blue line the clear-sky simulation.

up these two categories can be seen in Figure 4.7 for flight RF01. Between 18 UTC and 19 UTC, the cloud flag of the measurement (orange) indicates cloud free conditions. The cloud top height of ICON-ART (blue) indicates a cloudy case, thus the timeseries points falling in this region are marked with a dark grey background in the bottom panel. Flight RF01 is a typical example for a mainly cloudy category. This is also an example, where the manually constructed cloud flag for the measurement seems to be wrong since the photolysis rates increase. It is seen in both, measurement and simulation in contrast to the clear sky simulation. Analysing the video footage also stresses the argument that the manually constructed cloud flag is not sufficient enough for a standalone test criteria.
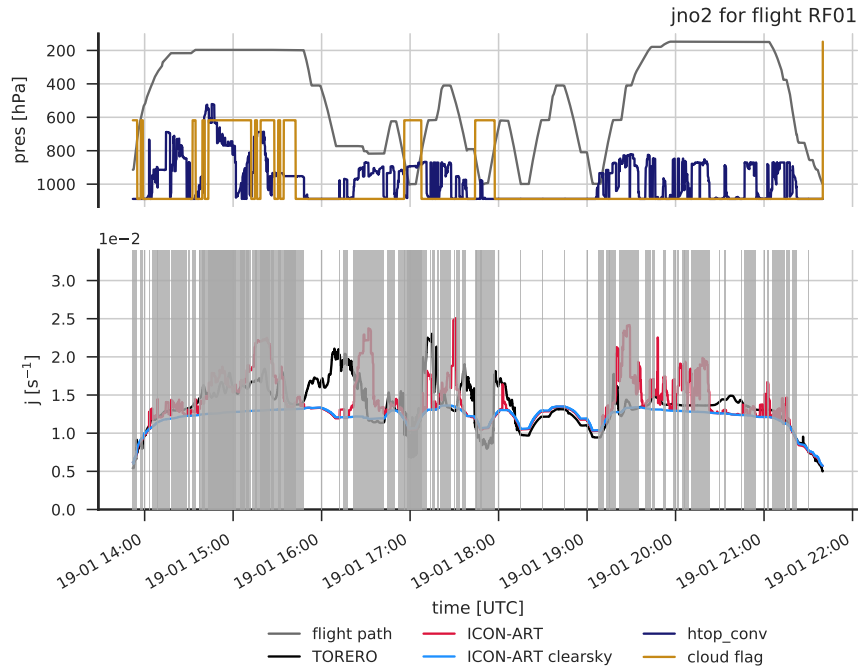
Figure 4.7: Same as Figure 4.6. In addition, grey areas included for the timeseries mark the cloudy category.

4.2.3 Impact of the horizontal resolution on photolysis rate simulations

In the following, the influence of the horizontal resolution in the model on the comparability between simulation and measurement is investigated. In both experiments, the datasets of measurement and simulation are split into the two categories, cloud free and cloudy data, as described before. The unflagged dataset contains all the datapoints and the flagged dataset only the cloud free datapoints. By this categorisation it is possible to characterise not only the influence of the different resolution but also the different results for datapoints affected by clouds and clear sky points.

The model output was chosen to be every $\Delta t = 300\,\mathrm{s}$, measurements were taken with $\Delta t = 1\,\mathrm{s}$. In order to get a more accurate dataset for the comparison study, both datasets are sampled onto the same resolution of $\Delta t = 1\,\mathrm{s}$ and then the moving average over $300\,\mathrm{s}$ is applied. The sampling does not include any kind of interpolation.

The first $300\,\mathrm{s}$ and the last $300\,\mathrm{s}$ for each flight are excluded, since this timespan represents starting and landing episodes. During these episodes, differences based on the orography or surface albedo between simulation and measurement might affect the analysis. After the starting episode, the flight path was located over water, meaning influences of the orography vanish and a constant albedo of 0.07 can be assumed. This value for the albedo is the

standard constant value for the ocean surface. For the TORERO campaign, the same value has been assumed.

Data points on the unstructured triangular grid of ICON-ART are interpolated horizontally by using the nearest neighbours interpolation method. The choice of three nearest neighbours has been proven to be an appropriate choice (Bentley, 1975). Also, time and vertical dimension are interpolated by this technique. Due to the regular spacing in both horizontal dimensions, the nearest neighbours interpolation method is equivalent to a common linear interpolation in this case.

Figure 4.8 shows the histogram and kernel density function for the simulation (red) and measurement (black), for the unflagged category in the global domain. Figure 4.9 shows the results for the nested domain. Here, also all datapoints are taken into account.

For the analysis, the kernel density is calculated using a Gaussian kernel density estimator (KDE) with

$$f(x) \;=\; \frac{1}{nh}\sum_{i=1}^{N} K\left(\frac{x - x_i}{h}\right) \tag{4.1}$$

with

$$K = g(x) \;=\; \frac{1}{\sigma\sqrt{2\pi}} e^{-\frac{1}{2}\left(\frac{x}{h}\right)^2} \tag{4.2}$$

$$h \;\approx\; 3.49\sigma N^{\frac{1}{3}} \tag{4.3}$$

where N is the number of datapoints, x is a point at which the KDE is evaluated with x_i, a subset of points from the complete dataset of length N. The KDE is controlled by the bandwidth h. In this case, the bandwidth is estimated with Scott's rule (Scott, 1979). The variable σ is the standard deviation of the dataset. The choice of the bandwidth estimator and KDE is appropriate for normally distributed data. The bandwidth calculation by Scott (1979) aims for minimisation of the integrated mean square error.

The cumulative density function (CDF)

$$C(f) \;=\; \int_{-\infty}^{x} f(x)\mathrm{d}x' \tag{4.4}$$

is used to calculate the median, given by the 50th percentile of the CDF.

Both Figures, Figure 4.8 and 4.9 show a high similarity in the shape of the KDE for the simulation for all four photolysis rates. This means that there a no systematic differences in the statistical distribution between the nested and global domain for photolysis rate calculation. The statistical distribution of photolysis rates is important for global chemistry-

climate simulations. This comparison also shows that the horizontal resolution does not affect the reliability of the photolysis rate calculation with ICON-ART. On the other hand, it could be beneficial to decrease computational costs by defining a region of interest for photolysis rate calculation. By investigating the differences between the results for the nested and global domain in more detail, differences for the statistical parameters, e.g. the median and bandwidth become more present. In the following, the KDEs and the statistical parameters for the simulation and the measurement are discussed in more detail.

For the unflagged category, the results of the KDEs for simulation and measurement, shown in Figure 4.8 for the global domain, seem to have a comparable shape. This means that the general characteristics of the underlying distribution of datapoints is represented similarly. The characteristic of the distribution is defined by solar zenith angle dependency, overhead ozone column dependency or altitude dependency (due to temperature dependency). It is important that the simulation is able to represent these dependencies realistically. The shape of the KDE function, determined by the bandwidth h is more similar for the photolysis
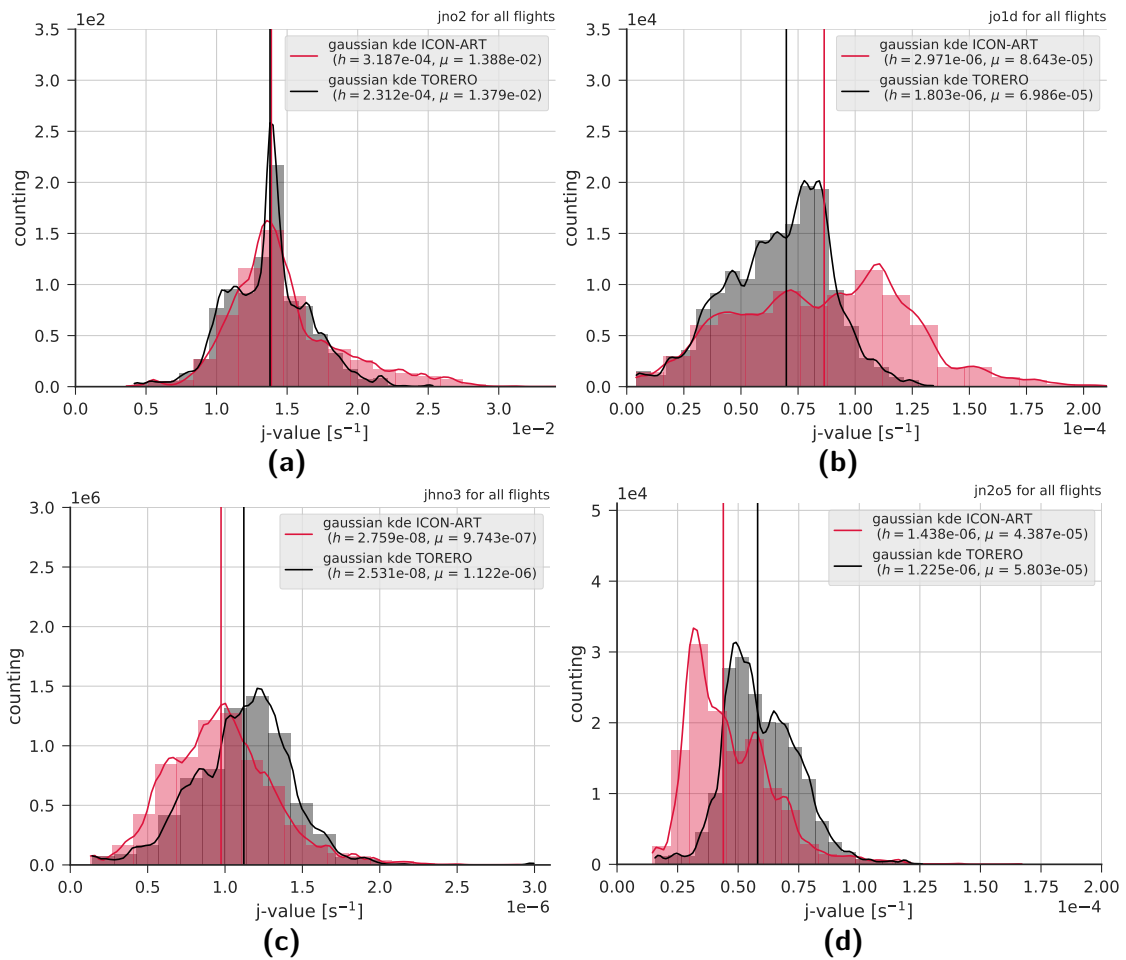
Figure 4.8: Analysis of measured (black) and simulated (red) KDEs of (a): JNO_2, (b): JO^1D, (c): $JHNO_3$, (d): JN_2O_5, the red and black vertical line marks the calculated median based on the Gaussian kernel. Datapoints are taken from the global domain, no flagging applied.
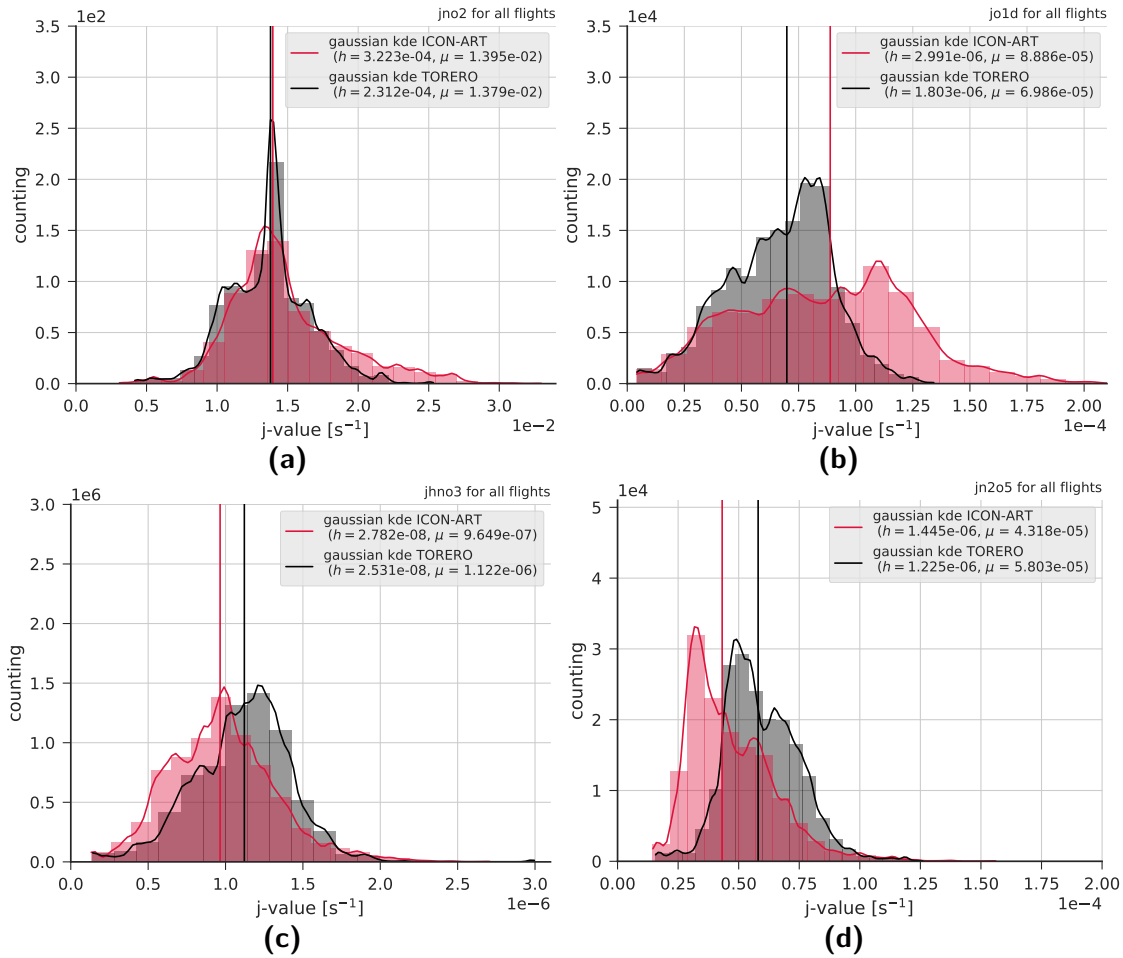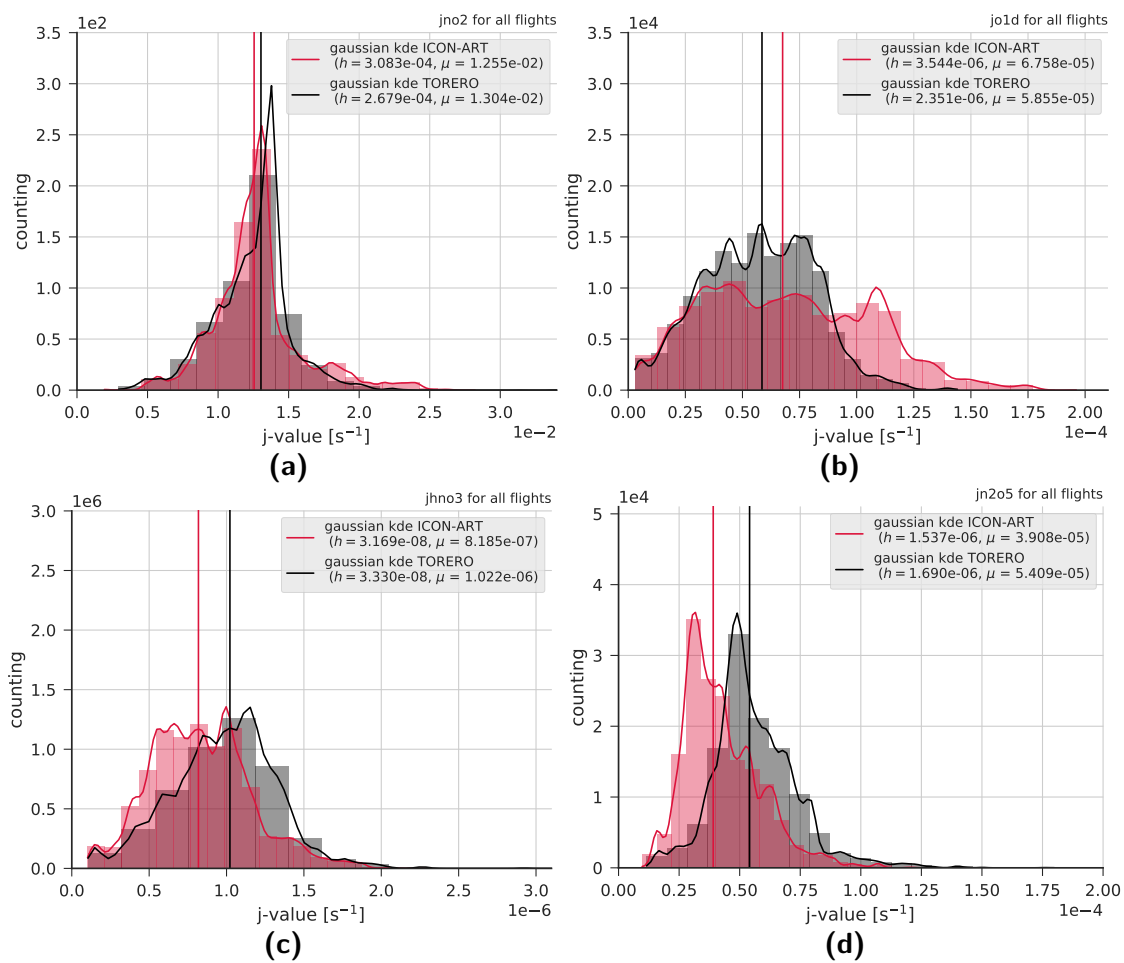
Figure 4.9: Analysis of measured (black) and simulated (red) KDEs of (a): JNO_2, (b): JO^1D, (c): $JHNO_3$, (d): JN_2O_5, the red and black vertical line marks the calculated median based on the Gaussian kernel. Datapoints are taken from the nested domain, no flagging applied.

rates of JNO_2, JN_2O_5 and $JHNO_3$ than for JO^1D, in comparison between measurement and simulation. For the latter, the calculated bandwidths show a relative difference of 65 %. The photolysis rate of JO^1D is much more affected by the overhead ozone column, than the others. This conclusion can also be drawn from the absorption cross section spectrum, see Figure 4.4.

For JNO_3, the shape of the KDE and also the calculated median are in close correspondence between simulation and measurement. The profile of JNO_2 is constant with altitude, whereas, e.g. JO^1D, shows a big increase up to one order of magnitude as shown in the box model comparison (Section 4.1, Figure 4.2). Thus, the values of JNO_2 do not show such a spread distribution as the other shown photolysis rates.

The same result holds for the investigation of the bandwidth of the KDEs for the nested domain. The difference in the bandwidth between simulation and measurement decreases only for JO^1D. The others stay nearly the same.

For both datasets, the global and the nested dataset, the median of the KDE for the photolysis rates of $JHNO_3$ and JN_2O_5 of simulations are smaller than for the measurement. This bias can be explained due to different assumptions on the incoming solar radiation which leads to linear shifts for all wavelength bands. As for the bandwidth investigation, one can see that the difference of the median between simulation and measurement for JNO_2 is much smaller than for the other three photolysis rates. This can be explained by the wavelength region of absorption. The photolysis rate JNO_2 is not as dependent on the overhead ozone column based on the larger absorption for wavelengths higher than $300\,\text{nm}$, as the other species. This leads to the assumption that for the measurement and for the simulation a different overhead column of ozone has been assumed. A comparison between the ozone profile during the measurement and the simulation can be found in section 4.2.5. The third factor influencing the median is the cross section used for calculating the photolysis rate. The assumption for the cross section dependence of the other three species than NO_2 on temperature has changed, seen by the changes in the underlying database for the cross sections for the different versions of Cloud. Like pointed out by the review of Orphal (2003), the changes of the NO_2 cross section on temperature changes are still under discussion. Nevertheless, the cross sections for NO_2 did not change over the last couple of years, in the different versions of CloudJ.

Figures 4.10 and 4.11 represent the histogram and the KDEs for flagged datasets of the global and nested domain. When flagging is applied, the shape of each KDE stays nearly the same. However, the lowest and highest values of the distribution seem to be cut off with respect to the unflagged dataset. The maximum peak is found at a higher value for the flagged dataset than for the unflagged. For example, the KDE of JN_2O_5 for the flagged dataset of the global domain showed a maximum at approximately $3 \times 10^{-5}\,\text{s}^{-1}$ with a counting of 3.5×10^5. The corresponding maximum of the KDE for the unflagged dataset shows a maximum counting of 3.2×10^5. This sharpening of the KDE is caused by neglecting the cloud influence. Since only clear sky datapoints are taken into account, the effect vanishes. The KDE and the median for JO^1D in both domains show a better agreement for the flagged dataset than for the unflagged dataset.

It can be concluded, that the photolysis rate of O^1D is much more affected by the impact of clouds than the other three shown photolysis rates.

Figure 4.10: Analysis of measured (black) and simulated (red) KDEs of (a): JNO_2, (b): JO^1D, (c): $JHNO_3$, (d): JN_2O_5, the red and black vertical line marks the calculated median based on the Gaussian kernel. Datapoints are taken from the global domain, flagging is applied.
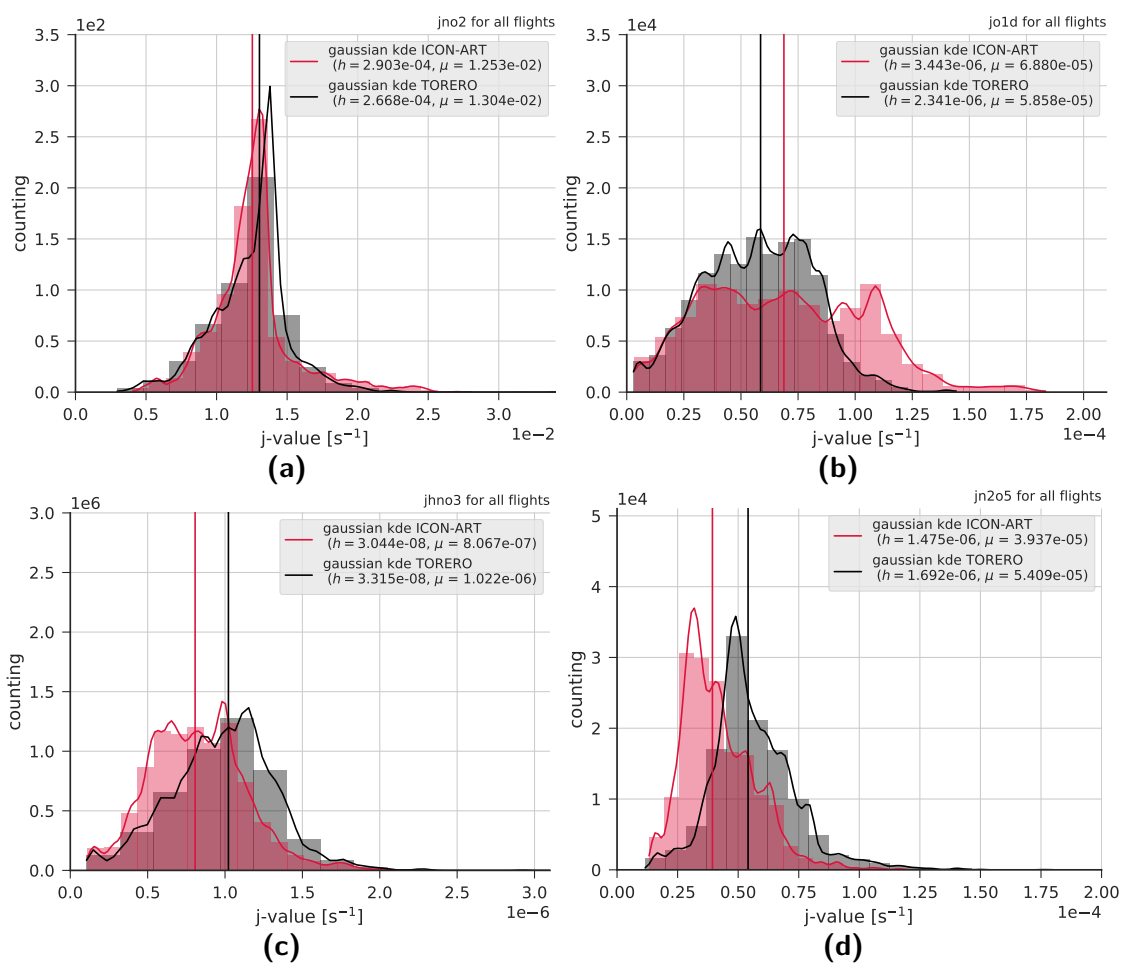
Figure 4.11: Analysis of measured (black) and simulated (red) KDEs of (a): JNO_2, (b): JO^1D, (c): $JHNO_3$, (d): JN_2O_5, the red and black vertical line marks the calculated median based on the Gaussian kernel. Datapoints are taken from the nested domain, flagging is applied.

For further analysis, the results of a linear regression model for the simulation and the measured dataset are used. For the simulation, as shown before, the datapoints are collected from the global and the nested domain. Simulation and measurement are separated in unflagged and flagged categories.

The linear regression model used in this analysis is defined by the equation:

$$y_i = a_1 x_i + b_1 + \epsilon \tag{4.5}$$

$$i = 1, \ldots, N \tag{4.6}$$

where x_i and y_i are the respective datapoints, for simulation and measurement, with length N. The variable a_1 is the slope and b_1 the intercept. By using the method of Ordinary Least-Squares Regression, the square sum of the residuals ϵ is minimised. This model assumes a linear dependency between both datasets, measurement and simulation. This assumption neglects drifts in the measurements, e.g. due to detector sensitivity or solar zenith angle dependence. Table 4.2 summarises the fitting results, as well as Pearson's r^2 as a measure of correlation and the Root Mean Square Error (RMSE). Here, all datapoints are taken into account, in comparison between nested (R2B7) and global domain (R2B6). The measure of r^2 is the highest for the photolysis rate of JO^1D, with approximately 0.85 in the global and 0.86 in the nested domain for the unflagged case. If only flagged datapoints are taken into account, r^2 increases. Thus, a linear correlation between simulation and measurement can be assumed. For the other photolysis rates, r^2 ranges between 0.5 to 0.8.

For a comparison, the study of Telford et al. (2013) uses the results of a predecessor of CloudJ, in the MetUM Chemistry Climate model (e.g. O'Connor et al., 2014). The results are compared to the INTEX-A campaign (July 2004 - August 2004). Here, the measure of r instead of r^2 has been used. For the simulation (not shown in Table 4.2), r is in the expected range between 0.7 and 0.9. The authors of the study in Telford et al. (2013) found a correlation for JNO_2 of $r \approx 0.65$ between measurement and simulation. In the case of the comparison between TORERO and ICON-ART simulation, ICON-ART shows a correlation of 0.7 in the global and nested domain. The correlation for JO^1D is higher (0.92 for ICON-ART and 0.83 for MetUM).

Since the correlation coefficient and r^2 for all investigated photolysis rates for both domains point to the allowed assumption of linearity between simulation and measurement, the analysis of the slope a_1 and the intercept b_1 allows for further interpretation of the model result.

The respective slope a_1 is slightly different between global and nested domain. For the unflagged dataset, the differences are within the boundaries of the estimated error. For the flagged dataset, the slope is higher for the nested domain than for the global domain.

The intercept represents a constant bias between measurement and simulation. This bias is slightly higher, outside of the boundaries of the estimated error of $\pm 0.001\,\text{s}^{-1}$, for the nested domain. With a higher resolution, the time the aeroplane is assigned to one model grid box, is decreased. Assuming an average speed of the aircraft of $250\,\text{m\,s}^{-1}$, the warplane is located in one grid box (R2B6) for $160\,\text{s}$. For the nested domain, the aircraft stays only $80\,\text{s}$ in one model grid box. This means, every $80\,\text{s}$, conditions are changing but the absolute number of datapoints stays the same. This leads to the assumption that with higher resolution, the possibility of misplaced cloud detection in comparison to the measurement is increased.

Table 4.2: Comparison of global vs nesting - L90 - unflagged. The values of the intercept and RMSE have the unit of s^{-1}.

jvalue	resolution	r^2	slope	intercept	RMSE
JNO2	R2B6	0.499	0.512 ± 0.001	$(6.090 \pm 0.001) \times 10^{-03}$	3.04×10^{-03}
	R2B7	0.510	0.513 ± 0.001	$(6.060 \pm 0.001) \times 10^{-03}$	3.05×10^{-03}
JO1D	R2B6	0.854	0.561 ± 0.001	$(1.837 \pm 0.001) \times 10^{-05}$	2.68×10^{-05}
	R2B7	0.858	0.559 ± 0.001	$(1.843 \pm 0.001) \times 10^{-05}$	2.70×10^{-05}
JHNO3	R2B6	0.691	0.763 ± 0.001	$(3.657 \pm 0.001) \times 10^{-07}$	2.36×10^{-07}
	R2B7	0.698	0.760 ± 0.001	$(3.660 \pm 0.001) \times 10^{-07}$	2.33×10^{-07}
JN2O5	R2B6	0.626	0.673 ± 0.001	$(2.811 \pm 0.001) \times 10^{-05}$	1.70×10^{-05}
	R2B7	0.635	0.675 ± 0.001	$(2.794 \pm 0.001) \times 10^{-05}$	1.68×10^{-05}

Table 4.3: Comparison of global vs nesting - L90 - flagged. The values of the intercept and RMSE have the unit of s^{-1}.

jvalue	resolution	r^2	slope	intercept	RMSE
JNO2	R2B6	0.432	0.572 ± 0.001	$(5.148 \pm 0.001) \times 10^{-03}$	2.48×10^{-03}
	R2B7	0.450	0.616 ± 0.001	$(4.708 \pm 0.001) \times 10^{-03}$	2.32×10^{-03}
JO1D	R2B6	0.835	0.606 ± 0.001	$(1.471 \pm 0.001) \times 10^{-05}$	2.15×10^{-05}
	R2B7	0.845	0.625 ± 0.001	$(1.396 \pm 0.001) \times 10^{-05}$	2.02×10^{-05}
JHNO3	R2B6	0.744	0.907 ± 0.001	$(2.228 \pm 0.001) \times 10^{-07}$	2.30×10^{-07}
	R2B7	0.762	0.951 ± 0.001	$(2.015 \pm 0.001) \times 10^{-07}$	2.31×10^{-07}
JN2O5	R2B6	0.609	0.856 ± 0.001	$(1.964 \pm 0.001) \times 10^{-05}$	1.75×10^{-05}
	R2B7	0.630	0.910 ± 0.001	$(0.796 \pm 0.001) \times 10^{-05}$	1.77×10^{-05}

Further on, the cloud free datapoints are taken into consideration (flagged). The result is summarised in Table 4.3. The correlation and r^2 is slightly decreased, except for JHNO$_3$ in both domains. The slope increased significantly and the intercept decreased. This leads to the conclusion that the misplaced clouds, meaning a cloud was detected in the simulation

but has not been seen during the measurement, or vice versa, result in a higher constant bias between measurement and simulation. This bias is higher due to a high resolved cloud coverage in the nested domain. The datapoints diagnosed to have a cloud coverage greater than zero have changed in the nested domain in comparison to the global domain. For the flagged datasets, the RMSE is slightly decreased, another indicator that the model of linear regression is suitable for the comparison between measurement and simulation of photolysis rates. The influence of clouds seems to have a nonlinear contribution to the distribution of datapoints. The deviation from the linear model decreased, as indicated by the RMSE, if cloudy datapoints are filtered out.

This analysis shows the advantage of ICON-ART to simulate two domains with different resolutions, interacting with each other during one simulation. The correlation between measurement and simulation is much higher in the nested domain for cloud free and cloudy categories. Despite the higher bias in the nested domain, it seems reasonable to limit the further analysis to the nested domain with a higher horizontal resolution. This domain allows for more information about the influence of clouds than the global domain. In the global domain, the horizontal resolution is 2.5 times coarser than in the nested domain, thus specific types of cloud coverage cannot be resolved as good as in the nested domain.

4.2.4 Solar zenith angle dependency of photolysis rates

One of the main dependencies of photolysis rates on variables, is the dependency on the solar zenith angle (SZA). In order to investigate differences, which would limit the further investigation, both datasets, simulation and measurement, are investigated with respect to the SZA of the simulation. The SZA in simulation and measurement are matching (not shown), thus there is no difference in taking one or the other dataset for this investigation. Figure 4.12 shows the binned results of both datasets. The datapoints for the simulation are taken from the nested domain. For every flight, the datapoints are binned based on the SZA values between 0° and 90°. The solid lines, red for the simulation and black for the measurement, represent the median of the binned distribution. The shaded areas represent the standard deviation. The round bracket indicates the open beginning of the interval, the square bracket the closed end of the interval.

During the campaign, only SZAs smaller than 80° occurred. The photolysis rates JNO_2, $JHNO_3$ and JN_2O_5 show the same SZA dependence within the limits of the error estimation. The photolysis rate of JO^1D shows this agreement only for SZA $> 25°$ in the boundaries of the estimated error. For smaller SZAs, the simulated photolysis rates are increased by approximately 30 %. This disagreement between measurement and simulation can be caused by errors in the actinic flux measurement in the wavelength regions. Within CloudJ, a pre-calculated and wavelength binned incoming solar irradiation is used. The incoming irradiation is based on values for the year of 1995. The incoming solar radiation varies over the solar cycle. Thus, the incoming solar radiation could cause a systematic error. It should also be taken into account that the overhead sun was present in the middle of each flight episode. On most days, the campaign started at 12 UTC. For most flights, the aeroplane was located at high altitudes during the middle of the flight episode. Thus, scattering of high altitude clouds, with a high ice water path could cause the difference between measurement and simulation. Assuming clear sky conditions for the measurement and a cloud present in simulation, scattering effects enhancing the actinic flux at smaller wavelength regions are causing differences in photolysis rates. The other photolysis rates are less affected since the corresponding chemical species show a different spectrum of the absorption cross sections as seen in Figure 4.4.

In order to underline the argument that clouds cause an enhancement of photolysis rates, the SZA dependence for clear sky conditions for the simulation is shown in Figure 4.13. Photolysis rates of JO^1D become smaller for small SZA values. All four photolysis rates decrease in the clear sky simulation for all values of SZA. Since only clear sky datapoints are taken into account, also for the measurement, differences between measurement and simulation get smaller for all shown photolysis rates. Nevertheless, for JO^1D, the difference for small SZAs is still higher than for the other three shown photolysis rates.
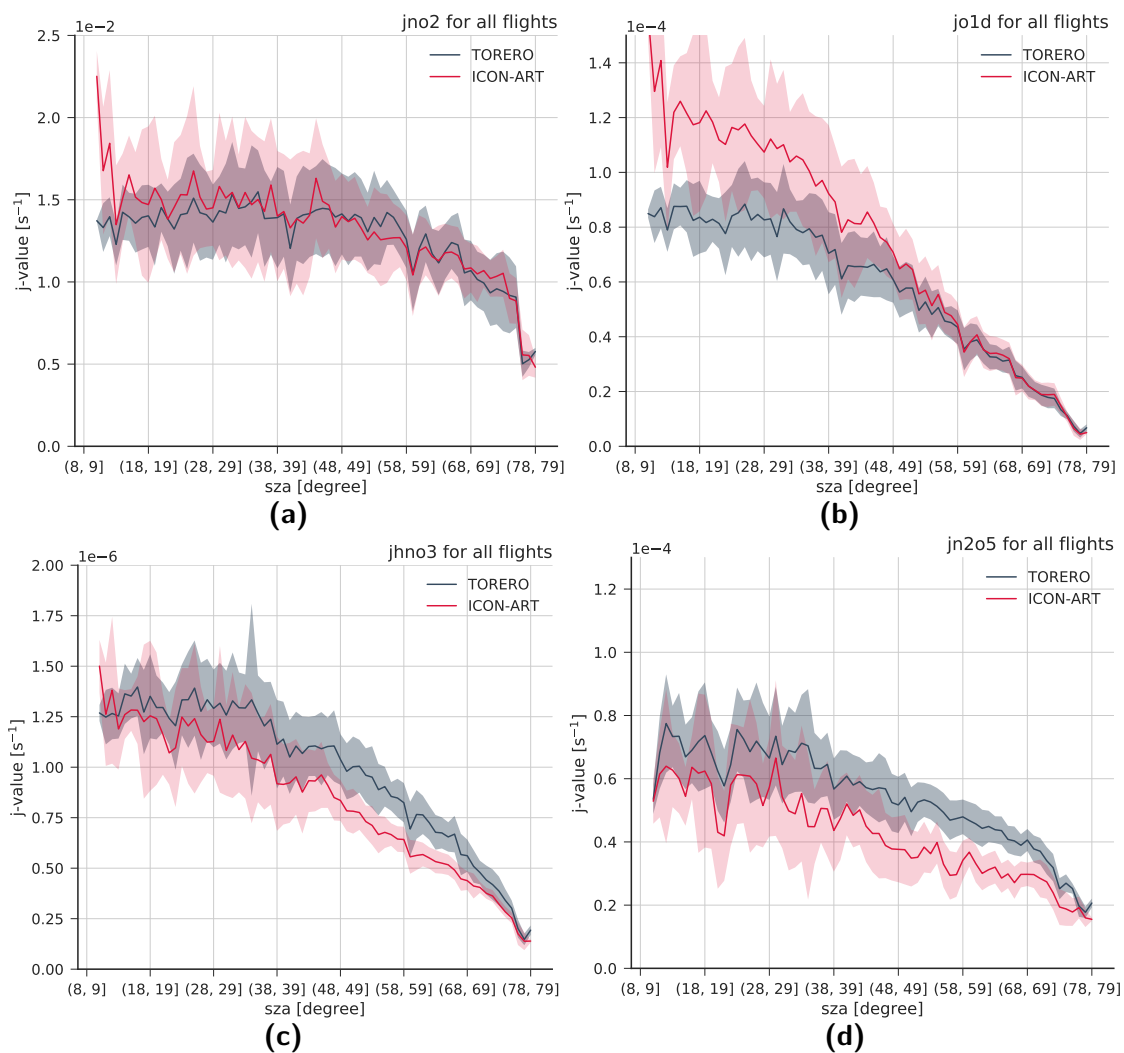
Figure 4.12: Measured (black) and simulated (red) photolysis rates as a function of the solar zenith angle (SZA) for (a): JNO_2, (b): JO^1D, (c): $JHNO_3$, (d): JN_2O_5. Datapoints are taken from the nested domain, no flagging applied.

Another influencing factor could be that the overhead ozone column differs for measurement and simulation. The influence of the overhead ozone column on the photolysis rates is investigated in the following section.
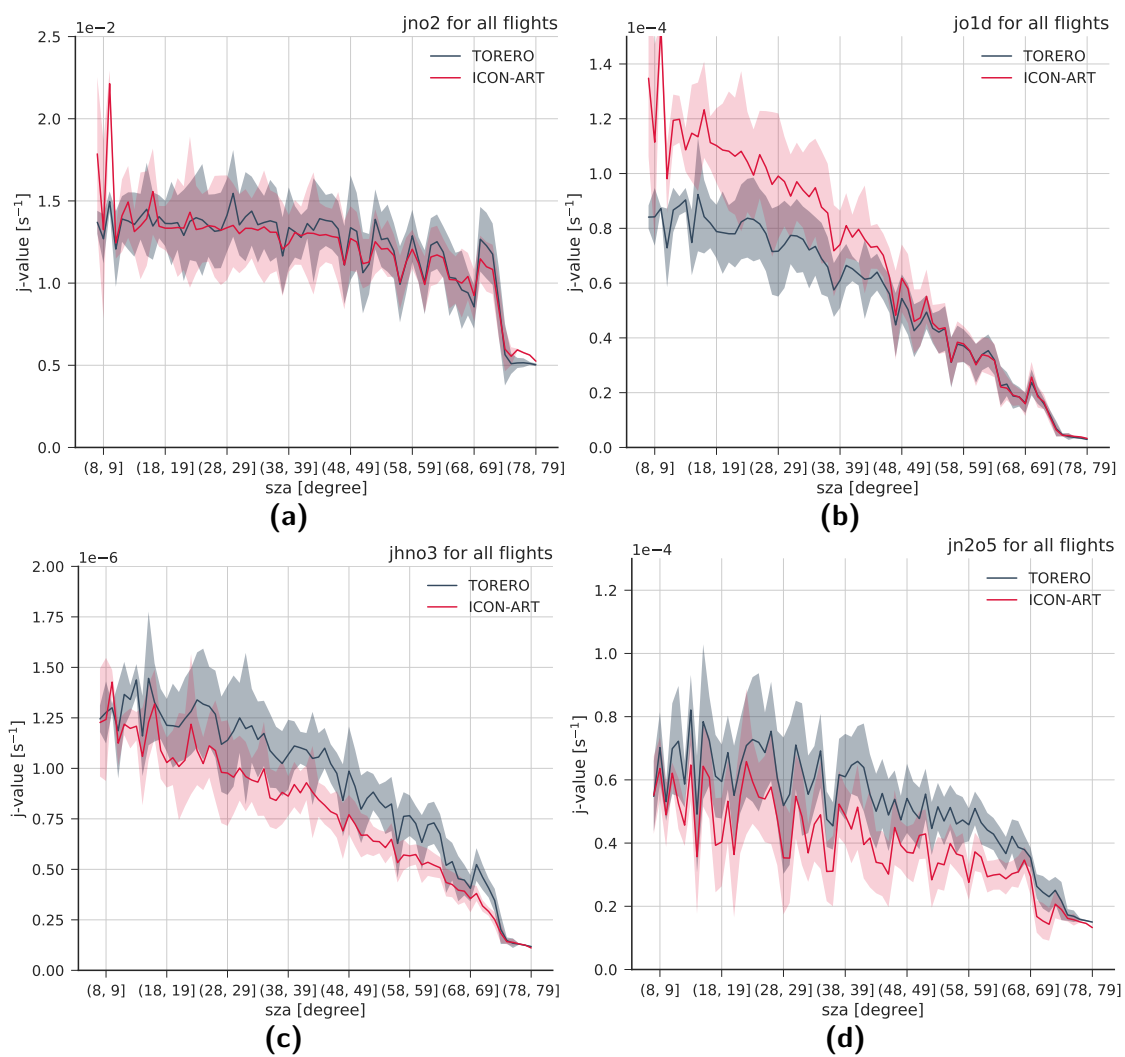
Figure 4.13: Measured (black) and simulated (red) photolysis rates as a function of the solar zenith angle (SZA) for (a): JNO_2, (b): JO^1D, (c): $JHNO_3$, (d): JN_2O_5. The result is shown for the clear sky simulation. Datapoints are taken from the nested domain, flagging is applied.

4.2.5 Differences between simulated and measured ozone values during the TORERO campaign

Differences in the photolysis rates seen in the section before can be caused by altered ozone distributions used for the actinic flux calculation. No information about the used overhead ozone column for the TUV calculations are available. However, the actual amount of ozone given as the mass mixing ratio can be retrieved from the measurement dataset. Ozone mass mixing ratios were measured by a dual beam spectrophotometer. The median vertical profile, binned for the altitude range from 1030 hPa to 150 hPa for the simulation and the measurement is shown in Figure 4.14. Both median profiles agree in the limits of
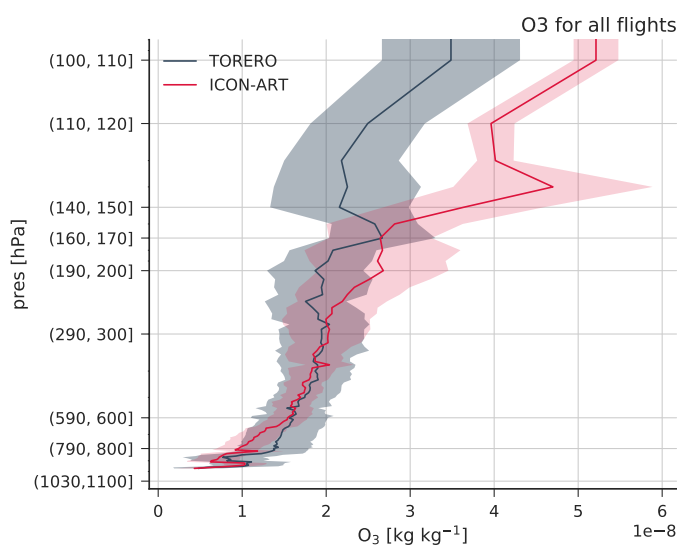
Figure 4.14: Measured (black) and simulated (red) ozone mass mixing ratio. The solid lines represent the median, the shaded area the standard deviation.

the estimated error, based on the standard deviation for each bin for pressure levels up to 140 hPa. Differences near the ground, between 1030 hPa and 850 hPa are the smallest. Above 140 hPa, the median of the ICON-ART simulation is higher than the measured ozone value. The difference is about $2.4 \times 10^{-8} \, \text{kg kg}^{-1}$. This is equivalent to a relative difference of approximately 30 %. In order to investigate the influence of a change of the ozone mixing ratio in the same order of magnitude on the four selected photolysis rates, a box model simulation is performed. Figure 4.15 shows the photolysis rate profile of JNO_2, JO^1D, $JHNO_3$ and JN_2O_5. For the simulation, CloudJ was operated in a box model configuration, using the atmospheric variables based on the US Standard Atmosphere NOAA (1976). The setup is comparable to the simulations of section 4.1. The ozone mass mixing ratio was varied by ± 30 %, for a chosen SZA of 30°. A clear sky atmosphere was assumed. The highest variations due to the varied ozone mixing ratio can be seen for the photolysis rate of JO^1D. The photolysis rate profile of JNO_2 shows the smallest alteration, changes in the profiles of $JHNO_3$ and JN_2O_5 are comparable. This result fits to the assumption of
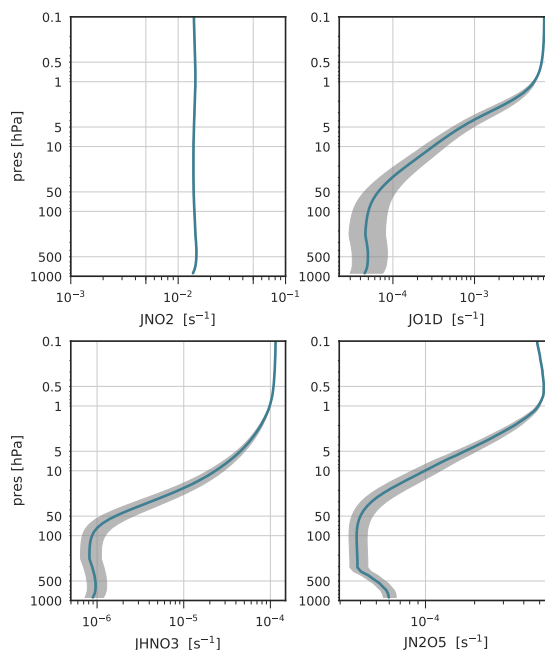
Figure 4.15: Box model simulation of photolysis rates with a variation of the ozone volume mixing ratio of $\pm 30\,\%$, for SZA $= 30°$. The variation of photolysis rate is indicated by the shaded area.

the previous section that differences between measurement and simulation for JO^1D are mainly caused by the differences in the ozone mixing ratio. The variations of JO^1D are approximately $\pm 0.5 \times 10^{-4}\,\mathrm{s}^{-1}$. This value fits to the maximum deviation, found in section 4.2.4.

4.2.6 Vertical profiles of photolysis rates

In order to focus on the impact of clouds on photolysis rates, the analysis is now shifted towards the investigation of vertical profiles. In the presence of a cloud, it is expected to see a decrease of the respective photolysis rate below the cloud and an enhancement above. This generalised behaviour is accepted in principal, but a quantification has only been performed in a few studies (Liu et al., 2006, 2009; Prather, 2015).

The datasets, analysed in the sections before, flagged and unflagged, are binned to predefined pressure bins. Starting at 1030 hPa decreasing in steps of 10 hPa down to 150 hPa. In both figures, Figure 4.16 and 4.17, the median of each bin is plotted. The shaded area represents the standard deviation from the median.

Beginning with the analysis of the unflagged case, as seen in Figure 4.16, the profiles of photolysis rates of JO^1D and JNO_2 are higher for ICON-ART than for the measurement and the profiles of $JHNO_3$ and JN_2O_5 are smaller for the simulation than for the measurement. However, all profiles agree in the limits of the error estimation. The largest difference can be noted for the comparison of the JO^1D profile. This enhancement corresponds to the
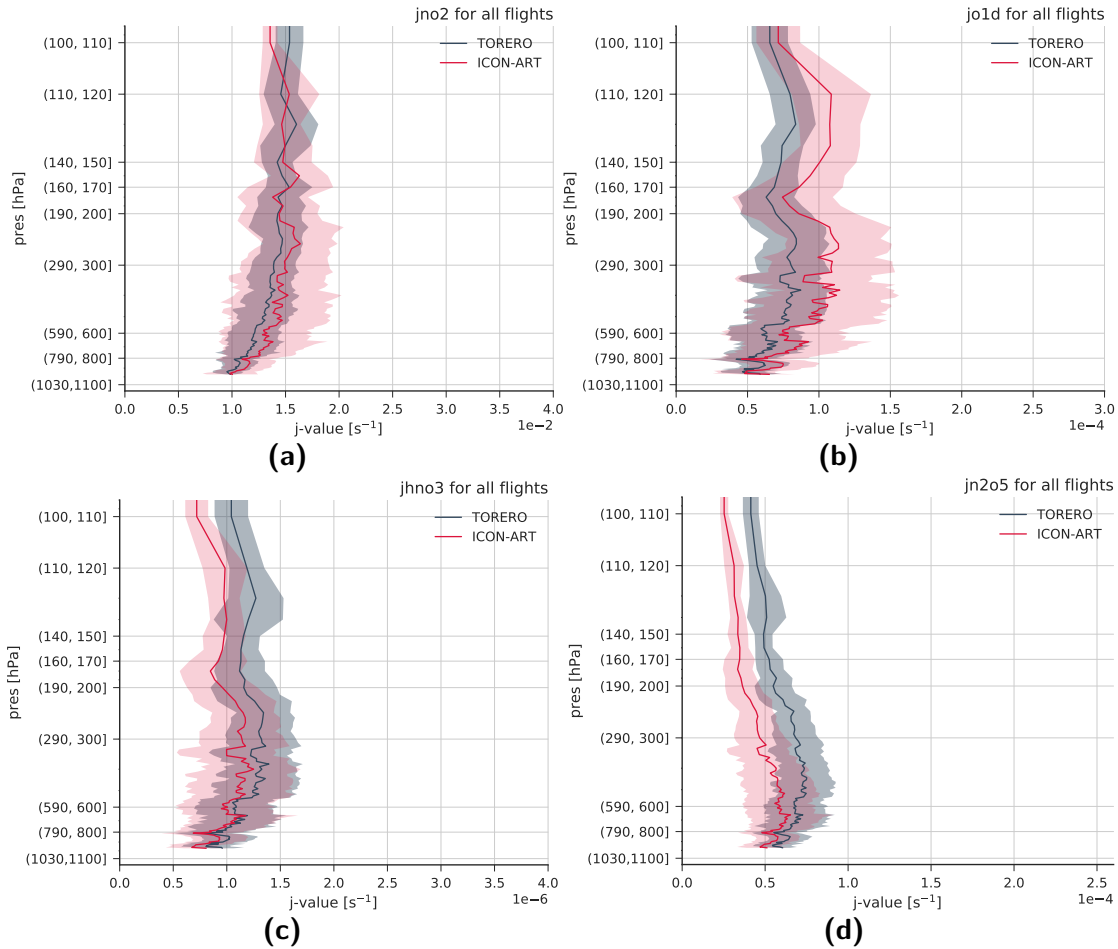
Figure 4.16: Vertical profiles of measured (black) and simulated (red) for (a): JNO_2, (b): JO^1D, (c): $JHNO_3$, (d): JN_2O_5, the red and black lines mark the calculated median for vertical binning. The shaded area represents the standard deviation from the median. Datapoints are taken from the nested domain, flagging is not applied.

previous findings and is mostly due to systematic differences in the actinic flux and due to the impact of clouds. For all four photolysis rates, the difference between measurement and simulation is increasing with increasing altitude. In Figure 4.17, only flagged datapoints of the nested domain are taken for the vertical profile construction. The difference between measurement and simulation is decreasing, as well as the error for each of the profiles. Only the profile of JN_2O_5 shows a deviation of the simulation from the measurement, outside of the limits of the standard error, above 300 hPa. This might be caused by the temperature dependency of the cross section of N_2O_5. Measurements of the N_2O_5 cross section, lead to a very weak temperature dependence between 195 K and 300 K. Thus, most models neglect this dependence completely. For ICON-ART, a temperature dependent representation of the cross section is implemented, but there is no knowledge about the dependence used for TORERO.
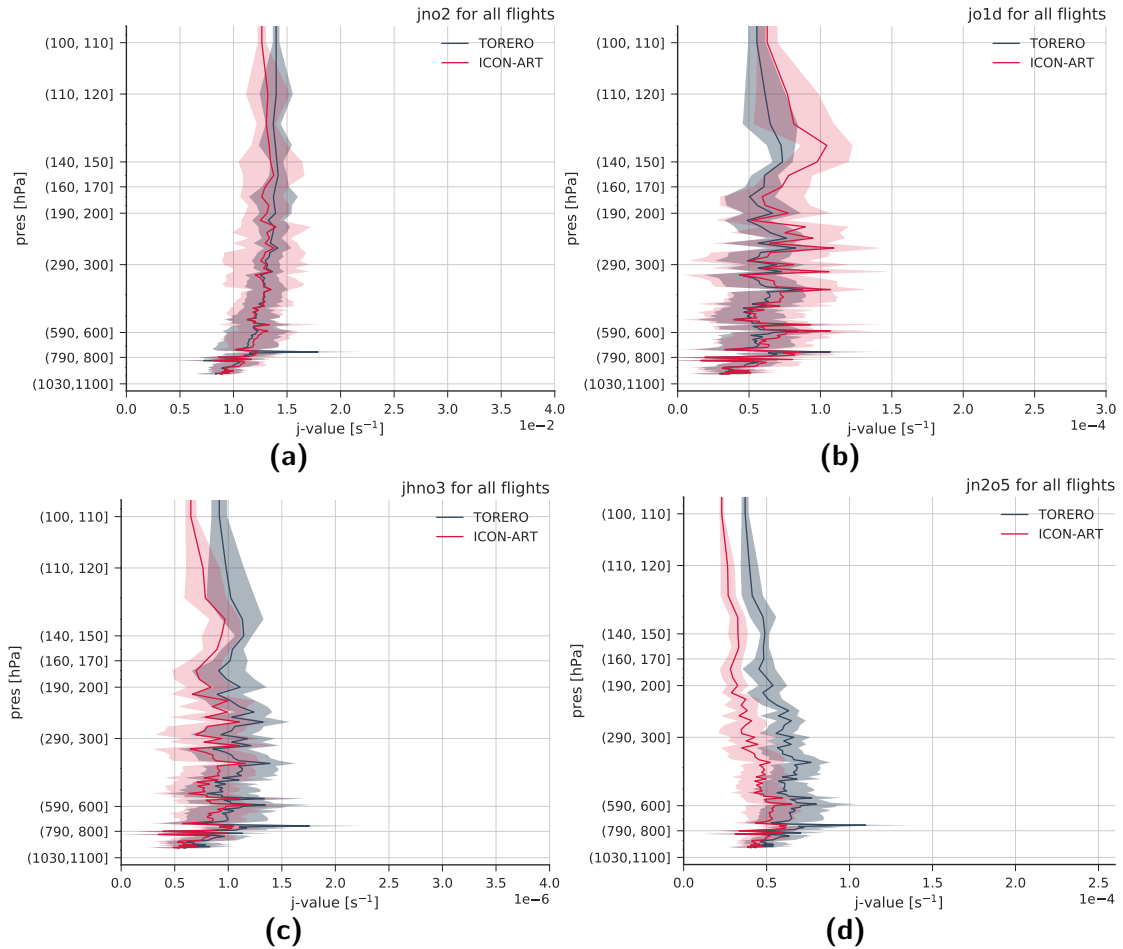
Figure 4.17: Measured (black) and simulated (red) vertical profiles of (a): JNO_2, (b): JO^1D, (c): $JHNO_3$, (d): JN_2O_5, the red and black lines mark the calculated median for vertical binning. The shaded area represents the standard deviation from the median. Datapoints are taken from the nested domain, flagging is applied.

All profiles seem to have a constant difference and influences seem to be represented in a consistent way. The profile of $JHNO_3$ shows two dips between $170\,\text{hPa}$ to $110\,\text{hPa}$. The relative differences are in the range between $10\,\%$ to $14\,\%$. By investigating the liquid and ice water path (diagnostic ICON-ART variables of *tqc* and *tqi*), the maximum of the ice water path can be found in the same altitude region, between $170\,\text{hPa}$ and $110\,\text{hPa}$. In this region, the median of the binned value of can be determined to $\text{tqc} = 3.2 \times 10^{-5}\,\text{kg m}^{-2}$. Since the dip in the photolysis rate profile vanishes for all photolysis rates, in the flagged dataset (Figure 4.17), it can be stated that the relative reduction between $10\,\%$ to $14\,\%$ for all photolysis rates is caused by scattering processes on ice water particles or large cloud droplets.

From the investigation of vertical profiles of the four photolysis rates it can be concluded that with ICON-ART the vertical profile are represented in a sensible way. The differences to the measured profiles is within the boundaries of the error estimation, except for JN_2O_5. This

71

difference can be caused by different representations of the temperature dependence of the absorption cross section of JN_2O_5 between ICON-ART and TORERO. By comparing flagged and unflagged profiles, the differences get smaller between simulation and measurement, for the flagged category. As a comprehensive validation, this study captures the reasonable simulation of photolysis rate profiles with ICON-ART in the presence of clouds.

4.3 Enhancement and reduction of photolysis rates due to the presence of clouds

Only a few studies have been made in the past on quantifying the impact of clouds on photolysis rates. Studies by e.g. Tie et al. (2003); Liu et al. (2006) report changes of JO^1D ranging from 5% to 13%, as a global average. Selected datapoints in this study showed photolysis rate enhancement of up to 62%. With ICON-ART, the cloud impact can be quantified using photolysis rate simulations in a nested model simulation. First, a case study is presented for a selected flight of the TORERO campaign.

4.3.1 Investigation of a selected case study

For the case study, the flight RF03 on 24 January 2012 is selected. During this flight, the aeroplane was flying firstly above a cloud, then descending through the cloud, flying below that cloud and ascending again. This flight path, with the cloud present in the model, is shown in Figure 4.18, respectively. The grey line shows the plane altitude in hPa. In the same panel, the blue lines represents the diagnosed top of the cloud and bottom of the cloud present during the model simulation. In addition, the orange line shows the empirical cloud flag.
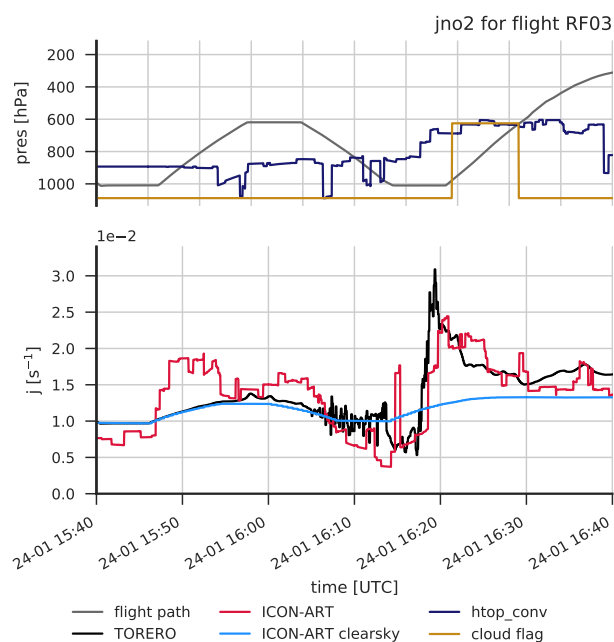
Figure 4.18: Timeseries of measured (solid black) and simulated photolysis rates for JNO_2. The upper panel shows the flight altitude in hPa of the aircraft, on the y-axis and the time is given in UTC on the x-axis. Additionally, the manually constructed cloud flag (orange), and the diagnostic cloud top height is shown (dark blue). The photolysis rates are given in units of $1 \times 10^{-2}\,\mathrm{s^{-1}}$. The solid red line represents the timeseries for the cloudy-sky simulation, the light blue line the clear-sky simulation.

Additionally, the lower panel shows the timeseries of the measured (black), cloudy case (red) and clear sky case (light blue) photolysis rate of JNO_2 as an example.

Figure 4.19 shows the vertically binned analysis, with similar colour coding as in the timerseries. This analysis is performed for all four photolysis rates. The grey vertical line in each box represents the median. Edges of each box show the first and third quantile with additional maximum and minimum markers at the end of the vertical line.

Between 15:55 UTC and 16:05 UTC, the ICON-ART diagnosed cloud product of htop detects a cloud presence. However, this cloud flag shows a misplaced cloud. By comparison between the clear sky time series (blue) and the measured one, the match between both is obvious. This is another indicator for a clear sky case. A few minutes later, the deviation between clear sky simulation and measurement increases. Now, the cloudy case fits better to the measurement. The investigation of photographs, taken during the flight, shows a match between the simulated cloud position, relative to the aeroplane and the realistic position for the time span between 16:10 UTC and 16:30 UTC.

Even though this selection of a case study is a representative for a misplaced cloud, it is a reasonable choice for the comparison between clear sky and cloudy simulation within ICON-ART. The comparison between the two timeseries shows a reasonable response in the presence of the cloud along the flight path.

Most datapoints would be declared as *below cloud* for flight altitudes below 900 hPa, as seen in the timeseries between 16:10 UTC and 16:15 UTC. For all four photolysis rates shown, a decreased value for measurement and simulation with respect to the clear sky simulation is seen. The vertical box plot shows that the median for all four photolysis rates between 1000 hPa to 900 hPa is smaller for the cloudy simulation than for the clear sky simulation. The median for $JHNO_3$ and JN_2O_5 of the measurement is higher with respect to the clear sky simulation. This is probability due to the fact, that the difference is in the range of the overall bias, calculated in the investigations before. This bias can also be seen in Figure 4.9. Another indicator for the systematic bias can be derived from the SZA dependence investigation in section 4.2.4 in Figure 4.12. During this flight episode, the SZA is ranging between 29° to 37°. Within this range of SZA values, the bias of the dataset including all datapoints is comparable to the difference between the selected clear sky datapoints and the measurement for RF03.

The median within the bins between 800 hPa and 200 hPa for the cloudy simulation is higher than for the clear sky simulation for all four photolysis rates. The positive difference decreases with increasing altitude.

To summarise the findings of this case study, Figure 4.20a shows the relative difference between clear sky and cloudy simulation. The different colours represent the four different photolysis rates, the vertical line the error of the difference calculation. For this calculation, the median of the cloudy simulation is subtracted from the clear sky simulation median

and is also divided by this median. The value is given in percent. All four photolysis rates show a reduction below $10\,\%$. The enhancement for the selected altitude bins is smaller for the photolysis rate of JO^1D than for the other three photolysis rates. Between $500\,hPa$ to $300\,hPa$ the enhancement above clouds of JO^1D is about $40 \pm 10\,\%$ and between $300\,hPa$ to $200\,hPa$ about $25 \pm 5\,\%$.
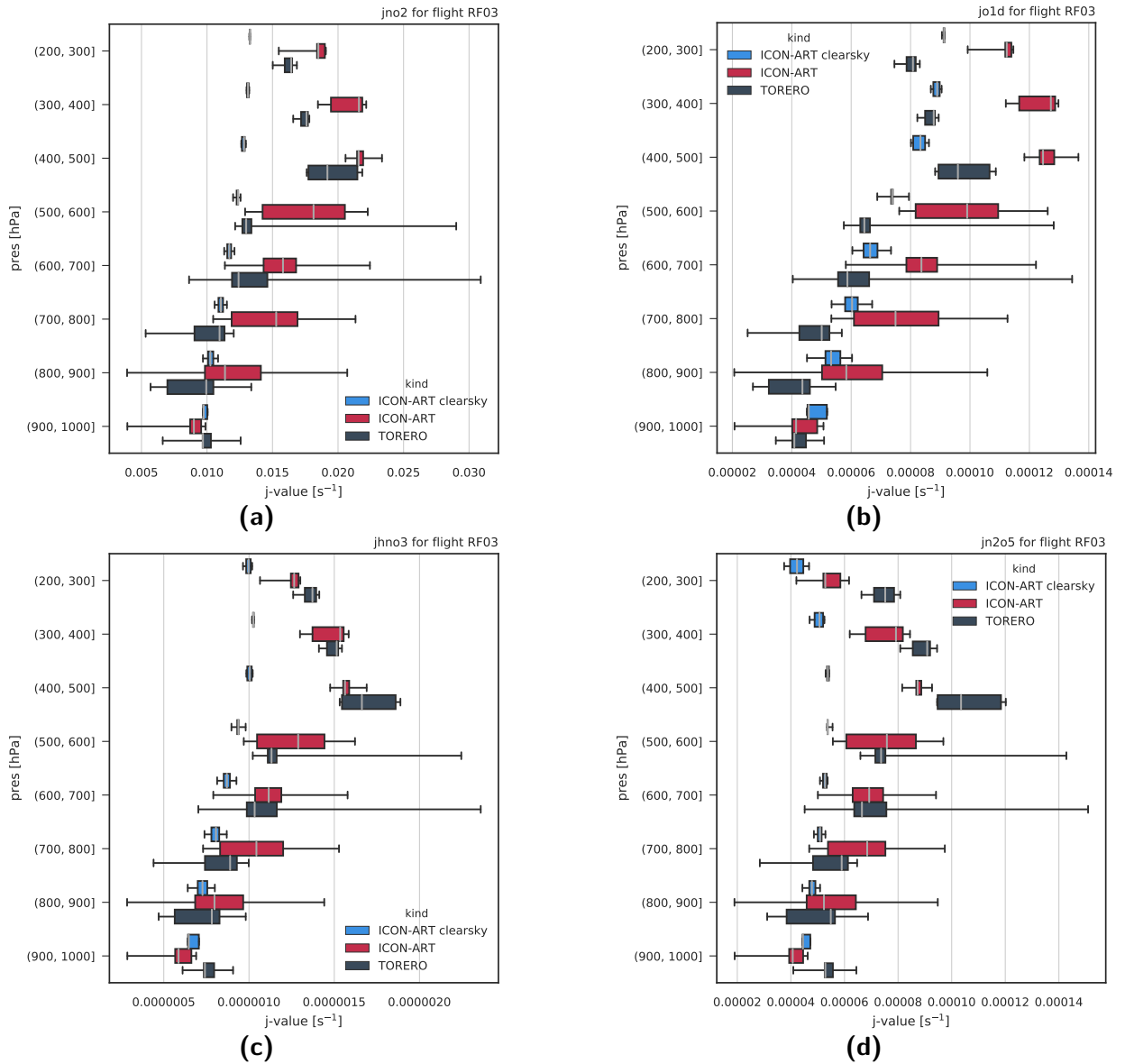

Figure 4.19: Analysis of a case study for RF03 with a flight path through a cloud - for measured (black) and simulated (red) vertical profiles of (a): JNO_2, (b): JO^1D, (c): $JHNO_3$, (d): JN_2O_5, the red and black line marks the calculated median for vertical binning. Datapoints are taken from the nested domain, flagging is not applied.
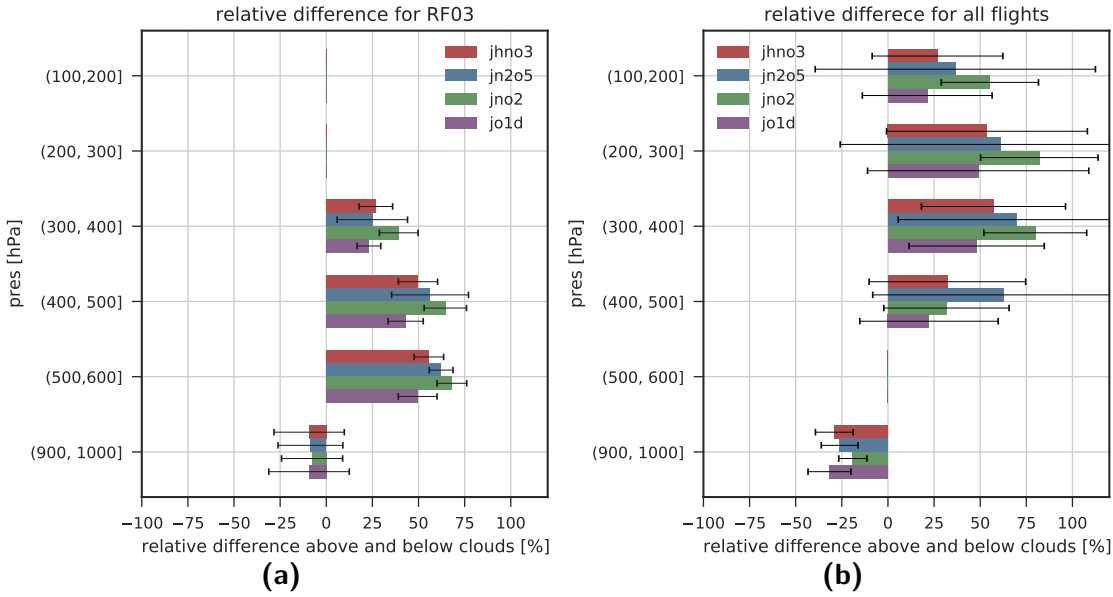
Figure 4.20: Mean relative differences for above and below cloud cases for the photolysis rates JNO$_2$, JO^{1}D, JHNO$_3$ and JN$_2$O$_5$. Vertical black lines represent the estimated error. Differences are taken for a) only RF03 and b) for all flights. Datapoints are taken from the nested domain. The bin $(900, 1000]$ represents the below cloud category, all others the above cloud category.

4.3.2 Co-located analysis of the simulation

The selected case study of flight RF03 showed that ICON-ART is able to represent enhancement and reduction of photolysis rates in different wavelength regions in a reasonable manner. The following analysis is focused only on ICON-ART simulations.

The datapoints of the cloudy case category are split into *below* and *above* categories. For the construction of this category, the diagnostic output of the simulation of the cloud top (htop_conv) and cloud bottom (hbas_conv) is used. As a reference, the flight altitude, on which the simulation is interpolated on, is taken into account. All datapoints, where the air plane was flying below the diagnosed height of hbas_conv with an additional threshold of 500 m, are in the *below* cloud category. When the plane was located above the cloud top, diagnosed by hbas_top, the datapoints are accounted for the *above* cloud category. The relative differences for all flights are summarised in Figure 4.20b. Compared to the investigation of RF03, here the datapoints for the pressure bin 500 hPa to 600 hPa are not taken into account. For RF03, only above cloud category points are added to this bin. When all flights are combined, sometimes the plane was located in the middle of a cloud, below one or above. This leads to a result which represents a mixture of reduction and enhancement effect. A concrete categorisation into above and below cloud case is not possible, thus this bin is excluded from the analysis. Compared to the analysis of RF03, the altitude ranges 100 hPa to 200 hPa and 200 hPa to 300 hPa is added. For RF03, these bins are excluded, because the plane was located at pressure levels higher than 300 hPa for

the investigated time span. For the other altitude ranges, the reduction below clouds is the highest for JO^1D with a relative difference of approximately $-30 \pm 10\,\%$. This reduction is more than twice as high as for the case study of RF03. The higher reduction is caused by the larger range of SZA values for the datapoints under consideration. The SZA ranges from 29° to 37° for RF03. For all datapoints in the *below* category, the SZA is between 17° to 77°. For a higher value of SZA, the optical path through the atmosphere is enhanced and thus the reduction effect due to the presence of clouds is also increased. Additionally, during the selected case of RF03, only cloud water particles are detected. For the *below* category, also ice water particles are detected. The sum of both is also higher for the full dataset in comparison to the selected case. In comparison to the case study, both variables contribute to the higher reduction for the complete dataset.

For the above category, the photolysis rate of JNO_2 shows the greatest enhancement of all four photolysis rates, in all pressure bins. The greatest enhancement is found for the bin between $200\,hPa$ to $400\,hPa$ for JNO_2, of $86 \pm 14\,\%$. Between $400\,hPa$ to $500\,hPa$ the relative difference for JO^1D is the smallest with a value of $21 \pm 24\,\%$. The estimated variation is very high for both pressure bins between $100\,hPa$ to $300\,hPa$. Since the relative difference is always positive, the high error is an indicator for a widely spread distribution. For the altitude bin between $300\,hPa$ to $400\,hPa$, the estimated error is slightly smaller. Investigating the timeseries of all flights, it can be concluded that the aeroplane was located for most of the time at altitudes between $100\,hPa$ to $200\,hPa$, thus more datapoints fall into this bin than in the others. In this bin, more than 6000 datapoints are counted. In contrast to that, between $300\,hPa$ to $400\,hPa$, only 100 datapoints are counted. This means that for the bin between $100\,hPa$ to $200\,hPa$, it is much more likely to have a wide spread of the relative enhancement than for the bin $300\,hPa$ to $400\,hPa$. The value of the ice water path is decreasing with increasing altitude. For $300\,hPa$ to $400\,hPa$, the median value of the ice water path is of about $300\,g\,m^{-2}$, whereas for $100\,hPa$ to $200\,hPa$ the median is found at $150\,g\,m^{-2}$. The SZA for the datapoints in the above category ranges between 7° to 41°. The value of the SZA is more important for the reduction below clouds due to the air mass dependency. This is also seen by the comparison between the case study and the complete dataset. The relative differences for all four photolysis rates are comparable.

4.3.3 Non co-located analysis of the simulation and measurement

Finally, the enhancement and reduction effects for the measured photolysis rates are estimated. In case of the measurement, no clear sky surrogate like for the simulation is possible. Thus, the constraint on the specific flight path and cloud top or bottom height has to be less strict than in the section before. First, the dataset is divided by the cloudy and clear sky datapoints. For the clear sky points, all flagged datapoints are taken, for the cloudy sky category the residual datapoints are accounted. This is done for both datasets,

the cloudy simulation and the measurement. Both resulting data categories are binned on the respective pressure bins, like shown before. Based on the results of the previous section, the pressure bin from $900\,\mathrm{hPa}$ to $1000\,\mathrm{hPa}$ is the representative for a below cloud case. Pressure bins from $500\,\mathrm{hPa}$ to $100\,\mathrm{hPa}$ represent the above cloud altitude range. The relative difference between the clear sky and cloudy sky category is depicted in Figure 4.21, for the simulation and the measurement. First thing to be kept in mind for the
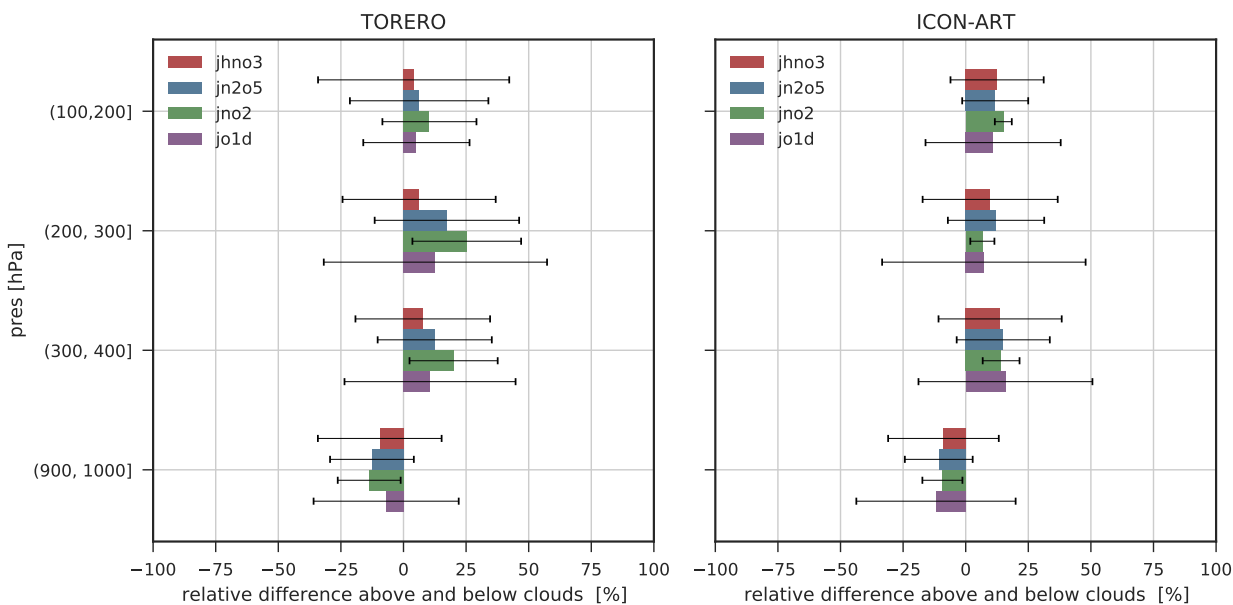
Figure 4.21: Mean relative differences for above and below cloud cases for the photolysis rates JNO_2, JO^1D, $JHNO_3$ and JN_2O_5. Vertical black lines represent the estimated error. Differences are taken for a) TORERO and b) ICON-ART. Datapoints are taken from the nested domain

comparison is the point that clear sky and cloudy datapoints no longer correspond to the same SZA, overhead ozone column or temperature conditions. Thus, the maximum value of enhancement and reduction is expected to be decreased, since other effects are interfering. This can be seen for both, the simulation and measurement in Figure 4.21. For TORERO, the maximum reduction below clouds is approximately $15\,\%$ and the enhancement above $25\,\%$. Only the maximum enhancement for ICON-ART is a little less (of about $20\,\%$). The reduction below clouds is comparable. The variations, indicated by the vertical lines, are comparable for simulation and measurement.

In the previous section, the photolysis rate of JO^1D showed the highest reduction below clouds of all four photolysis rates. This relationship can be seen in this study as well. In both studies, JNO_2 shows the weakest reduction effect. Between TORERO and ICON-ART the reduction of JN_2O_5 and $JHNO_3$ is comparable. In contrast to the simulation, TORERO shows the highest reduction for JNO_2 instead of JO^1D. This could be caused by differences in the wavelength bin characterisation between simulation and measurement. Since is was shown that the measured overhead ozone column shows a large difference to the ICON-ART simulation, the change of the difference hierarchy between JNO_2 and JO^1D cloud be caused

by that. As seen in section 4.2.5 difference in the overhead ozone column have the largest impact on JO^1D and the weakest on JNO_2 between $1000\,hPa$ to $100\,hPa$.

The enhancement above clouds is the highest for JNO_2 between $300\,hPa$ to $400\,hPa$ in the measurement. The highest enhancement in the simulation occurs also in this bin but not for JNO_2. The photolysis rate of JO^1D shows the highest enhancement of about $20\,\%$ in this region. As for the below cloud case, the differences in the overhead ozone column could cause this discrepancy. JNO_2 shows the highest value and JO^1D the smallest for the bin $100\,hPa$ to $200\,hPa$. This altitude region has also shown the smallest effect on changes in the overhead ozone column. Here, the discrepancy between measurement and simulation occurs for $JHNO_3$ and JN_2O_5. As throughout the analysis in this section, here again the influence of the overhead ozone column could be a possible explanation. Where $JHNO_3$ shows an approximately constant variation, JN_2O_5 shows an increasing variation with increasing altitude (see Figure 4.15).

The overall conclusion of this study is that ICON-ART shows a reasonable simulation of reduction and enhancement effects of photolysis rates due to clouds compared to the measurement. For all four photolysis rates the relative difference is between $20\,\%$ to $30\,\%$. Discrepancies between simulation and measurement can find a consistent explanation in the difference of the overheat ozone column.

4.4 Conclusions

Model studies investigating the cloud impact on photolysis rates are rare. As stated by van Weele and Duynkerke (1993), it is relatively easy to include a single cloud layer in a radiative model but overlapping cloud fields are more complicated. Thus, besides intensive modelling studies, additional measurements are of high importance as well (e.g. Vilà-Guerau de Arellano et al., 1994). The studies by Tie et al. (2003) and Liu et al. (2006) show an overall enhancement of JO^1D and JNO_2 of $13\,\%$ to $20\,\%$ and a reduction of about $13\,\%$ for JNO_2 and slightly smaller for JO^1D. The study of Liu et al. (2006) even reports enhancements of JO^1D and JNO_2 up to $62\,\%$. Both model studies in Tie et al. (2003) and Liu et al. (2006) use global datasets for the comparison. For the investigation of the TORERO campaign, a limited area was selected. By taking the relatively high error estimations into account, it can be concluded that the quantification of the enhancement and reduction due to clouds of the investigated photolysis rates is in agreement with previous studies. The first study on the quantification, including all flights results in an enhancement up to $80\,\%$ for JNO_2, due to the presence of clouds. This enhancement is based on the calculation, where a clear sky ICON-ART simulation was compared to a cloudy-sky simulation. Every datapoint contributing to the mean relative difference is influenced by the same SZA, overhead ozone column and temperature. The second study neglects this temporal co-location. With that,

a comparison also for the measure photolysis rates becomes possible. In this case, the enhancement due to the presence of clouds is decreased, investigating the measurement and the simulation. Here, a maximum relative difference for the measurement of 25 % for JNO_2 is reached. The simulations shows a slightly smaller enhancement. The overall result is that in the presence of clouds, a relative difference of 20 % to 30 % is expected. For an . Studies of Tie et al. (2003) and Liu et al. (2006) used fully coupled chemistry simulations. This has also to be taken into account, explaining the discrepancies between both analyses (between measurement and simulation) and to the cited values of photolysis rate enhancement. If the photolysis rate of JO^1D is enhanced, the ozone concentration decreases and thus the actinic flux in the respective wavelength regions increases as well. For the ICON-ART simulation, a climatological value for the overhead ozone column has been taken into account (Hollingsworth et al., 2008). With that, clear sky and all sky simulation are only different by the impact of clouds. For both studies by Tie et al. (2003) and Liu et al. (2006), the actinic flux is altered by altering chemical composition. The result of the co-located ICON-ART analysis and the non co-located comparison of the measurement and ICON-ART, reflects a similar result as indicated by Liu et al. (2006). Here, the authors state an absolute enhancement of photolysis rates of 13 % in global average. The global average corresponds to the second study, the non co-located analysis. In Liu et al. (2006), also a maximum enhancement of 62 % is reported, for selected datapoints. This result corresponds to the co-located analysis of ICON-ART. This emphasises the importance of the photolysis rate validation on both aspects. First, the validation for co-located datapoints and an average over the specific area.

Nevertheless, the wide range of values of the relative difference shows the great importance of this study. The simulation of photolysis rates with ICON-ART is proven to be reasonable for the wavelength region which is important for the UTLS region. The SZA dependence shows a bias between measurement and simulation for JO^1D for SZAs smaller than 20°. The introduction of data categories, flagged and unflagged by the presence of clouds, either in simulation or during the measurement, gives the opportunity to investigate differences between simulation and measurement in more detail. For the first time since beginning of the development of ICON-ART, a nested domain is used for photolysis rate calculations. The two way nesting technique allows simulations with a higher resolution without any inconsistencies. Boundary conditions are directly calculated during run time. With the comparison between results of the nested and global domain, the benefits of the nested domain are shown.

The vertical profile, affected by the presence of clouds, is of high importance for reasonable simulations of chemical constituents in the Earth's atmosphere. With ICON-ART, it is possible to simulate a realistic photolysis rate profile including enhancement and reductions

due to the presence of clouds. This has been shown for four different photolysis rates, capturing the important wavelength regions for the UTLS region.

5 Characterisation of ozone and water vapour feedbacks in ICON-ART

The integration of interactive water vapour and ozone calculation in global modelling systems is a mandatory step to get a better understanding of global climate changes (e.g. Eyring et al., 2006; Braesicke et al., 2013, 2006). These changes result from a complex interaction between atmospheric trace gases, temperature, dynamics and radiation. All components interact with each other on different temporal and spatial scales. The already mentioned Brewer-Dobson Circulation is a process on the global scale determining the global trace gas distribution. Ozone and water vapour have the ability to change stratospheric heating rates, also interacting with the global circulation pattern (e.g. de Forster and Shine, 1999; Kley et al., 2000). An important component of the atmospheric dynamics is the polar vortex regime, as described in section 2.4. The southern hemisphere polar vortex shows very low stratospheric ozone concentrations, forming the ozone hole (e.g. Kley et al., 2000). The spatial and temporal evolution of the southern hemisphere polar vortex and ozone hole has a strong impact on the stratospheric dynamics (e.g. Braesicke et al., 2006, 2013). The spatial extension of the polar vortex is of about a few hundreds of kilometers and it's variations of a few meters. Global circulation pattern refer to a much wider temporal and spatial extension. Here, ICON-ART shows its advantages over other modelling systems. With ICON-ART, it is possible to perform hindcasts with the NWP physics configuration and global climate projections with the climate physics configuration. For both physics configurations, an interactive simulation of atmospheric trace gases is possible. The first section of this chapter focuses on the description of the southern hemisphere polar vortex, including the ozone distribution. The focus is first set on the prominent vortex split event in 2002 and than shifted towards the climatological discussion on the impact of the interactive ozone calculation on southern hemisphere polar stratospheric temperatures. This discussion is followed in sections 5.4 to 5.11 by the investigation of ozone and water vapour feedbacks using climate integrations with ICON-ART. The following experiments and descriptions are also part of Schröter et al. (2018).

5.1 ICON-ART with different physics configurations

5.1.1 ICON-ART with NWP physics configuration - experimental setup

In 2002, an unusual split of the ozone hole was observed on 22 September 2002 and described by Newman and Nash (2005). The initiation of the splitting process is not fully understood yet. The split of the ozone hole had no chemical reason; instead it is dynamical change controlling composition and in particular ozone distributions. Several studies, e.g. Matsuno (1971) have shown that a vortex split event can be caused by atmospheric interactions with upward propagating planetary waves. Sinnhuber et al. (2003) pointed out, that the major stratospheric warming occurred far earlier than the normal final warming at the end of the ozone hole season. With ICON-ART is is possible to study the vortex split event of 2002 in a hindcast. First, the total ozone column simulated with ICON-ART is discussed. For the setup of the experiment, we use reanalysis data from the European Centre for Medium-Range Weather Forecasts (ECMWF) - ERA-Interim (Dee et al., 2011) to initialise the meteorological variables (e.g. pressure, temperature, water vapour and horizontal wind fields). The hindcast is initialised on 20 September 2002 00:00 UTC. The chosen grid is R2B6, corresponding to an approximate horizontal grid spacing of 40 km. The model top is at 75 km with 90 vertical levels. The integration time step is 240 s, and the output time step every hour.

5.1.2 ICON-ART with climate physics configuration - experimental setup

Further simulations in this chapter are configured in an AMIP (Atmospheric Model Inter-comparison Project) like experiment (Gates et al., 1999). The boundary conditions used are summarised in Table 5.1. Two experiments are set up on a R2B4 grid which corresponds to an effective horizontal grid spacing of 160 km. The integration time step for the physics routines is chosen to be 600 s and for the radiation 7200 s. Output is written every three days. Variables are interpolated on predefined pressure levels, corresponding to the standard ERA-Interim pressure levels. The first experiment uses an ozone climatology with monthly mean values based on Cionni et al. (2011). This simulation is called *ICON-ART control*. The feedback simulations use the interactive ozone as well as the additional tendencies on water vapour due to methane oxidation. The simulation where both tendencies influence the radiation is called *ICON-ART feedback*. For the setup of the experiments, data from ERA-Interim (Dee et al., 2011) is used for initialisation of the meteorological values (e.g. pressure, temperature, water vapour and wind fields). The simulations of ICON-ART are free running simulations.

Variable	Reference
SST/SIC	Taylor et al. (2000)
Spectral solar irradiation	Lean et al. (2005)
Greenhouse gases RCP 8.5	Riahi et al. (2007)
O3 concentration	Cionni et al. (2011)
Tropospheric aerosol	Stenchikov et al. (1998, 2004, 2009)
Stratospheric aerosol	Stenchikov et al. (1998, 2004, 2009)

Table 5.1: Overview of used references for boundary condition in AMIP like experiments

Experiment	Short name	O_3	H_2O
control	ctrl	AMIP	standard
feedback	feedb	LINOZ	methane oxidation

Table 5.2: Overview of experiments.

5.2 Investigation of the southern hemisphere polar vortex

The first study focuses on the southern hemisphere polar vortex. Here, two hindcast simulations of ICON-ART using the NWP physics configuration are used. One simulation shows the linearised ozone distribution, the other the result of the extended Chapman cycle simulation. Additionally, the passive polar vortex tracer is shown. For the investigation of the impact of interactive ozone and water vapour calculation, long term simulations using the climate physics configuration are discussed.

5.2.1 Characterisation of the polar vortex geometry with ICON-ART

To investigate processes, relevant in the region of stratospheric polar vortex, the polar vortex tracer in ICON-ART is introduced. The processes of interest include transport processes of air parcels from within the vortex, exchange processes at the vortex edge and mixing processes. The vortex tracer is a passive tracer, with no destruction over time. This means that the tracer is only affected by transport tendencies and has no interaction with other tracers. To define the edge of the polar vortex the first approach is to use Ertel's Potential Vorticity (PV) which is defined as follows:

$$PV = \frac{\zeta + f}{\rho} \frac{\partial \theta}{\partial z} \tag{5.1}$$

with ζ the relative vorticity, f the Coriolis parameter, ρ the air density of the specific model box, θ the potential temperature and z the geometric height. On a timescale of weeks and on an isentropic surface the PV is a conserved measure (Nash et al., 1996). The maximum

in the PV gradient defines the polar vortex edge. However, as this metric shows high variations in small horizontal regions, unique maximum cannot be defined. It is reasonable, to take a second metric into account following Nash et al. (1996) to get a unique definition. At the polar vortex edge, the horizontal wind component gets extremal and occurs as a surrogate for the PV gradient. In the model, the following steps are performed separately for each hemisphere: First, the PV is calculated at every grid point. Between minima and maxima of PV a sufficient number of equidistant isolines is defined. Then, the respective geographical area enclosed by the isolines is calculated. By determination of maximum westerly wind relative to the area under PV isolines and multiplication of both values gives a reasonable constraint for the polar vortex edge boundary region. The described definition holds for the location of the northern hemisphere polar vortex. For the southern hemisphere, the maximum of the easterly wind gives the constraint for the location of the edge.

At the initialisation time step, the passive tracer is filled with the value of one within the boundaries of the vortex. Afterwards only transport processes are in action. This gives a useful tool to investigate transport processes in the region of the polar vortex boundary.

In Figure 5.1, the temporal evolution of the passive vortex tracer of ICON-ART is depicted. The colour coding gives the arbitrary values of the vortex tracer at an interpolated pressure level of 30 hPa at midnight of the given date. Again, the date of initialisation is chosen to be 20 September 2002. In the corresponding snapshot, within the boundaries of the vortex, the tracer is filled with values of one. For the following time steps, only transport takes place. The horizontal spreading of the vortex tracer represents the dynamical evolution of the vortex over the southern hemisphere. The horizontal spreading corresponds to the horizontal distribution of the total ozone column in Figure 5.2. At the day of initialisation, the vortex is still intact, but in the following days the first major stratospheric warming at the southern hemisphere e.g. (Newman and Nash, 2005) is observed. The massive outflow of vortex air masses, beginning at 24 September 2002 can be observed by analysis of the vortex tracer. This outflow is correlated to the increased dynamical impact on the vortex integrity. The vortex split occurred at 26 September 2002. The structure, represented by the vortex tracer, is nearly separated. At this day the maximum latitude of 30° south of the vortex air filament has been reached. The vortex tracer allows to define those regions which can give an insight into the chemical composition of the isolated air within vortex air parcels, e.g. (McKenna et al., 2002) or (Konopka et al., 2005).

5.2.2 Investigation of ozone distributions during the vortex split event 2002

The simulated ozone column, interpolated on a regular latitude - longitude grid with a resolution of 0.5°, is shown in Figure 5.2. The four columns show daily means of total ozone
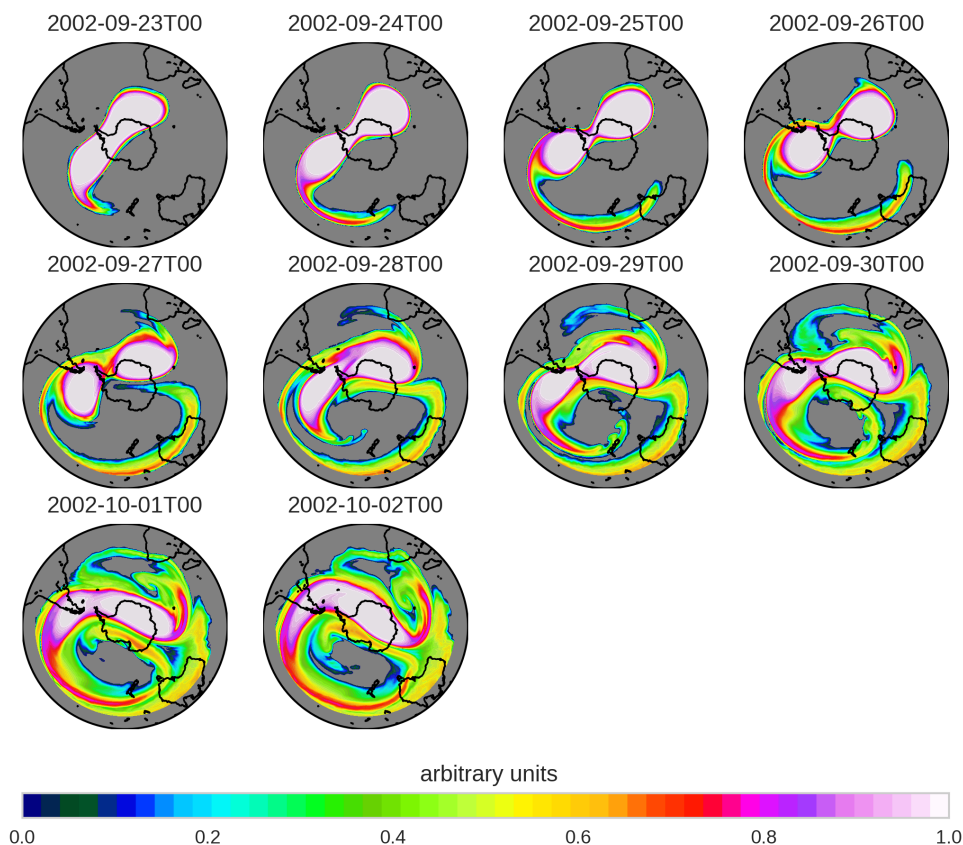
Figure 5.1: Vortex tracer case study - passive vortex tracer in arbitrary units. The figure shows snapshots of the simulation of the passive vortex tracer. Initialisation date was chosen to be 20th September. Within the vortex boundary, the passive tracer gets the value of one and is then transported. The figure represents snapshots at midnight UTC at 30hPa. Focus is set over the Antarctic.

for the respective dates. The mean is taken over all 24 output steps starting at 00:00 UTC. For the initial values of ozone, the ERA-Interim data is used analogous to the meteorological data. The ozone hindcasts are performed with two different schemes: The modified Linoz scheme as described in section 3.2.6 and a gasphase algorithm (the extended Chapman cycle) with reactions described in Table 3.2.9. For the comparison between simulations and measurements, satellite observations from TOMS instrument (TOMS Science Team, 2016) are used.

Five days after initialisation, the represented horizontal geometry of the total ozone column in both ICON-ART simulations is slightly different in comparison to the satellite observations. After more than ten days of simulation, the shape of the vortex is in good agreement with satellite observations again. Within the polar vortex, the total ozone column reaches values of about 200 DU in both, ICON-ART simulations and the satellite observations. At the end of the simulation, on 1 October 2002, the largest difference between the extended Chapman cycle simulation, using the full gas phase algorithm, and the simplified Linoz simulation is

found at 120°W, 70°S, outside of the polar vortex.The total ozone column reaches values of 450 DU and above for the extended Chapman cycle simulation. For the Linoz simulation, ozone destruction is slightly higher and values up to 400 DU are reached.

However, we can focus on the general spatial structures and how transport has modified ozone distributions. Inside the polar vortex, on 1 October 2002 , we model negative ozone loss for both simulations. The chemical tracer in both simulations is increased with respect to the passive one. The increase is higher in the Linoz simulation than in the extended Chapman cycle. This implies that temperatures in that region are not low enough to trigger the heterogeneous destruction of ozone in the Linoz scheme. Outside the polar vortex, mainly on 25 September, high values of ozone loss can be observed for the Linoz simulation but not for the extended Chapman cycle. This is also caused by the difference in addressing heterogeneous destruction. Within the Linoz scheme, the loss term has been triggered and we can observe additional ozone loss. This feature is missing for the extended Chapman cycle chemistry.
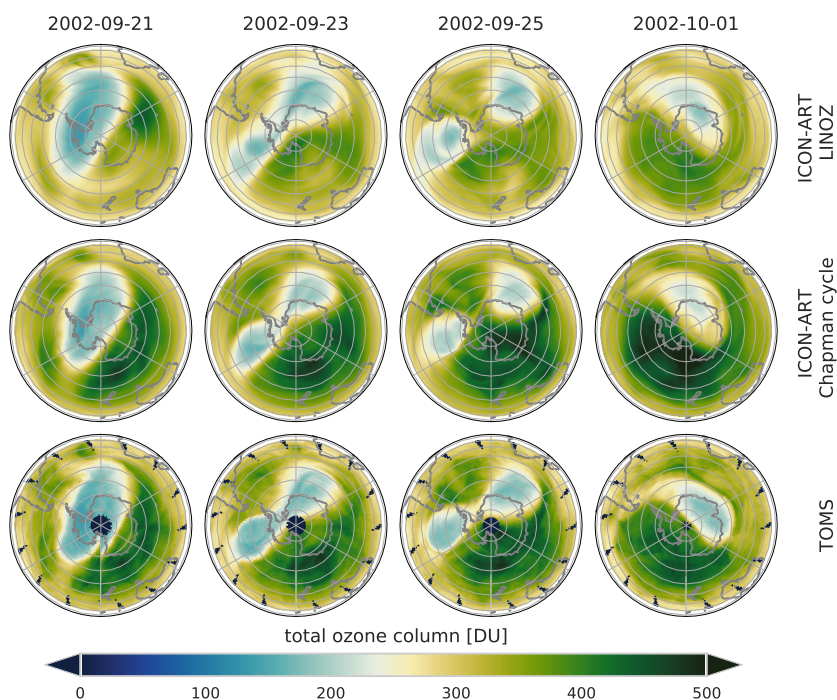
Figure 5.2: Antarctic total ozone column [DU] for a time sequence starting on 21 September 2002 finishing 01 October 2002 (left to right). Daily averages for two ICON-ART simulations for the Linoz chemistry scheme (top) and for the extended Chapman cycle chemistry (middle). TOMS observations are shown in the bottom. The model was initialised on 20 September 2002.

5.2.3 Feedbacks of asymmetric southern polar ozone distribution

The linearised ozone calculation shows reasonable results, as discussed in the previous section. Since full gas phase simulations show a high cost of computational time, parameterisations

of chemical tendencies are mostly used for climate integrations. In the following, the setup of ICON-ART described in section 5.1.2 (climate configuration) is used. Studies by, e.g. Waugh and Randel (1999), have shown that the southern hemisphere polar vortex has a large inter-annual variability in the midwinter upper stratosphere. Figure 5.3 shows the seasonal mean ozone distribution at 50 hPa for the control (top panel) and feedback (bottom) simulation of ICON-ART.
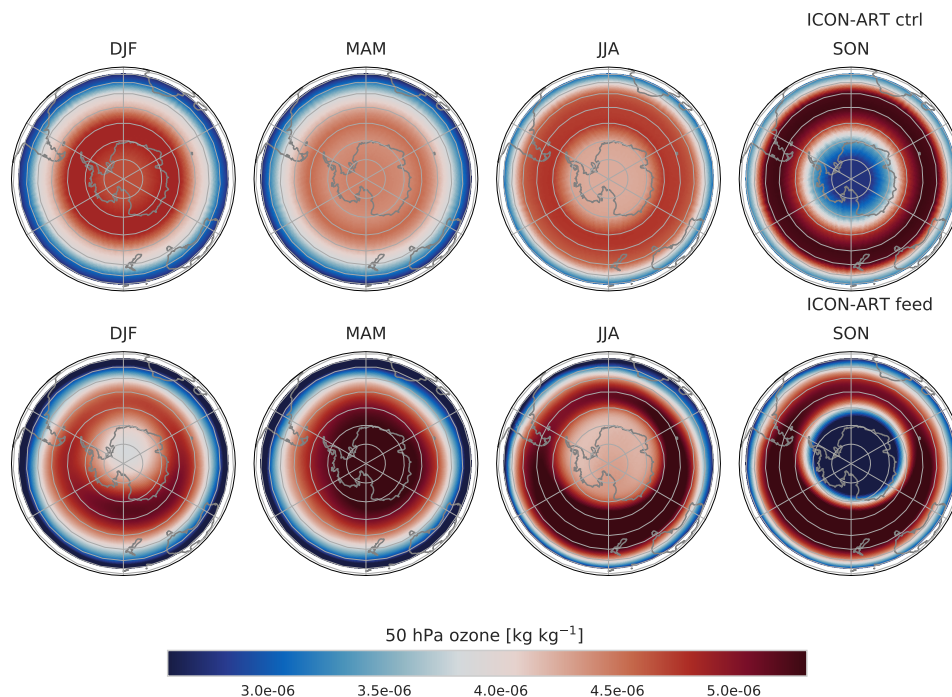
Figure 5.3: Antarctic seasonal mean ozone distribution at 50 hPa for the time period between 1980 and 2009. Top: control simulation with ozone climatology; Bottom: Feedback simulation of ICON-ART with interactive Linoz ozone.

The control simulation shows a pole centred circle of low ozone mass mixing ratios of about 3.5×10^{-6} kg kg^{-1} between September and November. The geometry of this circle stays unchanged during the year. This geometric characterisation was already indicated in Figure 5.12 in the previous section. The shape of low ozone values in the feedback simulation shows a varying geometry, not completely pole centred. Minimum ozone values between September and November are much lower of the order of 2.5×10^{-6} kg kg^{-1}. The shape is not a perfect circle and slightly shifted towards 60 °E (first clockwise straight grid line). Since ozone has a strong radiative impact, a misplaced ozone hole leads to structural temperature differences. Even near surface temperatures are changed by changing characteristics of the polar ozone distribution as shown in Figure 5.4. The differences in the seasonal mean temperatures between control and feedback simulation of ICON-ART are the highest between September and November. Here, the temperature difference at 50 hPa is about 6.1 K (maximum color shading not shown). Since the ozone hole is shifted in easterly
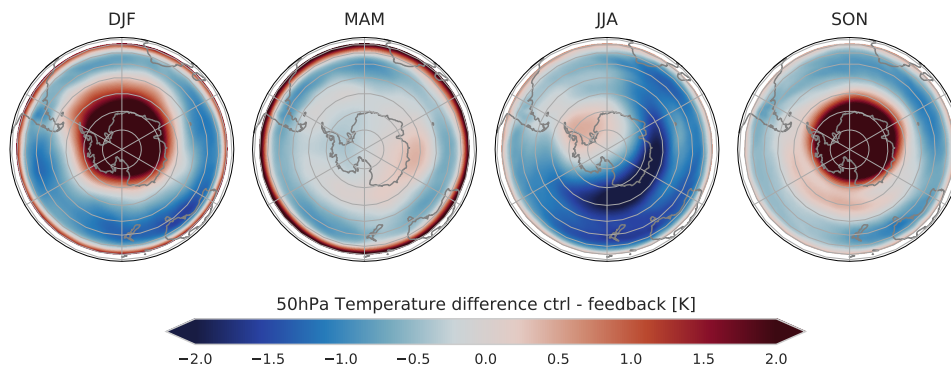
Figure 5.4: Antarctic seasonal mean temperature difference at 50 hPa between control and feedback simulation for the time period between 1980 and 2009.

direction, higher ozone values at 50 hPa are present in the feedback simulation. Higher stratospheric ozone levels result in higher radiative absorption and thus heating rates are changed throughout the atmosphere. Even near surface vertical levels show a temperature differences up to 1.5 K, as seen in Figure 5.5. Here, the difference is taken for the interpolated pressure level at 1000 hPa. The near surface temperature difference is the highest between September and November. Not only over the Antarctic, a difference of about 1.5 K occurs, also over Australia temperature differences greater than 1.5 K occur. Over Australia, changes in the stratospheric ozone are small compared to those over Antarctica.
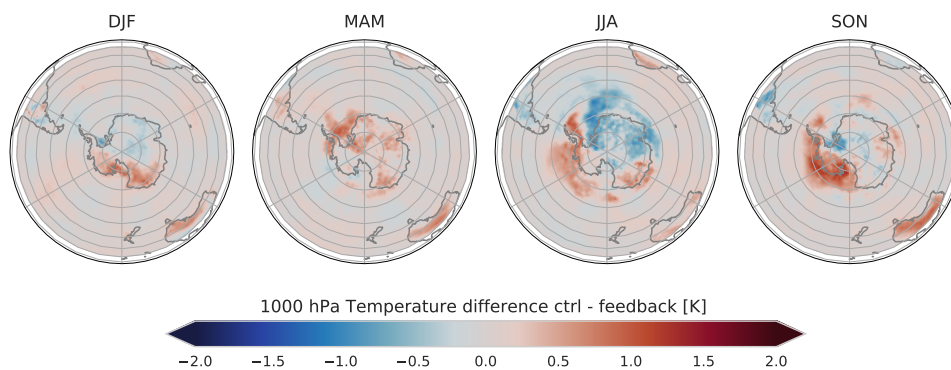
Figure 5.5: Antarctic seasonal mean temperature difference at 1000 hPa between control and feedback simulation for the time period between 1980 and 2009.

The asymmetry of the southern hemisphere ozone hole results in stratospheric cooling. The detailed investigation of the southern hemisphere polar vortex and ozone distribution shows, that the interactive ozone calculation is a beneficial implementation of ICON-ART. Other studies, like Crook et al. (2008); Keeble et al. (2014) and Dennison et al. (2017) also emphasise the importance of interactive ozone calculation for climate investigations. By using an non-interactive ozone climatology without any interaction with radiation and dynamics, important processes influencing the global climate, are neglected.

5.3 Investigation of the global composition and circulation interaction

5.3.1 Interactive and non-interactive ozone distribution

Major differences between both ICON-ART simulations are expected in the seasonal and zonal mean ozone distribution. Figure 5.6 shows the seasonal latitude-height distribution of ozone. For the control simulation, a climatological dataset (Cionni et al., 2011) is used. Maximum values appear in the upper stratosphere between $10\,\mathrm{hPa}$ and $5\,\mathrm{hPa}$ of approximately $1.5 \times 10^{-5}\,\mathrm{kg\,kg^{-1}}$ for the control simulation. The feedback simulation shows an ozone maximum at the same altitude with a slightly higher value of $1.7 \times 10^{-5}\,\mathrm{kg\,kg^{-1}}$. In general, regarding the stratospheric maximum, ERA-Interim is in good agreement to the latitude-height distribution of both ICON-ART simulations. The maximum value of the feedback simulation is closer to ERA-Interim than the control simulation.
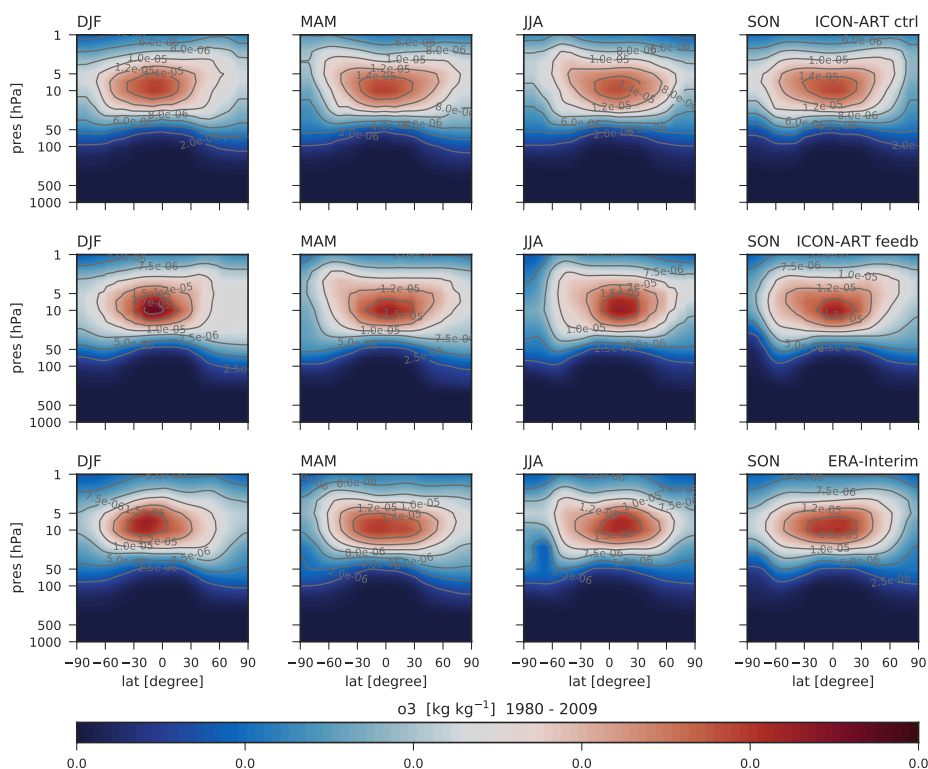
Figure 5.6: Latitude-height cross sections of seasonal and zonal mean ozone $[\mathrm{kg\,kg^{-1}}]$ for ICON-ART simulations and ERA-Interim from 1980 - 2009. Top: control run; Middle: feedback simulation; Bottom: ERA-Interim

Differences between the seasonal latitude - height cross sections are depicted in Figure 5.7. The biggest difference between both ICON-ART simulations is found above $5\,\mathrm{hPa}$ between June and August (JJA). In this season the ozone climatology of the control run shows values of about $3.5 \times 10^{-6}\,\mathrm{kg\,kg^{-1}}$ higher than the feedback simulation. In general, the

differences are higher in the southern hemisphere than in the northern hemisphere between September and October (SON). In the mid-latitude stratosphere at $100\,\text{hPa}$, differences are of the order of $4 \times 10^{-8}\,\text{kg}\,\text{kg}^{-1}$.
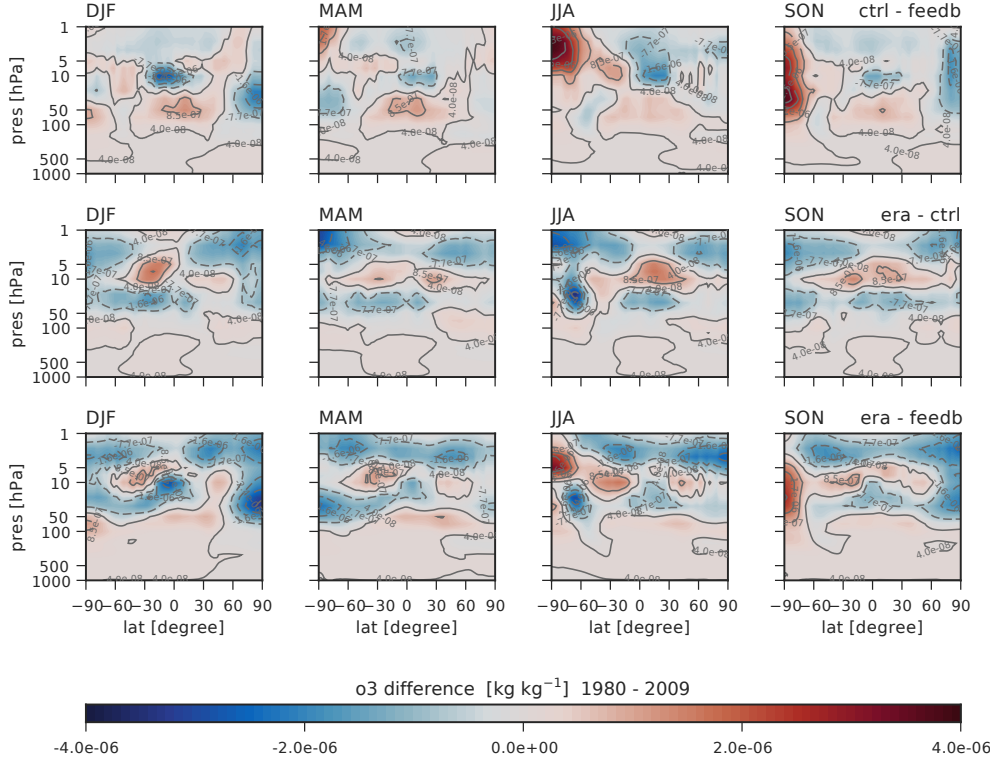
Figure 5.7: Latitude-height cross sections of seasonal and zonal mean ozone differences $[\text{kg}\,\text{kg}^{-1}]$ for ICON-ART simulations and ERA-Interim from 1980 - 2009. Top: control run minus feedback simulation ; Middle: ERA-Interim minus control simulation; Bottom: ERA-Interim minus feedback simulation

Differences between ERA-Interim and the ICON-ART control simulation show a deviating pattern compared to the differences in-between the ICON-ART simulations. Between December and February (DJF), between $30\,°\text{S}$ and equator and above $10\,\text{hPa}$, ozone values of ERA-Interim are $8.5 \times 10^{-7}\,\text{kg}\,\text{kg}^{-1}$ higher than of the ICON-ART control run. The extension of this difference pattern is reduced for the ICON-ART feedback simulation. For the time period between March and May (MAM), differences between both ICON-ART simulations are the smallest, of all four seasons. The highest deviation occurs in the southern hemisphere polar upper stratosphere. Here, ozone mass mixing ratios of the control simulation are higher than for the feedback run. The differences reach a value of $1.6 \times 10^{-6}\,\text{kg}\,\text{kg}^{-1}$. As seen in the bottom panel of Figure 5.7, the difference between ERA-Interim and ICON-ART is reduced for this region using the interactive ozone. The contour lines of the middle and bottom row indicate that between March and May the overall pattern of differences between ICON-ART and ERA-Interim is comparable for both simulations. Between June and August, the high deviation in the southern hemisphere polar

stratosphere, between both ICON-ART simulations is up to $4 \times 10^{-6}\,\mathrm{kg\,kg^{-1}}$. Compared to ERA-Interim, the existing negative bias of the control simulation is compensated in this region. Where the difference between ERA-Interim and control simulation is negative with a value of approximately $-1.6 \times 10^{-6}\,\mathrm{kg\,kg^{-1}}$, the difference between ERA-Interim and feedback simulation becomes positive ($3.5 \times 10^{-6}\,\mathrm{kg\,kg^{-1}}$).

The linearisation of ozone tendencies results in an ozone destruction for the polar stratosphere between March and August in the southern hemisphere. A reduced mass mixing ratio of ozone can still be observed in SON at $50\,\mathrm{hPa}$. The difference between control and feedback simulation is weaker than in the months before ($2.5 \times 10^{-6}\,\mathrm{kg\,kg^{-1}}$).

In general, differences between both, the climatology and the interactive ozone, are the highest for the southern hemisphere polar stratosphere. This feature results in a change of sign of the difference for both comparisons of ERA-Interim to ICON-ART.

Figure 5.8 shows monthly averages of zonal mean ozone. The monthly means are plotted twice to get a better impression of the temporal evolution. All panels show the latitude-time cross section for the time period between 1980 and 2009 at $50\,\mathrm{hPa}$. The left panel represents the latitude-time cross section for the control simulation. The ozone climatology shows low values over the complete mean year ($1 \times 10^{-6}\,\mathrm{kg\,kg^{-1}}$) in the tropics and subtropics up to $\pm 30°$. Only slight deviations are visible. The middle panel represents the non-interactive result of the Linoz parameterisation. Tendencies are calculated based on the same temperatures as in the control simulation. The resulting ozone mass mixing ratio has no impact on the radiation. Compared to the left panel, the non-interactive ozone latitude-time cross section in the tropics is smaller. Between $\pm 30°$, values around $2 \times 10^{-6}\,\mathrm{kg\,kg^{-1}}$ can be noted. In the northern hemisphere (NH), much higher values occur. Where the climatological ozone distribution shows maximum values of $5 \times 10^{-6}\,\mathrm{kg\,kg^{-1}}$, the non-interactive distribution reaches values up to $8 \times 10^{-6}\,\mathrm{kg\,kg^{-1}}$. The right panel represents the interactive ozone simulation of ICON-ART. Here, the tropics show a comparable result to the non-interactive simulation. However, the northern hemisphere maximum value is slightly smaller compared to the non-interactive simulation.

The most obvious differences between the three shown panels is located in the region of the southern hemisphere polar vortex. Values of the non-interactive and interactive simulation are much smaller (below $2 \times 10^{-6}\,\mathrm{kg\,kg^{-1}}$) compared to the values of the control simulation (approximately $2.5 \times 10^{-6}\,\mathrm{kg\,kg^{-1}}$). The temporal extent of these low values of ozone is larger for the interactive distribution than for the non-interactive one. For the control simulation, using the ozone climatology, low values on the southern hemisphere only occur between late August to end of November. For the non-interactive distribution, low values start up to half a month earlier and stay longer until the end of December. The longest time period is shown by the interactive simulation, from late August to end of January.
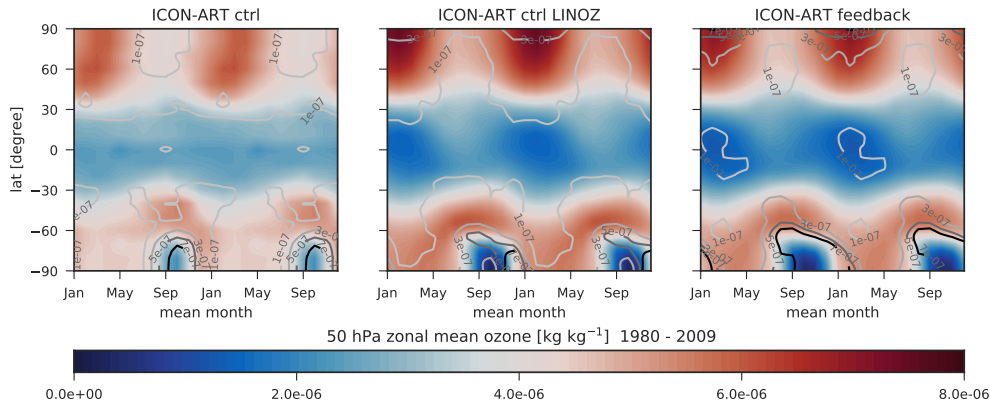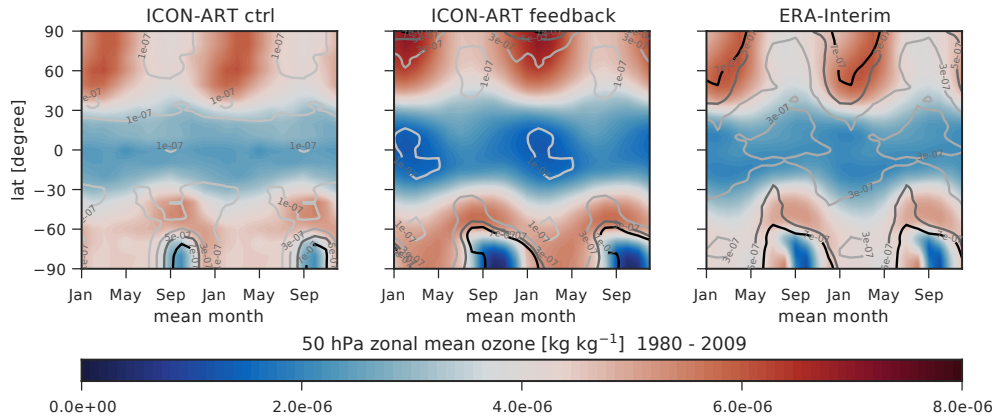
Figure 5.8: Monthly averaged zonal means of ozone [kg kg^{-1}] at 50 hPa (shown twice) for the period from 1980 to 2009 (shaded). Contour lines represent the standard deviation of the monthly means. Left panel: ozone climatology as used in the control simulation; middle panel: non-interactive Linoz ozone; right panel: interactive Linoz ozone.

The contour lines in Figure 5.8 are representing the standard deviation. The black contour line represents a standard deviation of 1×10^{-7}kg kg^{-1}. Brighter colours represent higher values of the standard deviation with a spacing of 2×10^{-7}kg kg^{-1}. Calculating the ozone distribution with the Linoz parameterisation under consideration of the correction term for a shorter ozone life time due to the presence of polar stratospheric clouds, the southern hemisphere polar vortex seems to be stable up to three months longer than in the control run. From August to December, very low ozone concentrations of about 0.5×10^{-5} kg kg^{-1} can be observed in the panel for the non-interactive simulation. Figure 5.8 shows the latitude-time cross section for the monthly averaged zonal mean ozone distribution of ERA-Interim (right panel) besides the ICON-ART control and feedback simulations (left and middle panel). The shown standard deviation and minimum values in the southern hemisphere of the ICON-ART feedback simulation are closer to ERA-Interim than the control simulation. Only the temporal extent of the southern hemisphere minimum ozone of the ICON-ART control simulation fits better to ERA-Interim than the feedback simulation. High values of standard deviation for ERA-Interim (7×10^{-7} kg kg^{-1}) represent a high inter-annual variability. For a few years between 1980 and 2009, low values of monthly mean ozone occur in the same time period as shown by the ICON-ART feedback simulation.

For the interactive simulation, low ozone concentrations in the southern hemisphere minimum temperatures occur until end of January.

The default climatology of the ICON-ART control simulation does not represent very low values of ozone concentrations. This misrepresentation has also been discussed by e.g. Arblaster et al. (2014). Here, the authors point out that most models that are using a prescribed ozone climatology tend to under estimate the Antarctic ozone depletion. Thus, modelled ozone values are higher than indicated by observations between 1979 and 2007 (e.g. Hassler et al., 2013). Taking the standard deviation into account, the characteristics

Figure 5.9: Monthly averaged zonal means of ozone [kg kg^{-1}] at 50 hPa (shown twice) for the period from 1980 to 2009 (shaded). Contour lines represent the standard deviation of the monthly means. Left panel: ozone climatology as used in the control simulation; middle panel: interactive Linoz ozone; right panel: ERA-Interim.

of the AMIP ozone climatology (Cionni et al., 2011) becomes clearer. The contour lines represent a semicircle each winter in the southern hemisphere that is aligned with the ozone concentration gradients. This symmetric and coherent pattern of the ozone minimum is most likely not a very realistic representation of variability on top of an ozone hole that is not deep enough. The standard deviation isolines for the modelled ozone are different and intersect the isolines of ozone concentrations with higher variabilities at later times in the ozone hole period. This seems a more realistic behaviour, however we do not claim that this is already a perfect representation in comparison to the reanalysis data.

5.3.2 Changes in the global temperature distribution

The previous section has shown that a changing ozone distribution has a strong impact on the surface temperature. But not only the surface temperature is changed, changes occur throughout the entire atmosphere. The impact of an altered ozone distribution on atmospheric temperatures is investigated in this section. It has been shown that great differences in the zonal mean ozone distribution between control and feedback simulation appear within the stratosphere. Figure 5.10 shows the latitude-height cross sections of seasonal and zonal mean temperature given in K. In the northern hemisphere winter (DJF), temperatures of 210 K are reached between 100 hPa and 10 hPa. For the season JJA, the temperature minimum in the tropics is at 100 hPa with temperatures as low as 200 K in both ICON-ART simulations. In the southern hemisphere winter, ICON-ART reaches temperatures of about 200 K. The northern hemisphere summer is represented by temperatures higher than 260 K above 5 hPa.
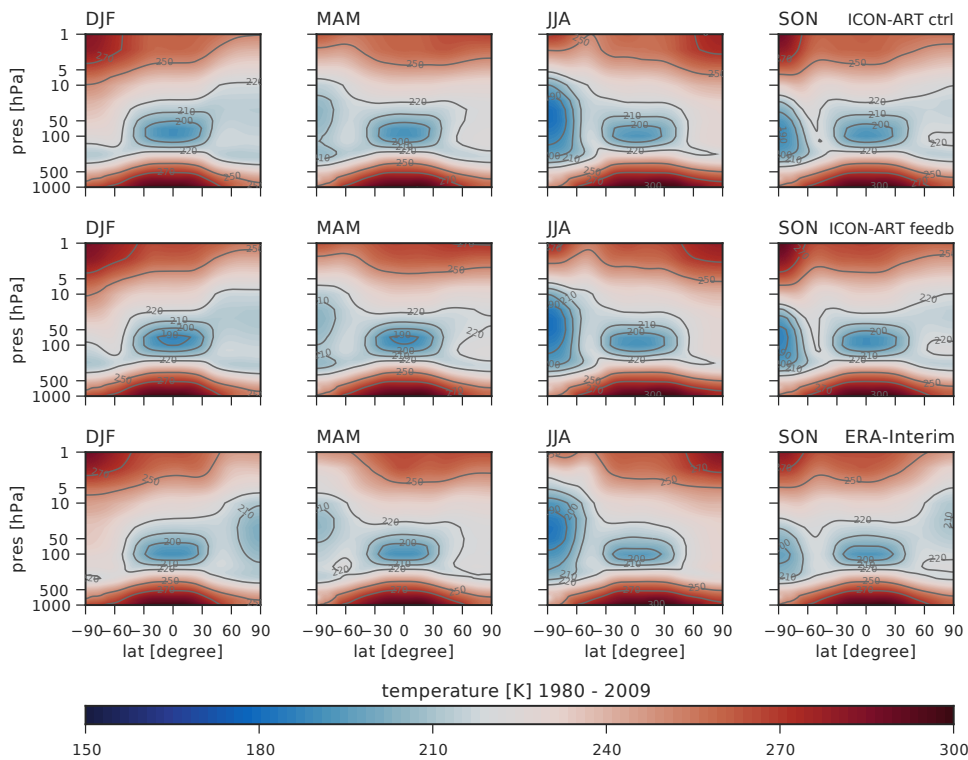
Figure 5.10: Latitude-height cross sections of seasonal and zonal mean temperature [K] for ICON-ART simulations from 1980 - 2009. Top: control run; middle: feedback simulation; bottom: ERA-Interim.

Figure 5.11 shows the difference between control and feedback run. Due to the stabilised polar vortex temperature, differences up to 5.4 K occur. The control run shows warmer temperatures in the southern polar region up to 20 hPa. Above this altitude, the feedback run is warmer than the control run. Again, this is due to the different ozone distribution in the

southern hemisphere winter. Within the tropical stratosphere, temperature differences about 2.8 K can be seen. Since the ICON-ART control simulation shows warmer temperatures than the ICON-ART feedback simulation, the latter simulation seems to be more reasonable. Like indicated by e.g. Arblaster et al. (2014), most models show a tropical tropopause with too low temperatures.

The differences of zonal and seasonal mean temperatures between ERA-Interim and the ICON-ART feedback simulation is shown in the bottom panel of Figure 5.11. The feature of a long lasting southern hemisphere polar vortex is present as well, seen in high temperature differences of up to 20 K from September to November (SON). The general structure is comparable to the results shown in the comparison studies of ECHAM5 (Roeckner et al., 2006). In this study, ECHAM5 is compared to ERA-Interim. The difference between ERA-Interim and ICON-ART is decreased in the southern hemisphere stratosphere due to the more realistic representation of the polar vortex. The ICON-ART feedback simulation shows higher temperatures compared ERA-Interim of about 5 K around 50 hPa.
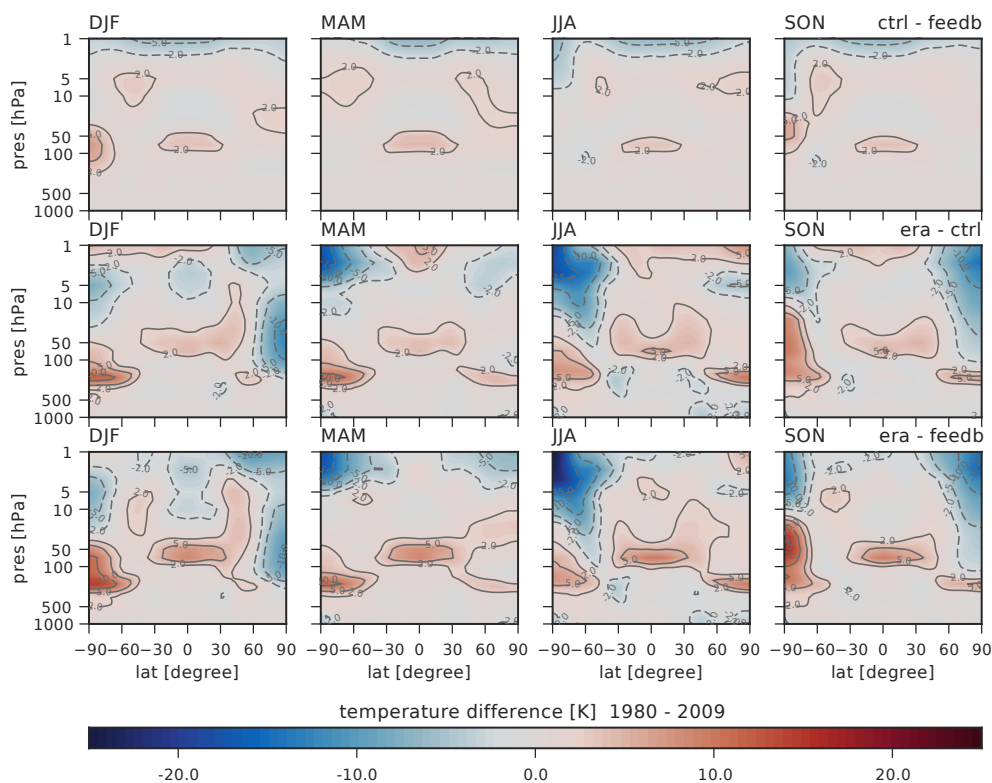
Figure 5.11: Latitude-height cross sections of seasonal and zonal mean temperature differences [K] for ICON-ART simulations and ERA-Interim from 1980 - 2009. Top: control run minus feedback simulation ; Middle: ERA-Interim minus control simulation; Bottom: ERA-Interim minus feedback simulation.

In Figure 5.12, the monthly averaged zonal mean of the temperature is shown twice for a better representation of the temporal evolution. For this analysis, the time period from 1980 to 2009 is included. Minimum temperatures in the southern hemisphere are

comparable between ERA-Interim, the ICON-ART control and feedback simulation. The minimum temperatures in ERA-Interim are slightly higher. The extend of the minimum temperature differs between both ICON-ART simulations and ERA-Interim. For the ICON-ART feedback simulation, low temperatures remain longer than in the ICON-ART control simulation. From end of April to November, the southern hemisphere temperatures stay below 200 K for the feedback simulation. In the control simulation, temperatures start to rise again up to half a month earlier. The inter-annual variability, indicated by the shown dark grey contour lines of 10 K, has a larger temporal extend in the feedback simulation than in the control simulation. The high variability of 10 K is only present in November for the control simulation. Temperatures in the feedback simulation show this variation from October to January. This variability is caused by the higher variability of the zonal mean ozone distribution in this area.
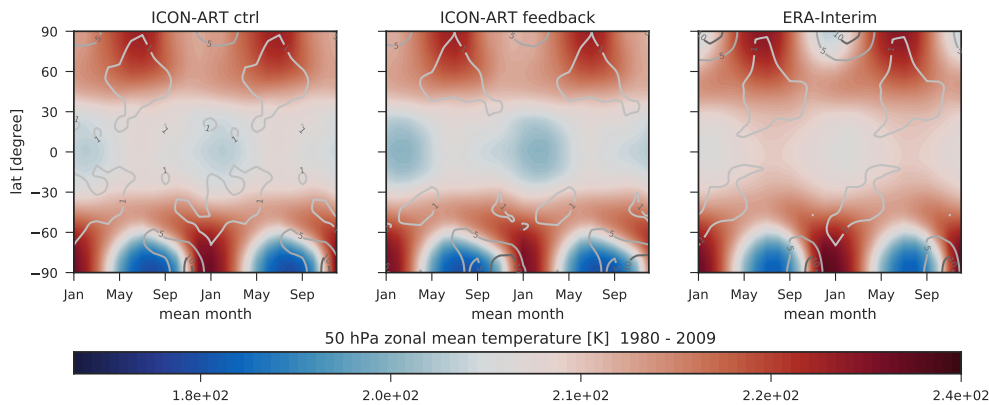
Figure 5.12: Monthly averaged zonal means of temperature [K] at 50 hPa (shown twice) for the period from 1980 to 2009 (shaded). Contour lines represent the standard deviation of the monthly means. Left panel: ozone climatology as used in the control simulation; middle panel: feedback simulation of ICON-ART; right panel: ERA-Interim.

The inter-annual variability of the zonal and monthly averaged temperature of ERA-Interim is in better agreement to the control simulation than to the ICON-ART feedback simulation. The temporal extend of minimum temperatures is a little smaller than in both ICON-ART simulations. The monthly averaged temperatures in middle latitudes within $\pm 30°$ show also differences between the shown simulations and ERA-Interim. For the feedback simulation, slightly lower temperatures of about 200 K occur compared to the control simulation between January and May. The temperature of ERA-Interim is even higher in this region than shown by the ICON-ART control simulation. The monthly mean temperatures reach up to 210 K for ERA-Interim. Additionally, the inter-annual variability of 1 K shows a different structure in the latitude - time cross section than in both ICON-ART simulations. The northern hemisphere shows the smallest deviations in-between the three different temperature cross sections. Only ERA-Interim shows temperatures down to 205 K with a high inter annual

variability of 10 K in January. Both ICON-ART simulations show a temperature around 210 K with a variability of 5 K.

By the investigation of stratospheric temperatures for all three cases, it can be concluded that the changed ozone and water vapour distribution has a strong impact. The changed ozone distribution is mainly present in the southern hemisphere polar region. In this region, also the highest temperature differences appear. The tropical changes of stratospheric temperature are also mainly caused by changes in the ozone distribution as shown in section 5.3.1. In the following section, the focus of the investigation is moved from the stratospheric temperature changes, to the overall atmospheric changes from the troposphere to the stratosphere. Up to now, only the differences in the ozone distribution between control and feedback simulation is discussed. The ozone distribution has probably the more dominant impact than changes in the water vapour distribution. Nevertheless, the changes due to altering water vapour concentrations in the stratosphere for the ICON-ART feedback simulation will be discussed in the next sections.

5.3.3 Feedbacks on zonal wind fields

Changes in temperature due to radiative feedback effects of ozone and water vapour are also affecting the zonal wind structure. The zonal mean zonal wind is shown in Figure 5.13. The top row shows the seasonal mean of the control ICON-ART simulation and the middle row the feedback simulation. In the bottom row, zonal mean zonal wind latitude-height cross sections for ERA-Interim are shown. In both ICON-ART simulations, a strong eastward zonal wind with wind speeds up to $60 \, \mathrm{m \, s^{-1}}$ is reached in the southern hemisphere winter (JJA). The wind speed patterns in the tropical stratosphere also matches the seasonal mean analysis. The location and magnitude of the subtropical jet is nearly identical in both simulations in comparison to ERA-Interim.

The top row of Figure 5.14 shows the difference between both ICON-ART simulations. The middle row shows the difference between ERA-Interim and the control simulation and the bottom row the difference between ERA-Interim and the feedback simulation. Between $100 \, \mathrm{hPa}$ to $200 \, \mathrm{hPa}$, the difference between control and feedback simulation is below $5 \, \mathrm{m \, s^{-1}}$. The amplitude and location of the subtropical jet agree with the ERA-Interim wind pattern for both simulations

Strong differences in the stratospheric zonal wind can be seen in the northern hemisphere winter. Here, the ERA-Interim shows values up to $25 \, \mathrm{m \, s^{-1}}$ higher than in both ICON-ART simulations. Between 30° and 60° latitude above 20 hPa, the sign of the differences changes. Here, we observe stronger zonal wind speeds than in ERA-Interim. The pattern is in agreement with the comparison studies shown in Roeckner et al. (2006). Here, the authors compare ECHAM5 zonal mean zonal wind pattern with ERA-Interim.
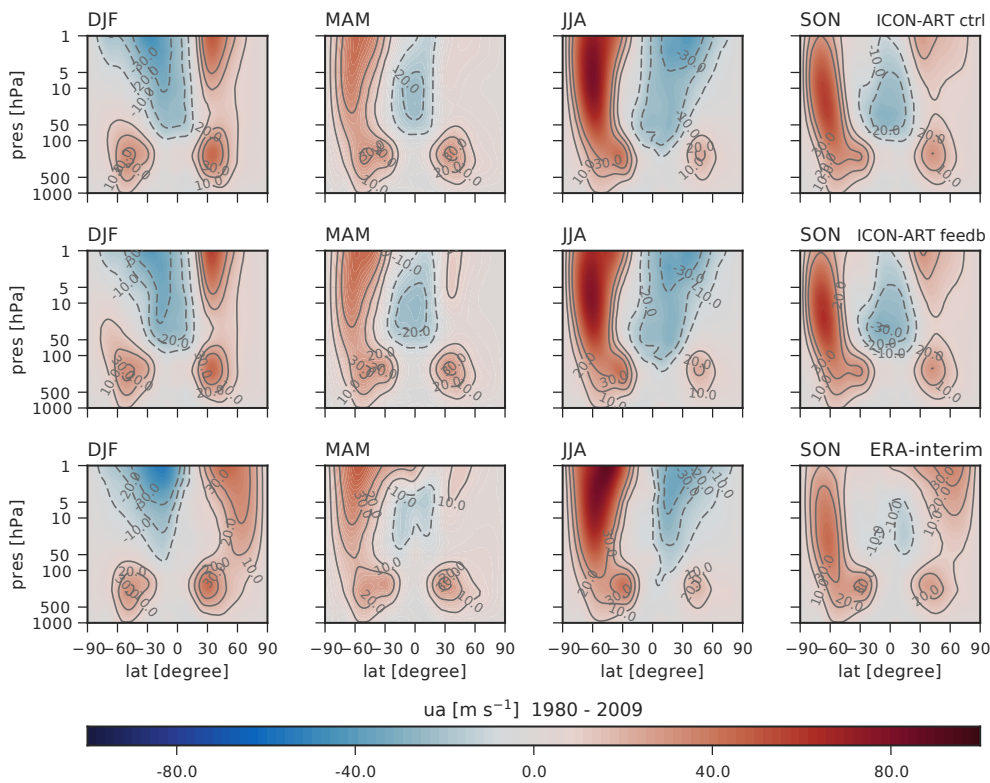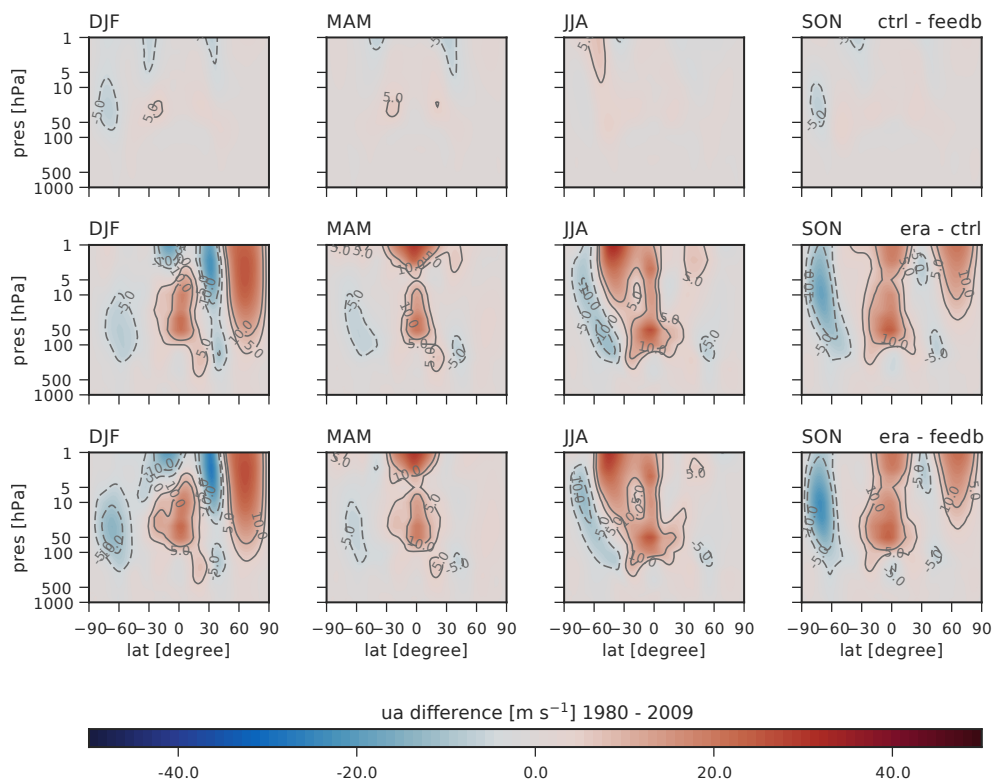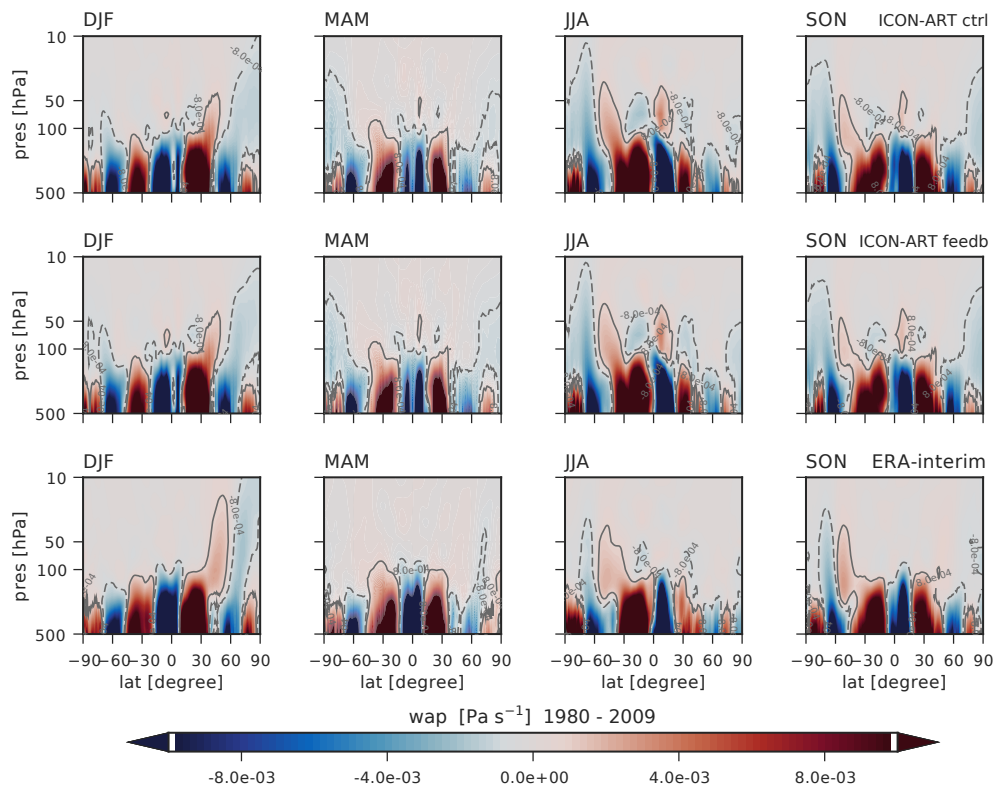
Figure 5.13: Latitude-height cross sections of seasonal and zonal mean zonal wind $[\mathrm{m\,s^{-1}}]$ for ICON-ART simulations and ERA-Interim from 1980 - 2009. Top: control run; Middle: feedback simulation; Bottom: ERA-Interim. Contour lines are set at $\pm 30\mathrm{m\,s^{-1}}$, $\pm 20\mathrm{m\,s^{-1}}$ and $\pm 10\mathrm{m\,s^{-1}}$.

Stratospheric high latitude easterly winds at the southern hemisphere are weaker in the feedback simulation than in the control run. This is caused by the lower stratospheric temperatures in the winter months (DJF), shown in section 5.3.2, Figure 5.12. Stratospheric tropical westerly wind patterns seem to be shifted pole-ward for both ICON-ART simulations with respect to ERA-Interim from June to August. The highest differences for both ICON-ART simulations in contrast to ERA-Interim occur for the tropical stratosphere, above $50\,\mathrm{hPa}$. The control simulation shows easterly winds up to $-20\,\mathrm{m\,s^{-1}}$. For the feedback simulation, the zonal wind speed is only slightly higher whereas the maximum for ERA-Interim is about $-10\,\mathrm{m\,s^{-1}}$. The highest difference between control and feedback simulation is seen in southern hemisphere easterly winds over Antarctica. This can be caused by the increased stability of the southern polar vortex as shown in the sections before. Additionally, high temperature differences occur over the southern hemisphere. If the polar vortex stability is changed, also horizontal wind patterns and the general stratospheric overturning circulation is changed (e.g. Eyring et al., 2006). The overall patterns are similar to the differences of ECHAM5 to ERA-Interim shown in Roeckner et al. (2006).
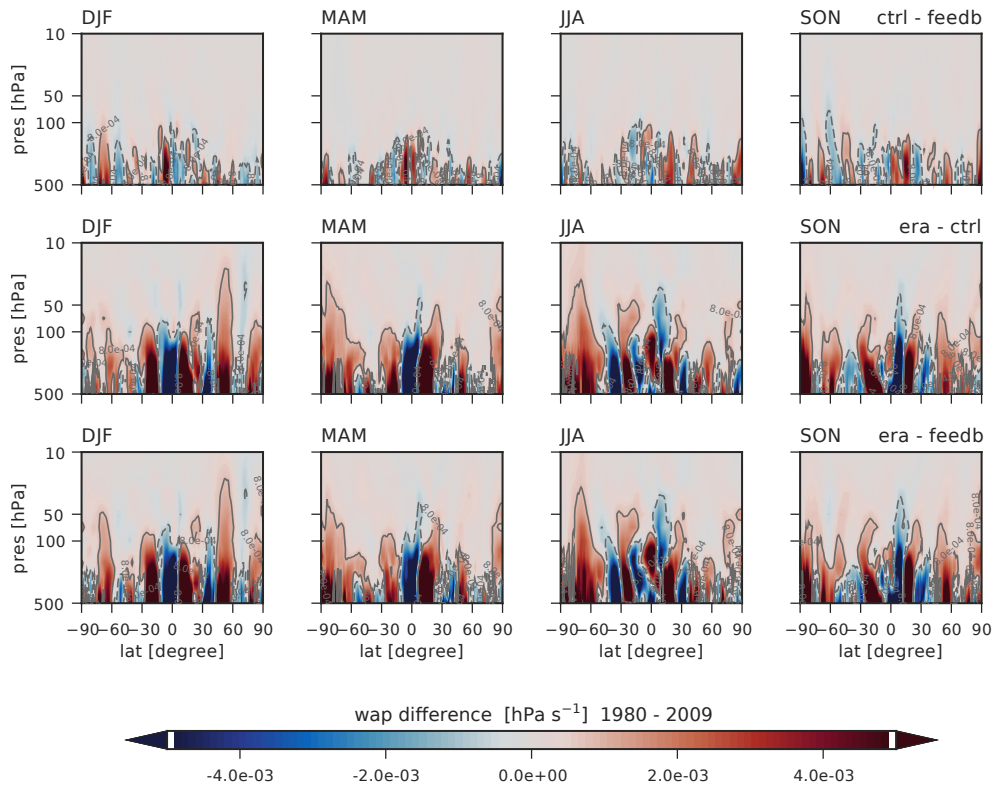
Figure 5.14: Latitude-height cross sections of seasonal and zonal mean zonal wind differences $[\text{m s}^{-1}]$ for ICON-ART simulations and ERA-Interim from 1980 - 2009. Top: control run minus feedback simulation ; Middle: ERA-Interim minus control simulation; Bottom: ERA-Interim minus feedback simulation. Contour lines are set at $\pm 10\text{m s}^{-1}$ and $\pm 5\text{m s}^{-1}$.

Not only the zonal mean zonal wind fields represent large scale dynamics in the Earth's atmosphere. The representation of the vertical wind field is an important factor to gain a more consistent picture for the large scale meridional circulations.

The zonal mean vertical wind field, given in Pa s^{-1} for both ICON-ART simulations and ERA-Interim, is shown in Figure 5.15. The differences are depicted in Figure 5.16. In both Figures the zonal mean vertical wind is averaged for the four separate seasons. Since ICON-ART is a non-hydrostatic model, the vertical wind component is a prognostic variable, whereas for in ERA-Interim, the vertical wind is a diagnostic quantity. Both Figures include the altitude range above $500\,\text{hPa}$, instead of starting at $1000\,\text{hPa}$.

At a first glance it can be stated that the zonal mean vertical wind shows a comparable pattern of up and downwelling vertical wind between ICON-ART control and feedback simulation. Also the difference in the upper most panel of Figure 5.16 reflects this impression. Here, differences are smaller than $\pm 1 \times 10^{-3}\,\text{Pa s}^{-1}$ for all seasons. Highest differences between control and feedback simulation are found between December and May in the tropics. Here, the upwelling wind of the feedback simulation is slightly slower. Between June and November, differences in the tropics are smaller.

Figure 5.15: Latitude-height cross sections of seasonal and zonal mean vertical wind $[\mathrm{Pa\,s^{-1}}]$ for ICON-ART simulations and ERA-Interim from 1980 - 2009. Top: control run; Middle: feedback simulation; Bottom: ERA-Interim.

In both simulations, the seasonal variation between upwelling and downwelling zonal mean wind pattern is very well represented in comparison to ERA-Interim. Absolute values of the differences between ERA-Interim and ICON-ART are of the same order of magnitude as the total values. The upwelling wind in the tropics is much slower in ERA-Interim than for ICON-ART. Between December and May, the difference is larger than $4 \times 10^{-3}\,\mathrm{Pa\,s^{-1}}$. From June to November, differences in the southern hemisphere are more dominating than the differences in the tropics or the northern hemisphere.

The differences in the vertical wind patterns are in agreement to the findings of the sections before. Since temperatures in the southern hemisphere are much lower in ICON-ART than in ERA-Interim, upwelling vertical wind is increased. Figure 5.17 shows the monthly averaged zonal means of the vertical wind in ICON-ART and ERA-Interim at 50 hPa, in the same representation as, e.g. Figure 5.12. The results of both ICON-ART simulations are comparable. The meridional pattern, the variation between upwelling and downwelling wind and monthly variations are comparable to ERA-Interim. As already seen in the difference plot (Figure 5.16), upwelling wind in the southern hemisphere is increased. From May to September, between 0° to 30° the downwelling wind in ICON-ART is much more intense than in the ERA-Interim data. Between −30° to −60°, the downwelling wind pattern for

Figure 5.16: Latitude-height cross sections of seasonal and zonal mean vertical wind differences $[\mathrm{Pa\,s^{-1}}]$ for ICON-ART simulations and ERA-Interim from 1980 - 2009. Top: control run minus feedback simulation; Middle: ERA-Interim minus control simulation; Bottom: ERA-Interim minus feedback simulation
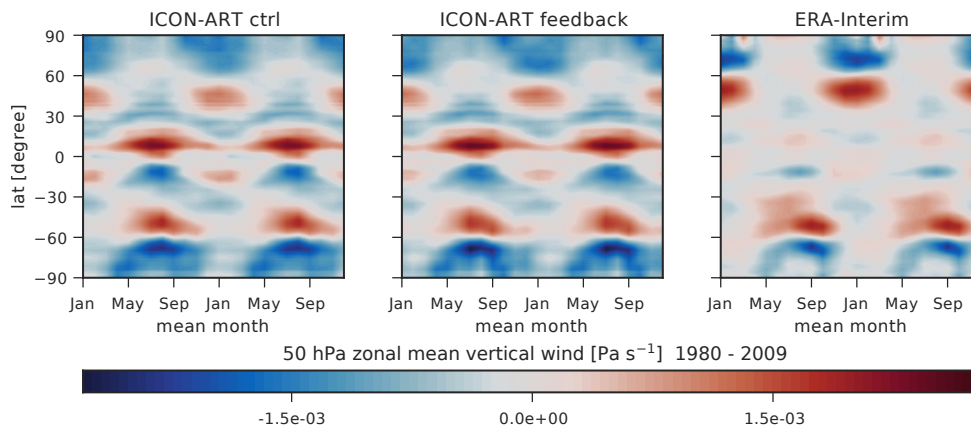
Figure 5.17: Monthly averaged zonal means of vertical wind $[\mathrm{Pa\,s^{-1}}]$ at $50\,\mathrm{hPa}$ (shown twice) for the period from 1980 to 2009 (shaded). Left panel: ICON-ART control simulation; middle panel: feedback simulation of ICON-ART; right panel: ERA-Interim.

ICON-ART shows a different structure compared to ERA-Interim for the time between May and September. The amplitude of about $1.4 \times 10^{-3}\,\mathrm{Pa\,s^{-1}}$ in ERA-Interim is weaker compared to the amplitude of $1.5 \times 10^{-3}\,\mathrm{Pa\,s^{-1}}$ (ICON-ART).

From the comparison of the zonal mean vertical wind in both ICON-ART simulations against ERA-Interim, it can be concluded that ICON-ART shows a sensible circulation pattern. The circulation pattern and seasonal changes for the region from the upper troposphere to the stratosphere are well captured. This is of high importance for a reasonable simulation of inter hemispheric transport. The strength of upwelling and dowelling zonal vertical wind shows greater difference between ICON-ART and ERA-Interim than between the ICON-ART simulations itself. Only in the tropics and the southern hemisphere differences between both ICON-ART simulations are reaching a value of $\pm 1 \times 10^{-3}\,\mathrm{Pa\,s^{-1}}$. By this conclusion it has been shown that ICON-ART is capable for a reasonable simulation of large scale stratospheric dynamics. However, for a more detailed characterisation of the changes induced by the altered ozone and water vapour distributions on stratospheric dynamics, further studies are necessary.

5.3.4 Discussion of changes in the stratospheric water vapour

This section is focusing first on the differences of the stratospheric water vapour distribution. This is followed by the study of the tropical water vapour tape recorder, for a characterisation of upward transport velocity in the tropics, based on the largest difference seen in this section between both ICON-ART simulations. As pointed out by the report of Arblaster et al. (WMO Assessment 2014), most atmospheric models underestimate global mean cooling rates in the lower stratosphere compared to e.g. satellite observations. The error sources have been proven to be caused by biases in the ozone trends (e.g. Solomon et al., 2012; Santer et al., 2013) as well as errors in the stratospheric water vapour distribution (e.g. Gettelman et al., 2010; Maycock et al., 2014). As the temperature decreases with increasing altitude, water vapour forms ice particles and sediments, as described by Mote et al. (1996); Fueglistaler et al. (2005, 2009) and Liu et al. (2010). This process is also called the process of *dry-freezing* (e.g. Brasseur and Solomon, 2006). Between several models, temperature biases occurred in the past causing problems in a sensible water vapour upward transport (Schoeberl et al., 2012). In Schoeberl et al. (2012), the authors compared several model results and ERA-Interim to measurements. As an example, the 100 hPa temperature of ERA-Interim is found to be colder than the observed temperature. As seen in the sections before, ICON-ART shows an even colder tropical tropopause region in both simulations compared to ERA-Interim. Thus, it is of high interest to investigate the stratospheric water vapour and its transport through the tropopause with ICON-ART in more detail. As seen in the sections before, besides the atmospheric ozone distribution, also stratospheric water vapour can have a strong impact on stratospheric climate. Stratospheric water vapour has a cooling effect on the stratosphere of the same order of magnitude as the effect of ozone depletion (de Forster and Shine, 1999). Thus, the study of the water vapour tape recorder is an important tool for the further understanding of large scale transport processes.

In the previous sections, changes within ICON-ART were investigated in connection to changes in the ozone distribution. In the next step, the focus is shifted towards changes in atmospheric water vapour. For this study the standard vapour tracer, q_v is used. This tracer has feedback on radiation and is not only transported but is also affected by the microphysics scheme. As in the previous section, ozone calculated with the Linoz scheme was used for feedback on the radiation scheme. The additional tendency by methane oxidation and photolysis is also included in the feedback simulation.

Figure 5.18 shows the latitude-height cross section of the seasonal zonal mean water vapour in ICON-ART (Top: control simulation and Middle: feedback simulation) and ERA-Interim at the bottom. In contrast to the figures shown before, the altitude range starts at 100 hPa instead of 1000 hPa. The region above 100 hPa represents the lower stratosphere region. In this region, the mechanism of upward transport or deep convection can nearly be neglected as a source of water vapour. Only methane oxidation contributes to the amount

of stratospheric water vapour significantly (e.g. Kley et al., 2000). Since the water vapour tendency by methane oxidation is missing in the control simulation, the seasonal and zonal mean shows large differences to the feedback simulation. The result of the feedback simulation is more comparable to the ERA-Interim zonal mean water vapour for all four seasons. In the ERA-Interim data, the process of methane oxidation is also taken into consideration.
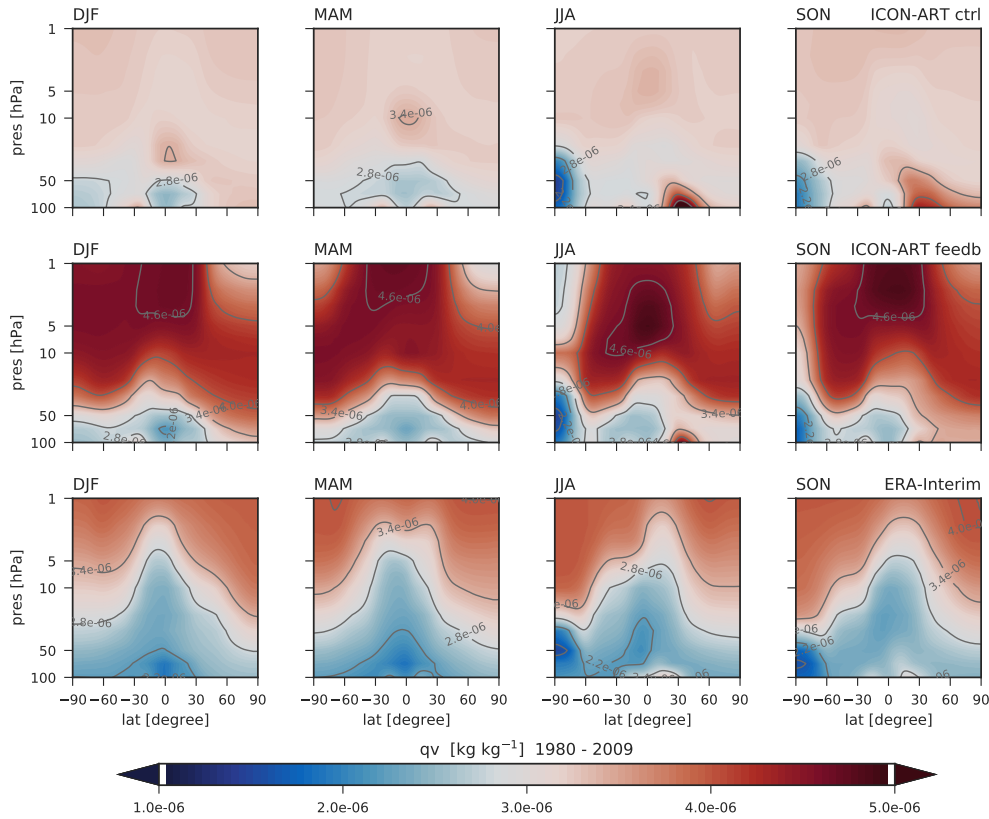
Figure 5.18: Latitude-height cross sections of seasonal and zonal mean water vapour $[\text{kg}\,\text{kg}^{-1}]$ for ICON-ART simulations and ERA-Interim from 1980 - 2009. Top: control run; Middle: feedback simulation; Bottom: ERA-Interim.

In the control simulation, values of $2.8 \times 10^{-6}\,\text{kg}\,\text{kg}^{-1}$ are only visible in the tropics below $50\,\text{hPa}$ between December and February. The spatial distribution in the feedback simulation below $50\,\text{hPa}$ is different in this season. From $50°N$ to $90°S$ values are below $2.8 \times 10^{-6}\,\text{kg}\,\text{kg}^{-1}$. For ERA-Interim this regime of low values for water vapour reaches up to $5\,\text{hPa}$ in the tropics. In comparison to ERA-Interim, values of water vapour are much too low for the ICON-ART control simulation. The difference is smallest in the tropics (below $0.4 \times 10^{-6}\,\text{kg}\,\text{kg}^{-1}$) but in the northern hemisphere, the difference is above $1\,\text{kg}\,\text{kg}^{-1}$. The feedback simulation shows values higher than the control simulation due to the methane oxidation tendencies on water vapour. For the northern hemisphere, the maximum is about $4.2 \times 10^{-6}\,\text{kg}\,\text{kg}^{-1}$. ERA-Interim shows values smaller than $4.0\,\text{kg}\,\text{kg}^{-1}$. Nevertheless, the stratospheric water vapour distribution in the feedback simulation of ICON-ART seems more

reasonable than the control simulation in comparison to ERA-Interim between December to February, as well as between March and May.

Whereas ERA-Interim shows a quasi symmetric zonal water vapour distribution around the equator for all four seasons, ICON-ART shows a slight asymmetry for both simulations. Minimum values of water vapour in the southern hemisphere from June to November below $2.0 \times 10^{-6} \, \mathrm{kg \, kg^{-1}}$ are represented by ICON-ART in agreement to ERA-Interim. The tropics as well as the northern hemisphere show again, values too low for the control simulation and slightly too high values for the feedback simulation.

However, the introduction of methane oxidation in the stratosphere as an important source of water vapour seems to be a reasonable step towards a more realistic representation of water vapour in the stratosphere. However, the absolute values of the ICON-ART feedback simulation seem to be too high. It could be possible, that the balance between H_2O and CH_4 is not preserved during the model simulation. Studies performed by e.g. Maycock et al. (2014), have shown that a water vapour increase of 2.0 ppm leads to cooling of the stratosphere of approximately $0.2 \, \mathrm{K \, dec^{-1}}$. The difference between the ICON-ART control simulation and feedback simulation is of the same order of magnitude, regarding the amount of water vapour above 50 hPa. Thus, temperature differences shown in section 5.3.2 are not only caused by altered ozone distribution, but also the impact of the chemical tendency of methane oxidation on water vapour.

5.3.5 Influences of water vapour and ozone on atmospheric dynamics

The previous sections have shown the close connection of thermodynamically induced changes in horizontal and vertical wind fields and the radiative impact of water vapour and ozone distributions. By the investigation of changes in stratospheric water vapour, zonal ozone, temperature and zonal wind distributions, a change in the global Brewer-Dobson Circulation is expected. In general, the inspection of different model simulations has shown that with the past changes in the chemical constitution, especially ozone and water vapour, a strengthening of the Brewer-Dobson Circulation is expected (Arblaster et al., 2014; Butchart, 2014). Since the Brewer-Dobson Circulation underlies a strong natural variability and the speed is not directly measurable, trends are hard to detect (Arblaster et al., 2014).

In the following two sections, two different methods are used to characterise changes in the atmospheric dynamics under changing ozone and water vapour distributions. The first method is the estimation of the tropical upward transport velocity by the water vapour tape recorder. The second one uses the concept of the simulated mean age of air.

5.3.6 Investigation of the tropical tape recorder

An atmospheric tape recorder can be defined as vertical propagation that varies periodically in time with a tropospheric source (Gregory and West, 2002). The temporal and vertical distribution of the tropical stratospheric water vapour is a prominent example for an atmospheric tape recorder signal. Water vapour in the tropics is transported upwards through the troposphere towards the tropopause (Schoeberl et al., 2012). The transport through the tropopause is caused by convective transport processes (e.g. Rosenlof and Reid, 2008). The simulated stratospheric water vapour depends strongly on the temperatures that are seen by an parcel of water vapour (Schoeberl et al., 2012). The concrete link between a variation of tropical tropopause temperatures over decades and the influence on the water vapour intake to the stratosphere is still not fully understood (e.g. Rosenlof and Reid, 2008).
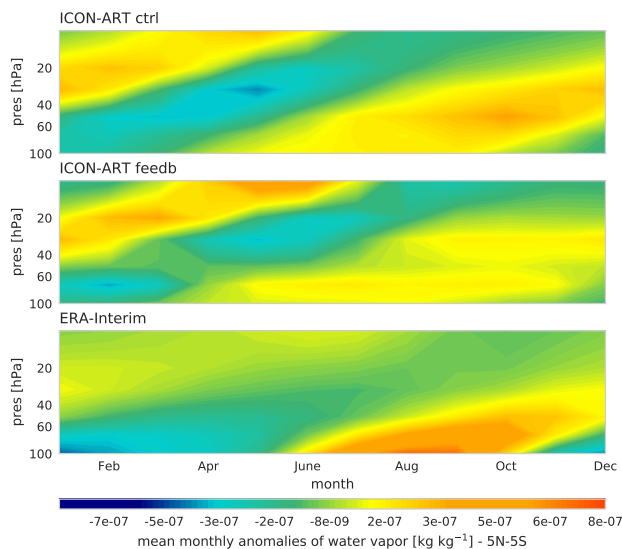
Figure 5.19: Tropical (5°N-5°S) water vapour anomalies as monthly mean deviations from the annual mean, averaged from 1980 to 2009, as a function of months and altitude.

The tape recorder is calculated from the annual mean anomalies of the respective water vapour tracer in the tropics ($5°N - 5°S$). Figure 5.19 shows the stratospheric tape recorder from 1980 to 2009. In this analysis, the year of initialisation (1979) is excluded. This reduces any possible spin up effects. To compare the ICON-ART results, we are using the water vapour product of ERA-Interim. The result of the calculated tape recorder of ERA-Interim is shown in the bottom panel of Figure 5.19.

As seen in Figure 5.19, the tape recorder signal for the ICON-ART control simulation shows lower values of anomalies down to $-5 \times 10^{-7}\,\mathrm{kg\,kg^{-1}}$ in comparison to the feedback simulation. For ERA-Interim, absolute values up to $-2 \times 10^{-7}\,\mathrm{kg\,kg^{-1}}$ can be observed from February to June in the pressure range of $100\,\mathrm{hPa}$ to $60\,\mathrm{hPa}$.

The anomalies in the feedback simulation show higher absolute values. The dry anomalies of the control simulation, between April and June, is decreased in the feedback simulation. On the other hand, the wet anomalies from June to December, between 60 hPa to 20 hPa, are also decreased in the feedback simulation. The analysis of the water vapour tape recorder detects less dry anomalies in the tropical stratosphere for the feedback simulation due to the additional source of water vapour by methane oxidation. Additionally, the analysis of the water vapour tape recorder fits to the results of the temperature difference, as seen in Figure 5.11. Due to lower tropical tropopause temperatures in the feedback simulation, less water can enter the lower stratosphere. This is caused, e.g. by dry freezing of water vapour. The radiative feedback of ozone is dominating the tropical transport processes. In general, monthly mean anomalies become much smaller in the feedback simulation compared to the experiment using the standard ozone climatology. The reduction of water vapour anomaly in the winter months leads to a more realistic representation of the mean annual tape recorder compared to ERA-Interim.

The slope following maximum anomalies seems to be nearly unaffected. Thus, the speed of the upward transport stays unaffected in the feedback simulation. The result of both ICON-ART simulations in comparison to ERA-Interim fits to the findings shown in Jiang et al. (2015). Here, the authors combined measurements and simulations of water vapour from the Microwave Limb Sounder (MLS), GMAO Modern-Era Retrospective Analysis for research and Applications in it's newest version (MERRA-2) and ERA-Interim and take them into comparison in the analysis of the water vapour tape recorder. The upward transport in the tropical tropopause of ERA-Interim is found to be up to 86 % faster than the transport diagnosed from MLS measurements. For higher altitudes, this discrepancy is increased.

5.3.7 Determining the velocity by analysis of the tape recorder signal

The shown tape recorder can be described by the concept of a time series, varying periodically in time, showing a vertical propagation in the tropics (Gregory and West, 2002). The deviations from the annual mean water vapour represent this time series x_i for each i discrete model layer. The time lag between the upward transported signal can be used to calculate the upward transport velocity. By using the method of the maximum cross correlation, where the cross correlation $\xi_i(\tau)$ is calculated by:

$$\xi_{i_1}(\tau) = \left(x_{i_1} \otimes x_{i_2} \right)(t) \tag{5.2}$$

$$\xi_{i_1}(\tau) = \int_{-\infty}^{\infty} x_{i_1}(t)^* x_{i_1}(t+\tau)\mathrm{d}t \tag{5.3}$$

with τ the time lag, t the time and x_{i_1} and x_{i_2} two tape recorder time series in two different model levels. For the analysis of the vertical upward transport velocity, the lag $\tau_{\max}$ for the maximum cross correlation is determined. By deviation of $\tau_{\max}$ by the altitude difference between both time series, the upward transport velocity ω_i is gained. The result for the ICON-ART control simulation is shown in Figure 5.20 in the left panel, as well as for ERA-Interim. The different values for different altitudes are binned, the mean of each bin is represented by the cross marker, as well as the standard deviation by the horizontal error bars.
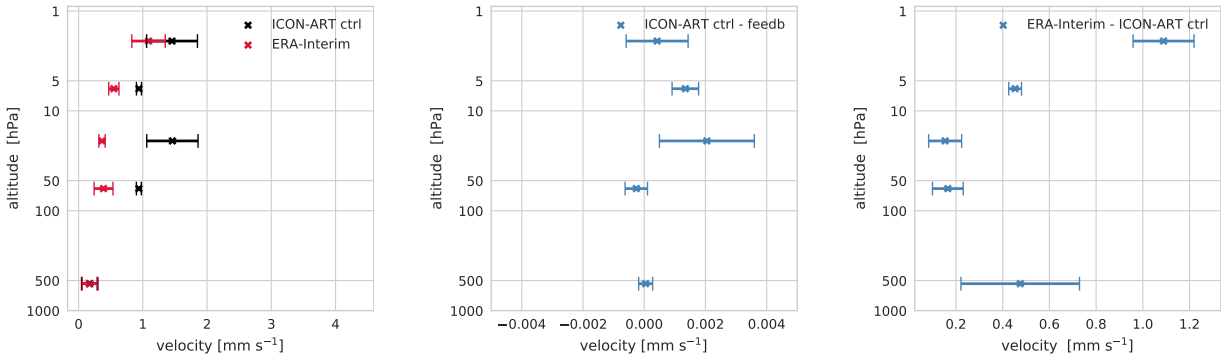
Figure 5.20: Estimated mean upward transport velocities based on water vapour tape recorder timeseries as a function of altitude. The most left panel shows the vertical profile for ICON-ART and ERA-Interim, the middle panel the difference between both ICON-ART simulations and the right panel the difference between ERA-Interim and ICON-ART. Error limits are indicated by horizontal bars, based on the standard deviation.

Below $100\,\text{hPa}$, the upward transport velocities of ERA-Interim and ICON-ART are comparable. The value of $\omega_{(1000,100]}$ is about $0.1\,\text{mm}\,\text{s}^{-1}$. The velocity of ICON-ART is higher than ERA-Interim between $100\,\text{hPa}$ to $1\,\text{hPa}$. This result matches the qualitative result of the investigation of the tropical tape recorder slope in the previous section. Compared to Seinfeld and Pandis (2006), the estimated upward transport velocity of $1\,\text{mm}\,\text{s}^{-1}$ in the stratosphere for ICON-ART is a sensible result. However, the study by e.g. Jiang et al. (2015) shows that recent observations show an even slower upward transport velocity compared to ERA-Interim. The discrepancy for the investigated years between 2005 and 2014 is up to $40\,\%$. In that context, the upward transport velocity in ICON-ART seems to be too fast. The differences between ERA-Interim and the ICON-ART control simulation are shown in the right panel of Figure 5.20.

By taking the feedback simulation into account, the estimated upward transport velocity becomes smaller than for the control simulation. The differences between both simulations are shown in the middle panel of Figure 5.20. The altered distribution of ozone and stratospheric water vapour clearly has an impact on the tropical upward transport velocity, estimated by the analysis of the water vapour tape recorder. Using the interactive ozone

and methane oxidation as a chemical tendency for water vapour, the transport is slowed down up to 13 m month^{-1}, which corresponds to a value of $0.005\,\mathrm{mm\,s^{-1}}$.

5.3.8 Changes in the mean age of air

The investigation of the simulated passive tracer of age of air in ICON-ART can give more information about stratospheric meridional transport processes. The diagnostic of age of air can be seen in this case study as an important tool to analyse the feedback processes of greenhouse gases on transport processes in the Earth's atmosphere. The tracer was initialised as described in section 3.2.8. The first eleven years of simulation are excluded in the analysis to prevent spin up effects.

The diagnostic of mean age of air in ICON-ART is depicted in Figure 5.21. With this diagnostic the general representation of stratospheric transport processes can be investigated.
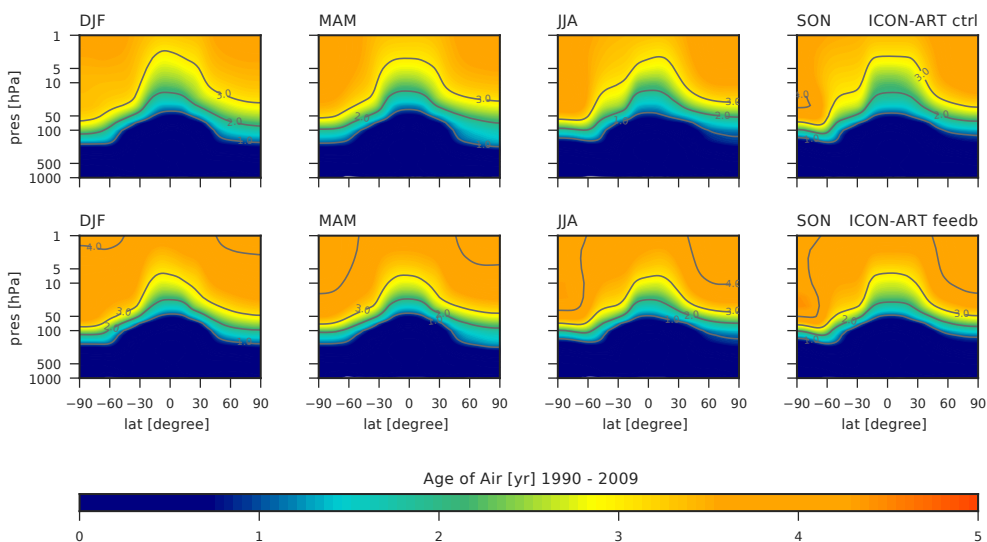
Figure 5.21: Latitude-height cross sections of seasonal and zonal mean age of air [years] for ICON-ART simulations 1990 - 2009. Top: control run; Bottom: feedback simulation.
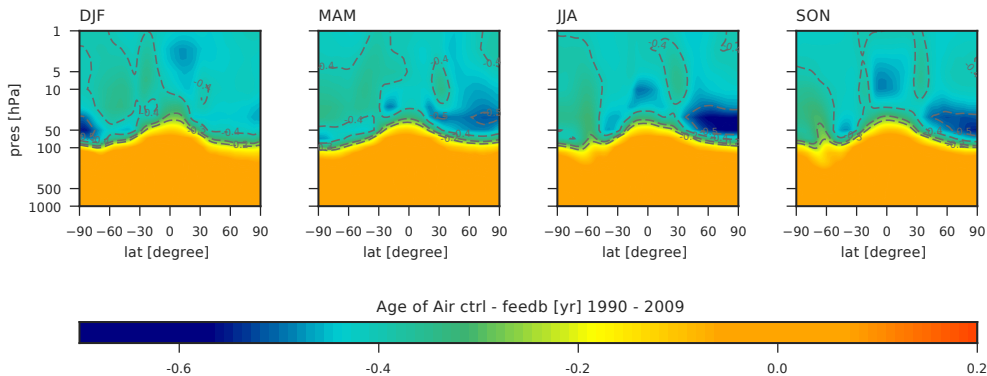
Figure 5.22: Latitude-height cross sections of seasonal and zonal mean age of air differences [years] between both ICON-ART simulations 1990 - 2009.

Due to upwelling transport processes in the tropics, the youngest air masses can be found there. The polar regions show the occurrence of older air masses up to an age of four years

in both simulations. The asymmetry between southern and northern hemisphere, induced by faster circulations in the southern hemisphere (e.g. Mahieu et al., 2014), is also well captured. The age of air is a diagnostic tool used to investigate and to evaluate transport times in the atmosphere against measurements. In comparison to other studies, which focus on other time spans (e.g. Brasseur and Solomon, 2006; Stiller et al., 2012), ICON-ART shows an age of air which is too young compared to observations. But this behaviour has also been observed in other studies with different models, as described in e.g. Monge-Sanz et al. (2007) or Hoppe et al. (2014). In general, it can be noted that ICON-ART shows good agreement to other model studies (e.g. Hoppe et al., 2014) and measurements (e.g. Engel et al., 2009; Haenel et al., 2015). The differences between control and feedback simulation are depicted in Figure 5.22. Between December and February, the zonal mean age of air in the feedback simulation is up to six month older. For the northern hemisphere the difference is slightly higher than for the southern hemisphere. However, the region of the southern hemisphere polar vortex shows the highest difference of eight months around $50\,\mathrm{hPa}$. This result matches the previous findings. Here, one can clearly see the impact of the interactive ozone on temperatures and thus on transport velocities. Between June and August, the inter hemispheric diversities between control and feedback simulations are higher in the northern hemisphere than in the southern hemisphere. Figure 5.23 shows the climatological mean age of air in the same representation as shown before. Here, the temporal and zonal mean of the age of air from 1990 to 2009 is taken at an altitude of $50\,\mathrm{hPa}$. The standard deviation from the mean is represented by the contour lines. These lines represent the inter-annual variability. The absolute mean age of air is higher for the feedback simulation on both hemispheres. The band of low values in the tropics is narrowed for the feedback simulation. The values of standard deviation are comparable. However, in the region of the southern hemisphere polar vortex, from October to January the standard deviation is higher for the feedback simulation. Since the polar vortex is stabilised by the ozone feedback, a different dynamical situation can be observed, influencing the inter annual variability of the age of air. The results at $50\,\mathrm{hPa}$ are in agreement for both hemispheres with e.g. Hoppe et al. (2014). In this study, the used model shows an age of air at $50\,\mathrm{hPa}$ which is of approximately 3.8 years in the southern hemisphere and 3.5 years at the northern hemisphere. As also seen in Figure 5.21, the age of air of both ICON-ART simulations is older than 4 years for high latitudes at both hemispheres at $50\,\mathrm{hPa}$ between July and November. As indicated by e.g. Hoppe et al. (2014), age of air determinations based on SF_6 measurements show an age of air of 4.5 ± 1 years at the southern hemisphere at $50\,\mathrm{hPa}$ and 3.8 ± 1 years at the northern hemisphere. MIPAS measurements reported by Stiller et al. (2012) and Haenel et al. (2015), show a higher age of air at $50\,\mathrm{hPa}$ on both hemispheres, more closely to 5 years. Since the interactive ICON-ART simulation shows an older age of
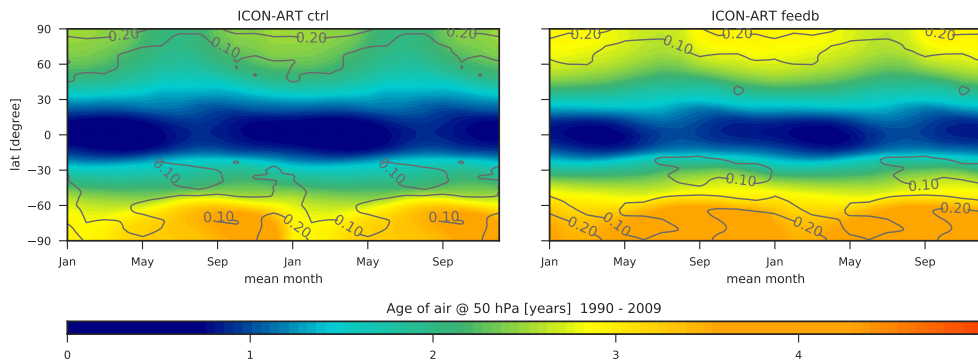
Figure 5.23: Monthly averaged zonal means of age of air at 50 hPa (shown twice) for the period from 1990 to 2009 (shaded). Contour lines represent the standard deviation of the monthly means. Left panel: age of air climatology in the control simulation; right panel: feedback simulation of ICON-ART.

air, it can be concluded that the implementation of the interactive ozone and water vapour calculation is an improvement for ICON-ART.

The climatological representation of Figure 5.23 shows more clearly, that the interactive ozone and water vapour do not only have an impact on the polar vortex stability but also influence the upward transport velocity in the tropics. Both effects in combination have the impact to alter the speed of the Brewer-Dobson circulation. In general, it can be concluded that the investigation of the tropical tape recorder and of the mean age of air shows consistent results. The impact of the altered ozone and water vapour distributions slows down the stratospheric overturning circulation.

5.4 Conclusions

By the investigation of both free running simulations, the feedback and control simulation, it can be seen how closely the atmospheric state variables, here temperature and wind are connected to the complex feedback process of the atmospheric composition. For the interactive (feedback) integration, ozone and water vapour is coupled to the radiation. First it was shown, by comparing both ICON-ART simulations, that the southern hemisphere polar vortex is stabilised for the feedback simulation. The temporal extend is up to two months longer for the feedback simulation than in the control simulation. The higher inter annual variability of the southern hemisphere ozone distribution seems to be more realistic than the ozone climatologies used in the control simulation. It has been stated by e.g. Arblaster et al. (2014) that an interactive calculation of ozone is preferable for next generation modelling systems. Changes in the atmospheric state variables are treated in a more consistent way, using an interactive calculation. However, the absolute values of ozone do not seem perfect compared to e.g. ERA-Interim. However, further investigating the atmospheric state, one can see that changes in water vapour and ozone in the interactive simulation induce reasonable changes in the zonal mean temperature distribution. The same holds for the zonal mean zonal wind and vertical wind. At this point it can be stated that ICON-ART has been successfully coupled to the climate physics configuration. Additionally, ICON-ART now offers an interactive ozone calculation and a more realistic calculation of stratospheric water vapour.

The control simulation shows values of stratospheric water vapour lower than values provided by ERA-Interim. The interactive ICON-ART simulation overcomes this dry bias. Changes in the stratospheric water vapour distribution, together with changes in the atmospheric ozone distribution, lead to changes in the stratospheric overturning circulation. The radiative impact of both chemical species lead to temperature changes resulting in changes in the atmospheric dynamics. To investigate those changes in more detail, the tropical water vapour tape recorder is investigated. The tape recorder investigation shows that the tropical upwelling is only weakly affected. However, changes in the upwelling are consistent to the findings before. The overturning circulation as measured by the Brewer-Dobson Circulation shows a northern hemisphere age increase, indicated by the age of air tracer of ICON-ART.

6 Interactive heating rate calculation

The absorption of incoming solar radiation does not only cause photodissociation of molecules but also has the ability to heat the Earth's atmosphere. The internal energy of a volume is increased if electromagnetic energy is absorbed. The thermal speed is also increased and consequently, the temperature within the volume rises. For the stratosphere, the shortwave absorption of ozone is one of the most important heat sources. The ozone absorption causes the temperature gradient inversion at the tropopause.

In a plane-parallel absorbing and scattering atmosphere, the heating rate $\frac{\partial T}{\partial t}$ at an altitude z is calculated by

$$\frac{\partial T}{\partial t} = -\frac{1}{C_{\mathrm{p}}\rho}\frac{\Delta F_\lambda(z)}{z} \tag{6.1}$$

with C_{p} the specific heat capacity at constant pressure, ρ the air density and F_λ the spectral flux. Here, $\Delta F_\lambda(z)$ is calculated by

$$\Delta F_\lambda(z) = F_\lambda(z) - F_\lambda(z + \Delta z) \tag{6.2}$$

where Δz is the differential thickness of the respective model layer.

Within the scope of this thesis, the model ICON-ART was extended by the ability to use a new model for heating rate calculations. This model is the same as used for photolysis rate calculations. In chapter 4, the validation of CloudJ in ICON-ART against air craft measurements is presented. The calculated heating rates by CloudJ can now be used to replace the ones provided by the standard radiation code PSRad. PSRad is based on the radiation code of RRTM, which is a basic two-stream model for solving the radiative transfer equation. Since CloudJ uses a more extensive approach of solving the radiative transfer equation, the heating rate calculation is more accurate (Hsu et al., 2017). Since CloudJ uses the same aerosol optical depths and gas optical depths, differences between PSRad and CloudJ are mainly caused by the method of solving the radiative transfer equation. The usage of the two-stream approach limits the heating rate calculation of PSRad to SZAs below 90°, whereas CloudJ provides sensible heating rate and photolysis rate calculation for SZA up to 94° (Hsu et al., 2017).

6.1 Construction of new heating rate profiles in ICON-ART

Figure 6.1 illustrates the separate short wave heating rate profiles on model levels. The profiles are selected from the global dataset at 105°W, 15°S, for a SZA of approximately 68°. The upper boundary of the CloudJ short wavelength bins is lower than of PSRad. Consequently, in the troposphere, from model level 47 to 35, the CloudJ profile shows a different shape than seen in the PSRad profile. For the model levels above, both shapes are
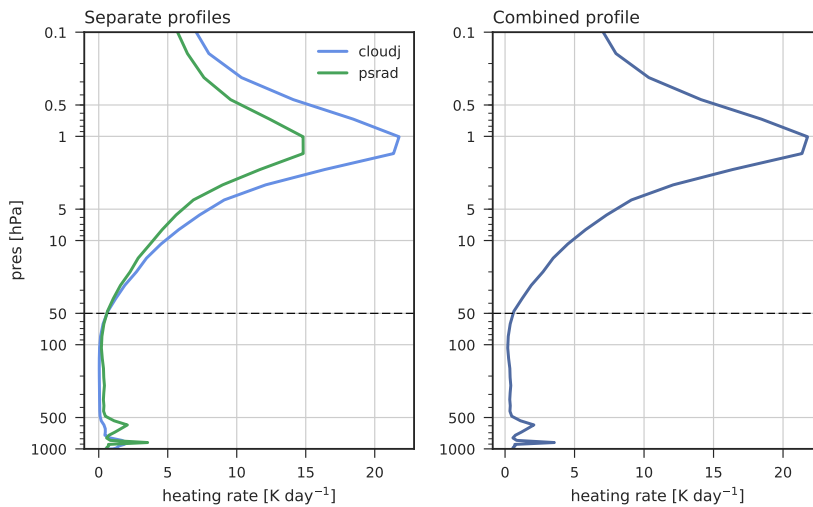
Figure 6.1: Profiles of short wave heating rate in ICON-ART with model levels on the y-axis. The left panel shows the heating rate calculated by PSRad and CloudJ separately. The right panel shows the resulting combined heating rate profile.

matching. Only the maximum value of CloudJ is of about $5\,\mathrm{K\,d^{-1}}$ higher than of PSRad. This difference corresponds to differences shown in Hsu et al. (2017). The new heating rate profile for ICON-ART is conducted by using the profile of PSRad for model levels 47 to 20 and of CloudJ for all levels above. The resulting profile is shown in the right panel of Figure 6.1. Figure 6.2 shows the monthly averaged zonal means of the short wave heating rates calculated by PSRad (left) in ICON-ART and CloudJ (right) in comparison at $50\,\mathrm{hPa}$. On both hemispheres, the different SZA dependence is clearly seen. Dark blue shaded areas indicate values of around $0\,\mathrm{K\,d^{-1}}$ at high SZA. Since PSRad only provides a reasonable heating rate calculation to an SZA of 90°, the duration of an absence of short wave heating is much longer than for the CloudJ simulation. For a decreasing SZA, starting in November at the southern hemisphere, a steep increase in the short wave heating rate for the CloudJ simulation can be observed. Whereas, the PSRad simulation shows a quite moderate increase. The absolute values around January are up to $0.5\,\mathrm{K\,d^{-1}}$ higher for the CloudJ simulation than for the standard PSRad simulation. In the northern hemisphere the difference in maximum values is less pronounced. In the tropics, short wave heating
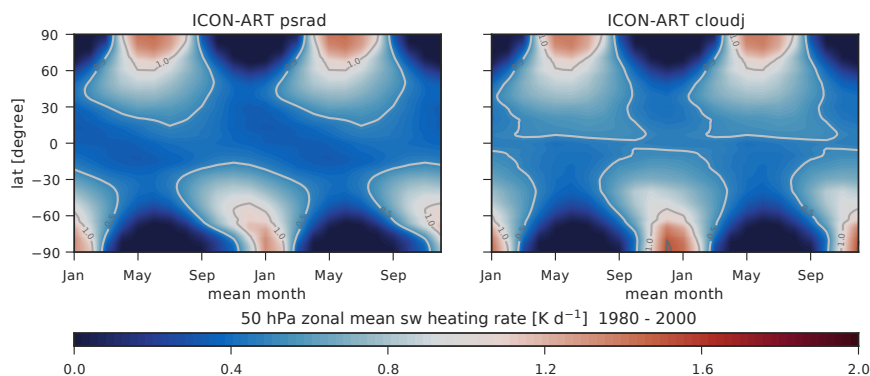
Figure 6.2: Monthly averaged zonal means of short wave heating rates $[K\,d^{-1}]$ at 50 hPa (shown twice) for the period from 1980 to 2000 (shaded). Left panel: Heating rates calculated by PSRad; right panel: Heating rates calculated by CloudJ.

rates around $0.6\,K\,d^{-1}$ occur in both simulations. The maximum tropical values seem to be higher in the CloudJ simulation than in the PSRad simulation. Since the differences are most prominent in the southern hemisphere, it can be concluded that the ozone distribution is altered due to different temperatures in the southern hemisphere polar vortex region.

For the following analysis, the feedback simulation of chapter 5 is used. Since this simulation uses the standard PSRad setup, this simulation is now called ICON-ART psrad. The second simulation uses the short wave heating rates, calculated with CloudJ. This simulation is called ICON-ART cloudj. Since the ICON-ART cloudj simulation shows a higher demand on computational time, due to the more advanced solution of the radiative-transfer-equation, the simulation is carried out from 1979 to 2000. All other parameters on the configuration are the same as described in chapter 5.

6.2 Changes in zonal mean temperature due to shortwave heating rates

As indicated by the findings of the previous section, temperatures in the region of the southern polar vortex seems to be lower in the simulation using short wave heating rates calculated by CloudJ instead of PSRad. Figure 6.3 shows the latitude-height cross sections of the seasonal and zonal mean temperature differences between both ICON-ART simulations and ERA-Interim. One simulation is called psrad, the other cloudj. The psrad simulation uses the interactive ozone and water vapour distributions like described in Section 5.1.2. The cloudj simulation uses also interactively calculated ozone and water vapour distribution using the same parameterisations as the psrad simulation. However, the distributions of water vapour and ozone are expected to differ between the psrad and cloudj simulation, if temperatures are changed due to altered short wave heating rates.
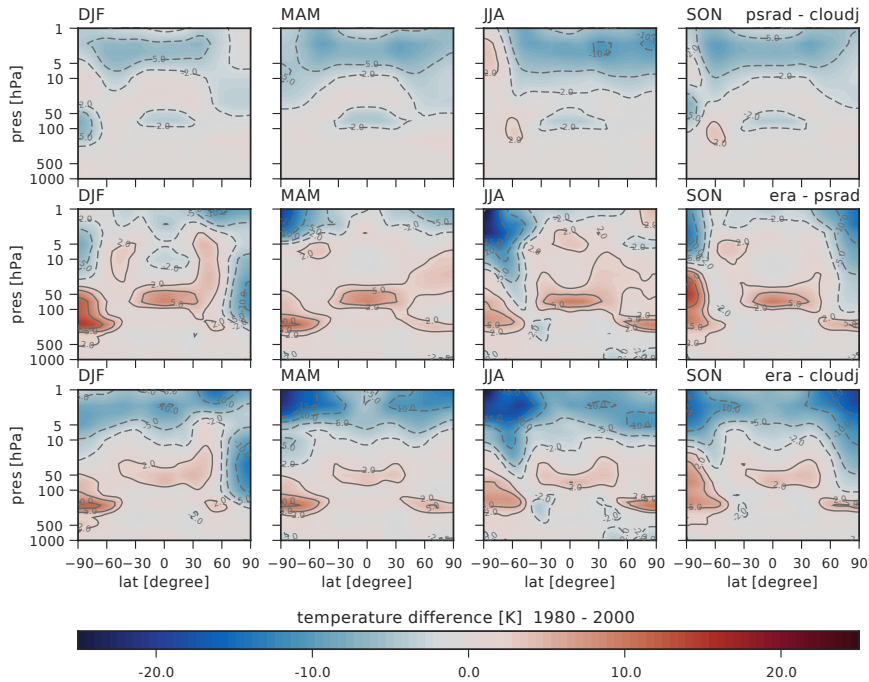
Figure 6.3: Latitude-height cross sections of seasonal and zonal mean temperature differences [K] for ICON-ART simulations and ERA-Interim from 1980 - 2000. Top: PSRad simulation minus CloudJ simulation ; Middle: ERA-Interim minus PSRad simulation; Bottom: ERA-Interim minus CloudJ simulation.

The top panel of Figure 6.3 shows the difference between the psrad and cloudj simulation. Here, the expected temperature difference in the southern hemisphere region between both simulations can be seen. As indicated by the investigation of the short wave heating rates of both simulations in the previous section, it is expected that the cloudj simulation shows higher temperatures between September and February. This is due to the fact that CloudJ provides a reasonable short wave heating rate calculation for higher SZA. The difference between 200 hPa to 30 hPa in the southern hemisphere is up to -5 K. The cloudj simulation shows a warmer southern hemisphere polar vortex region than the psrad simulation. In the tropics, a maximum difference of -2 K can be seen. This is probably caused by a changed water vapour distribution, induced by changed temperatures in the tropical tropopause region. Above 10 hPa between 60°S and 90°N, the cloudj simulation shows overall higher zonal and seasonal mean temperatures. This is also expected, since the cloudj simulation shows an enhanced profile of short wave heating rates as indicated in Section 6.1, Figure 6.1.

The middle and bottom panel show the difference of both simulations to ERA-Interim. By using short wave heating rates calculated with CloudJ in ICON-ART, the southern hemisphere and tropical tropopause discrepancies with ERA-Interim seasonal zonal mean temperatures are decreased. Between September and February, the psrad simulation is up to 10 K warmer compared to ERA-Interim in the southern hemisphere polar vortex

region. This difference is decreased in the cloudj simulation. Here only a difference of 5 K can be observed between ERA-Interim and the cloudj simulation. Also, the tropical tropopause temperatures seem to fit better for cloudj compared to ERA-Interim than the psrad simulation. Only the region above 10 hPa seems to be too warm in the psrad simulation compared to ERA-Interim. The differences reach a value of $-15\,\mathrm{K}$ in the southern hemisphere between June and August.

6.3 Differences in the meridional circulation by heating rate changes

Changes in the stratospheric meridional transport processes can be accessed, like shown in section 5.3.8 by investigation of the age of air tracer. Figure 6.4 shows the zonal and seasonal mean differences of the age of air tracer for both ICON-ART simulations. At this
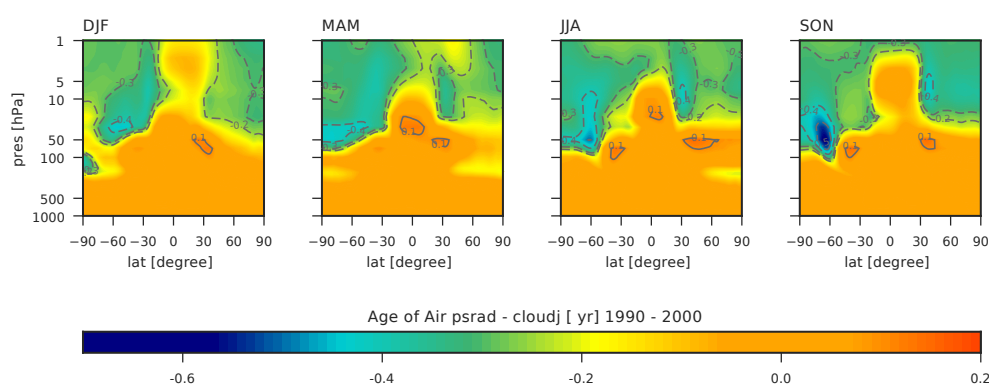
Figure 6.4: Latitude-height cross sections of seasonal and zonal mean age of air differences [years] between both ICON-ART simulations 1990 - 2000

point it is important to note that the color coding is slightly changed compared to the difference plot in section 5.3.8, Figure 5.22. Where as in Figure 5.22 only negative differences occurred, here also minor regions with a positive difference appear. The positive difference between the psrad simulation and cloudj simulation is approximately one and a half month in small regions between 100 hPa to 50 hPa in all four seasons. Here, the age of air of the psrad simulation is older than of the cloudj simulation. However, negative differences are dominating over all four seasons. Thus, the cloudj simulation shows a slower stratospheric meridional circulation than the psrad simulation. The age of air is between two and three months older between September and February in the cloudj simulations in the tropics from 1000 hPa to 1 hPa. Between March and August, this difference increases by one month for the upper regions between 5 hPa to 1 hPa. The highest difference can be found in the southern hemisphere between 100 hPa to 30 hPa. Here, the cloudj simulation shows values of age of air up to eight months older than the psrad simulation between September and

November. In those three months, also the climatological differences between both short wave heating rate distributions, shown in Figure 6.2, are high. Since cloudj is possible to simulate higher values of the SZA, heating rates are increasing much earlier in the southern hemisphere spring than in the psrad simulation. Temperatures rise earlier, also shown by Figure 6.3. This major difference in the temperature distribution seems to lead to a slower meridional stratospheric circulation in the model. The standard ICON-ART configuration shows an age of air which is too young compared to measurements (e.g. Brasseur and Solomon, 2006; Engel et al., 2009; Stiller et al., 2012; Haenel et al., 2015). In the feedback simulation, the polar vortex is stabilised by the ozone feedback and a different dynamical situation can be observed. The tropical upward transport is slowed down. Using the alternative heating rates by cloudj instead of psrad, the age of air decreases further. It can be concluded that the heating rate calculation with cloudj leads to a more realistic representation of the stratospheric meridional circulation in ICON-ART.

7 Summary and Outlook

Interactions between composition and meteorology are important for reliable models of the atmosphere. Climate change results from a small imbalance in the global energy balance. The interaction between the atmospheric composition and radiation determines the net effect of climate change, e.g. the change of near surface temperature. On average around $240\,\mathrm{W\,m^{-2}}$ of the incoming solar irradiance is absorbed at the surface. The current imbalance is estimated to be around $0.58 \pm 0.15\,\mathrm{W\,m^{-2}}$ for the years 2005–2010 (Hansen et al., 2011).

Radiative impact, circulation and chemistry are three processes that might occur on different temporal and spatial scales. The new modelling system ICON-ART allows to study the interaction between radiation and the atmospheric composition with two different physics configurations. For small spatial and temporal scales of days, the preferred configuration is the NWP (Numerical Weather Prediction) configuration, whereas the climate configuration is more suitable for projections of global change. A conceptual depiction of the interaction between the atmospheric composition, radiation, temperature as well as circulation is shown in Figure 7.1. Changes in the atmospheric composition induce changes in the radiative net flux (marked in orange). The atmospheric heating is defined by the convergence of the radiative net flux. Further, atmospheric temperature changes lead to a modification of
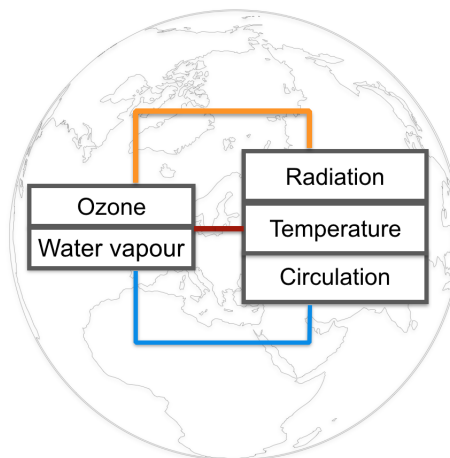
Figure 7.1: Schematic depiction of the interaction between the atmospheric composition and radiation. Processes of transport is marked in blue, radiative processes in orange and chemical processes in red.

the stratospheric overturning circulation. The circulation also influences the atmospheric composition by transport (marked in blue). Chemical reactions are temperature dependent (marked in red). All processes form a complex system with many feedbacks, which needs careful investigation.

In the framework of this thesis the ART component of the modelling system ICON-ART was substantially enhanced. The flexible tracer framework is the mandatory component for extensive chemical simulations in the future. Besides the linearised parameterisation of chemical tendencies, a full gas phase routine has been successfully included. The realistic simulation of atmospheric chemistry needs a reasonable calculation of photolysis rates. Within the scope of this thesis the photolysis module CloudJ (e.g. Wild et al., 2000; Bian and Prather, 2002) was added to ICON-ART and validated. The improved ICON-ART model was configured to perform a range of model integrations with both physics configurations to validate the system and to characterise climate sensitivities.

In most climate and NWP models, many simplifications and approximations are made in the development of a suitable radiation model with low computational cost (e.g. Wild et al., 2000; Bian and Prather, 2002; Arblaster et al., 2014). However, the consistent treatment of actinic flux and net flux calculations are preferable. The actinic flux is defined as the radiant flux density incident onto a spherical unit area (Ruggaber et al., 1993) and is used for photolysis rate calculation.

Many previous studies emphasised the radiative impact of clouds in the atmosphere (e.g. van Weele and Duynkerke, 1993; Kley et al., 2000; Tie et al., 2003; Liu et al., 2006). Nevertheless, studies of the absolute values of the relative differences of the actinic flux between the cloud free and cloudy atmosphere are rare. With ICON-ART it is now possible to quantify the impact of clouds on the actinic flux and thus on photolysis rates. The calculation of the actinic flux in a scattering atmosphere, due to the presence of clouds can be calculated using the ICON-ART model with the CloudJ module. The simulations with ICON-ART show that the enhancement effect on photolysis rates due to cloud presence is between 20 % to 80 % for the co-located comparison. Compared to the values given by Tie et al. (2003) and Liu et al. (2006) of 13 % to 62 % for an photolysis rate enhancement, ICON-ART shows higher values. Neglecting the temporal co-location between the clear sky and cloudy sky datapoints, an enhancement between 10 % to 25 % can also be seen. Relative differences are higher for the co-located case too. The non co-located analysis corresponds to the finding of Tie et al. (2003). Here, a global average is taken into account, leading to a 13 % photolysis rate enhancement.

For the first time ICON-ART simulations in climate configuration were performed, for a simulation timespan from 1979 to 2009. To investigate composition-climate interactions a parameterised stratospheric ozone chemistry was included, a methane oxidation scheme and a diagnostic tracer, the so-called age of air. In the non-interactive case ozone is

prescribed. In the interactive case ozone is calculated and the calculated ozone is used in the radiation scheme of ICON-ART. The decadal non-interactive and interactive integrations are compared with each other and with ERA-Interim. In the interactive simulation, the ozone hole season is extended, the tropical upwelling is only weakly affected and the overturning circulation as measured by the Brewer-Dobson Circulation shows a slowing down. This can also be seen by the investigation of the age of air.

Most importantly, the zonal asymmetry of the interactive ozone manifest itself in climatic relevant temperature and circulation changes. The importance of the successful representation of this asymmetry in modelling systems is also under current discussion (e.g Dennison et al., 2017).

As an outlook, the possibility of consistent heating rate and photolysis rate calculations in ICON-ART is discussed. Heating rates can be calculated with the validated module for actinic fluxes, CloudJ. The replacement of the default shortwave heating rates was implemented. Now it is possible to use the shortwave heating rates, calculated with CloudJ for climate integrations with ICON-ART. The consistent heating rate calculation provides a reasonable thermal structure in the UTLS. The investigation of the age of air implicates a good representation of the overturning circulation. Further investigation is required to assess all possible benefits and issues for this model configuration.

The studies of this thesis show for the first time the applicability of ICON-ART for climate integrations. In the future, not only the consistent treatment of photolysis rates and shortwave heating rate calculations will become an essential part of chemistry climate modelling but also decadal and seasonal forecasts will benefit from improvements based on the investigations and validation shown in this thesis. All technical improvements are described (in detail) in Schröter et al. (2018).

This configuration of ICON-ART is now ready to be used for studies on aspects of climate sensitivity and radiative forcing. The concept of radiative forcing can be understood as the measure of the radiative imbalance (e.g. IPCC, 2007). More precisely, the radiative forcing is defined as the linear gradient of the temperature caused by solar irradiance, altered by changes in the atmospheric composition (e.g. Shine et al., 2003). A large variety of studies focused on the discussion of the radiative forcing by different chemical species or aerosols (e.g. Shine et al., 2003; Gregory et al., 2004). Studies on climate sensitivity as well as radiative forcing need computational expensive sensitivity studies with global chemistry-climate models (e.g. Nowack et al., 2014). ICON-ART is well suited for such integrations, because it scales well. It is designed for modern massive parallel computing systems. Studies on radiative forcing and climate sensitivity will be performed with ICON-ART in the future. Due to the nesting technique, ICON-ART shows advantages for supporting future aircraft campaign studies. The developments shown in the scope of this thesis suite the demands of a large variety of different applications ranging from NWP to climate integrations.

8 Bibliography

Extensible Markup Language (XML) 1.0 (Fifth Edition), `https://www.w3.org/TR/2008/REC-xml-20081126/`, accessed: 2017-07-27.

U.S. standard atmosphere, 1976, United States Committee on Extension to the Standard Atmosphere National Oceanic and Atmospheric Administration : for sale by the Supt. of Docs., U.S. Govt. Print. Off., 1976.

Abramowitz, M., Stegun, I. A., et al.: Handbook of mathematical functions with formulas, graphs, and mathematical tables, Vol. 9, Dover, New York, 1972.

Arblaster, J., Gillett, N., N. Calvo, P. F., L.M. Polvani, S.-W. S., Waugh, D., and Young, P.: Stratospheric ozone changes and climate, Chapter 4 in Scientific Assessment of Ozone Depletion: 2014, Global Ozone Research and Monitoring Project – Report No. 55, World Meteorological Organization, Geneva, Switzerland, 2014.

Bentley, J. L.: Multidimensional Binary Search Trees Used for Associative Searching, Commun. ACM, 18, 509–517, doi:10.1145/361002.361007, 1975.

Bey, I., Jacob, D. J., Yantosca, R. M., Logan, J. A., Field, B. D., Fiore, A. M., Li, Q., Liu, H. Y., Mickley, L. J., and Schultz, M. G.: Global modeling of tropospheric chemistry with assimilated meteorology: Model description and evaluation, Journal of Geophysical Research: Atmospheres, 106, 23 073–23 095, doi:10.1029/2001JD000807, 2001.

Bian, H. and Prather, M.: Fast-J2: Accurate Simulation of Stratospheric Photolysis in Global Chemical Models, Journal of Atmospheric Chemistry, 41, 281–296, doi:10.1023/A:1014980619462, 2002.

Bithell, M., Gray, L. J., Harries, J. E., III, J. M. R., and Tuck, A. F.: Synoptic Interpretation of Measurements from HALOE, Journal of the Atmospheric Sciences, 51, 2942–2956, doi:10.1175/1520-0469(1994)051<2942:SIOMFH>2.0.CO;2, 1994.

Bohn, B., Corlett, G. K., Gillmann, M., Sanghavi, S., Stange, G., Tensing, E., Vrekoussis, M., Bloss, W. J., Clapp, L. J., Kortner, M., Dorn, H.-P., Monks, P. S., Platt, U., Plass-Dülmer, C., Mihalopoulos, N., Heard, D. E., Clemitshaw, K. C., Meixner, F. X., Prevot, A. S. H., and Schmitt, R.: Photolysis frequency measurement techniques: results

of a comparison within the ACCENT project, Atmospheric Chemistry and Physics, 8, 5373–5391, doi:10.5194/acp-8-5373-2008, 2008.

Bönisch, H., Engel, A., Birner, T., Hoor, P., Tarasick, D. W., and Ray, E. A.: On the structural changes in the Brewer-Dobson circulation after 2000, Atmospheric Chemistry and Physics, 11, 3937–3948, doi:10.5194/acp-11-3937-2011, 2011.

Braesicke, P., Hurwitz, M. M., and Pyle, J. A.: The stratospheric response to changes in ozone and carbon dioxide as modelled with a GCM including parameterised ozone chemistry, Meteorologische Zeitschrift, 15, 343–354, doi:10.1127/0941-2948/2006/0124, 2006.

Braesicke, P., Keeble, J., Yang, X., Stiller, G., Kellmann, S., Abraham, N. L., Archibald, A., Telford, P., and Pyle, J. A.: Circulation anomalies in the Southern Hemisphere and ozone changes, Atmospheric Chemistry and Physics, 13, 10 677–10 688, doi:10.5194/acp-13-10677-2013, 2013.

Brasseur, G. P. and Solomon, S.: Aeronomy of the middle atmosphere: Chemistry and physics of the stratosphere and mesosphere, Vol. 32, Springer Science & Business Media, 2006.

Brasseur, G. P., Hauglustaine, D. A., Walters, S., Rasch, P. J., Müller, J.-F., Granier, C., and Tie, X. X.: MOZART, a global chemical transport model for ozone and related chemical tracers: 1. Model description, Journal of Geophysical Research: Atmospheres, 103, 28 265–28 289, doi:10.1029/98JD02397, 1998.

Briegleb, B. P.: Delta-Eddington approximation for solar radiation in the NCAR community climate model, Journal of Geophysical Research: Atmospheres, 97, 7603–7612, doi:10.1029/92JD00291, 1992.

Butchart, N.: The Brewer-Dobson circulation, Reviews of Geophysics, 52, 157–184, doi:10.1002/2013RG000448, 2014.

Chandrasekhar, S.: Radiative Transfer, Dover Books on Intermediate and Advanced Mathematics, Dover Publications, 1960.

Cionni, I., Eyring, V., Lamarque, J. F., Randel, W. J., Stevenson, D. S., Wu, F., Bodeker, G. E., Shepherd, T. G., Shindell, D. T., and Waugh, D. W.: Ozone database in support of CMIP5 simulations: results and corresponding radiative forcing, Atmospheric Chemistry and Physics, 11, 11 267–11 292, doi:10.5194/acp-11-11267-2011, 2011.

Crook, J. A., Gillett, N. P., and Keeley, S. P. E.: Sensitivity of Southern Hemisphere climate to zonal asymmetry in ozone, Geophysical Research Letters, 35, doi:10.1029/2007GL032698, l07806, 2008.

de Forster, P. M. and Shine, K. P.: Stratospheric water vapour changes as a possible contributor to observed stratospheric cooling, Geophysical Research Letters, 26, 3309–3312, doi:10.1029/1999GL010487, 1999.

Dee, D. P., Uppala, S. M., Simmons, A. J., Berrisford, P., Poli, P., Kobayashi, S., Andrae, U., Balmaseda, M. A., Balsamo, G., Bauer, P., Bechtold, P., Beljaars, A. C. M., van de Berg, L., Bidlot, J., Bormann, N., Delsol, C., Dragani, R., Fuentes, M., Geer, A. J., Haimberger, L., Healy, S. B., Hersbach, H., Hólm, E. V., Isaksen, L., Kållberg, P., Köhler, M., Matricardi, M., McNally, A. P., Monge-Sanz, B. M., Morcrette, J.-J., Park, B.-K., Peubey, C., de Rosnay, P., Tavolato, C., Thépaut, J.-N., and Vitart, F.: The ERA-Interim reanalysis: configuration and performance of the data assimilation system, Quarterly Journal of the Royal Meteorological Society, 137, 553–597, doi:10.1002/qj.828, 2011.

DeMore, W., Howard, C., Sander, S., Ravishankara, A., Golden, D., Kolb, C., Hampson, R., Molina, M., and Kurylo, M.: Chemical Kinetics and Photochemical Data for Use in Stratospheric Modeling, 1997.

Dennison, F., McDonald, A., and Morgenstern, O.: The evolution of zonally asymmetric austral ozone in a chemistry–climate model, Atmospheric Chemistry and Physics, 17, 14 075–14 084, doi:10.5194/acp-17-14075-2017, 2017.

Dethof, A.: Aspects of modelling and assimilation for the stratosphere at ECMWF, SPARC Newsletter, 21, 250, 2003.

Diekmann, C.: Simulation der polaren UT/LS im Winter 2015/16 mit ICON-ART, 2017.

Dörnbrack, A.: Atmospheric Physics: Background – Methods – Trends, Chap. The Atmosphere: Vast, Shallow, and Full of Subtleties, 3–16, Springer Berlin Heidelberg, Berlin, Heidelberg, doi:10.1007/978-3-642-30183-4_1, 2012.

Eckstein, J.: Atmospheric models and aircraft measurements : representativeness and model validation, 2017.

Eckstein, J., Ruhnke, R., Pfahl, S., Christner, E., Dyroff, C., Reinert, D., Rieger, D., Schneider, M., Schröter, J., Zahn, A., and Braesicke, P.: From climatological to small scale applications: Simulating water isotopologues with ICON-ART-Iso (version 2.1), Geoscientific Model Development Discussions, 2017, 1–31, doi:10.5194/gmd-2017-280, 2017.

Emmons, L. K., Walters, S., Hess, P. G., Lamarque, J.-F., Pfister, G. G., Fillmore, D., Granier, C., Guenther, A., Kinnison, D., Laepple, T., Orlando, J., Tie, X., Tyndall, G., Wiedinmyer, C., Baughcum, S. L., and Kloster, S.: Description and evaluation of the

Model for Ozone and Related chemical Tracers, version 4 (MOZART-4), Geoscientific Model Development, 3, 43–67, doi:10.5194/gmd-3-43-2010, 2010.

Engel, A., Mobius, T., Bonisch, H., Schmidt, U., Heinz, R., Levin, I., Atlas, E., Aoki, S., Nakazawa, T., Sugawara, S., Moore, F., Hurst, D., Elkins, J., Schauffler, S., Andrews, A., and Boering, K.: Age of stratospheric air unchanged within uncertainties over the past 30 years, Nature Geosci, 2, 28–31, 2009.

Erle, F., Pfeilsticker, K., and Platt, U.: On the influence of tropospheric clouds on zenith-scattered-light measurements of stratospheric species, Geophysical Research Letters, 22, 2725–2728, doi:10.1029/95GL02789, 1995.

Eyring, V., Butchart, N., Waugh, D. W., Akiyoshi, H., Austin, J., Bekki, S., Bodeker, G. E., Boville, B. A., Brühl, C., Chipperfield, M. P., Cordero, E., Dameris, M., Deushi, M., Fioletov, V. E., Frith, S. M., Garcia, R. R., Gettelman, A., Giorgetta, M. A., Grewe, V., Jourdain, L., Kinnison, D. E., Mancini, E., Manzini, E., Marchand, M., Marsh, D. R., Nagashima, T., Newman, P. A., Nielsen, J. E., Pawson, S., Pitari, G., Plummer, D. A., Rozanov, E., Schraner, M., Shepherd, T. G., Shibata, K., Stolarski, R. S., Struthers, H., Tian, W., and Yoshiki, M.: Assessment of temperature, trace species, and ozone in chemistry-climate model simulations of the recent past, Journal of Geophysical Research: Atmospheres, 111, doi:10.1029/2006JD007327, d22308, 2006.

Feng, Y., Penner, J. E., Sillman, S., and Liu, X.: Effects of cloud overlap in photochemical models, Journal of Geophysical Research: Atmospheres, 109, doi:10.1029/2003JD004040, d04310, 2004.

Forster, P. M., Fomichev, V. I., Rozanov, E., Cagnazzo, C., Jonsson, A. I., Langematz, U., Fomin, B., Iacono, M. J., Mayer, B., Mlawer, E., Myhre, G., Portmann, R. W., Akiyoshi, H., Falaleeva, V., Gillett, N., Karpechko, A., Li, J., Lemennais, P., Morgenstern, O., Oberländer, S., Sigmond, M., and Shibata, K.: Evaluation of radiation scheme performance within chemistry climate models, Journal of Geophysical Research: Atmospheres, 116, doi:10.1029/2010JD015361, d10302, 2011.

Fueglistaler, S., Bonazzola, M., Haynes, P. H., and Peter, T.: Stratospheric water vapor predicted from the Lagrangian temperature history of air entering the stratosphere in the tropics, Journal of Geophysical Research: Atmospheres, 110, doi:10.1029/2004JD005516, d08107, 2005.

Fueglistaler, S., Dessler, A. E., Dunkerton, T. J., Folkins, I., Fu, Q., and Mote, P. W.: Tropical tropopause layer, Reviews of Geophysics, 47, doi:10.1029/2008RG000267, rG1004, 2009.

Gassmann, A. and Herzog, H.-J.: Towards a consistent numerical compressible non-hydrostatic model using generalized Hamiltonian tools, Quarterly Journal of the Royal Meteorological Society, 134, 1597–1613, doi:10.1002/qj.297, 2008.

Gates, W. L., Boyle, J. S., Covey, C., Dease, C. G., Doutriaux, C. M., Drach, R. S., Fiorino, M., Gleckler, P. J., Hnilo, J. J., Marlais, S. M., Phillips, T. J., Potter, G. L., Santer, B. D., Sperber, K. R., Taylor, K. E., and Williams, D. N.: An Overview of the Results of the Atmospheric Model Intercomparison Project (AMIP I), Bulletin of the American Meteorological Society, 80, 29–55, doi:10.1175/1520-0477(1999)080<0029:AOOTRO>2.0.CO;2, 1999.

Gerber, E. P. and Manzini, E.: The Dynamics and Variability Model Intercomparison Project (DynVarMIP) for CMIP6: assessing the stratosphere–troposphere system, Geoscientific Model Development, 9, 3413–3425, doi:10.5194/gmd-9-3413-2016, 2016.

Gettelman, A., Hegglin, M. I., Son, S.-W., Kim, J., Fujiwara, M., Birner, T., Kremser, S., Rex, M., Añel, J. A., Akiyoshi, H., Austin, J., Bekki, S., Braesike, P., Brühl, C., Butchart, N., Chipperfield, M., Dameris, M., Dhomse, S., Garny, H., Hardiman, S. C., Jöckel, P., Kinnison, D. E., Lamarque, J. F., Mancini, E., Marchand, M., Michou, M., Morgenstern, O., Pawson, S., Pitari, G., Plummer, D., Pyle, J. A., Rozanov, E., Scinocca, J., Shepherd, T. G., Shibata, K., Smale, D., Teyssèdre, H., and Tian, W.: Multimodel assessment of the upper troposphere and lower stratosphere: Tropics and global trends, Journal of Geophysical Research: Atmospheres, 115, doi:10.1029/2009JD013638, d00M08, 2010.

Gregory, A. R. and West, V.: The sensitivity of a model's stratospheric tape recorder to the choice of advection scheme, Quarterly Journal of the Royal Meteorological Society, 128, 1827–1846, doi:10.1256/003590002320603430, 2002.

Gregory, J. M., Ingram, W. J., Palmer, M. A., Jones, G. S., Stott, P. A., Thorpe, R. B., Lowe, J. A., Johns, T. C., and Williams, K. D.: A new method for diagnosing radiative forcing and climate sensitivity, Geophysical Research Letters, 31, doi:10.1029/2003GL018747, l03205, 2004.

Haenel, F. J., Stiller, G. P., von Clarmann, T., Funke, B., Eckert, E., Glatthor, N., Grabowski, U., Kellmann, S., Kiefer, M., Linden, A., and Reddmann, T.: Reassessment of MIPAS age of air trends and variability, Atmospheric Chemistry and Physics, 15, 13 161–13 176, doi:10.5194/acp-15-13161-2015, 2015.

Hansen, J., Ruedy, R., Sato, M., and Lo, K.: GLOBAL SURFACE TEMPERATURE CHANGE, Reviews of Geophysics, 48, doi:10.1029/2010RG000345, rG4004, 2010.

Hansen, J., Sato, M., Kharecha, P., and von Schuckmann, K.: Earth's energy imbalance and implications, Atmospheric Chemistry and Physics, 11, 13 421–13 449, doi:10.5194/acp-11-13421-2011, 2011.

Hassler, B., Young, P. J., Portmann, R. W., Bodeker, G. E., Daniel, J. S., Rosenlof, K. H., and Solomon, S.: Comparison of three vertically resolved ozone data sets: climatology, trends and radiative forcings, Atmospheric Chemistry and Physics, 13, 5533–5550, doi:10.5194/acp-13-5533-2013, 2013.

Hollingsworth, A., Engelen, R., Textor, C., Benedetti, A., Boucher, O., Chevallier, F., Dethof, A., Elbern, H., Eskes, H., Flemming, J., et al.: The Global Earth-system Monitoring using Satellite and in-situ data (GEMS) Project: Towards a monitoring and forecasting system for atmospheric composition, Am. Meteorol. Soc, 89, 1147–1164, 2008.

Holton, J. and Hakim, G.: An Introduction to Dynamic Meteorology, Academic Press, Elsevier, 2013.

Hoppe, C. M., Hoffmann, L., Konopka, P., Grooß, J.-U., Ploeger, F., Günther, G., Jöckel, P., and Müller, R.: The implementation of the CLaMS Lagrangian transport core into the chemistry climate model EMAC 2.40.1: application on age of air and transport of long-lived trace species, Geoscientific Model Development, 7, 2639–2651, doi:10.5194/gmd-7-2639-2014, 2014.

Hsu, J., Prather, M. J., Cameron-Smith, P., Veidenbaum, A., and Nicolau, A.: A radiative transfer module for calculating photolysis rates and solar heating in climate models: Solar-J v7.5, Geoscientific Model Development, 10, 2525–2545, doi:10.5194/gmd-10-2525-2017, 2017.

Iacono, M. J., Delamere, J. S., Mlawer, E. J., Shephard, M. W., Clough, S. A., and Collins, W. D.: Radiative forcing by long-lived greenhouse gases: Calculations with the AER radiative transfer models, Journal of Geophysical Research: Atmospheres, 113, doi:10.1029/2008JD009944, d13103, 2008.

IPCC: Climate Change 2007: The Physical Science Basis. Contribution of Working Group I to the Fourth Assessment Report of the Intergovernmental Panel on Climate Change, Cambridge University Press, Cambridge, United Kingdom and New York, NY, USA, 2007.

IPCC: Climate Change 2013: The Physical Science Basis. Contribution of Working Group I to the Fifth Assessment Report of the Intergovernmental Panel on Climate Change, Cambridge University Press, Cambridge, United Kingdom and New York, NY, USA, doi:10.1017/CBO9781107415324, 2013.

Jacob, D.: Introduction to atmospheric chemistry, Princeton University Press, 1999.

Jacob, D. J., Gottlieb, E. W., and Prather, M. J.: Chemistry of a polluted cloudy boundary layer, Journal of Geophysical Research: Atmospheres, 94, 12 975–13 002, doi:10.1029/ JD094iD10p12975, 1989.

Jiang, J. H., Su, H., Zhai, C., Wu, L., Minschwaner, K., Molod, A. M., and Tompkins, A. M.: An assessment of upper troposphere and lower stratosphere water vapor in MERRA, MERRA2, and ECMWF reanalyses using Aura MLS observations, Journal of Geophysical Research: Atmospheres, 120, 11 468–11 485, doi:10.1002/2015JD023752, 2015.

Jöckel, P., Sander, R., Kerkweg, A., Tost, H., and Lelieveld, J.: Technical Note: The Modular Earth Submodel System (MESSy) - a new approach towards Earth System Modeling, Atmospheric Chemistry and Physics, 5, 433–444, doi:10.5194/acp-5-433-2005, 2005.

Kato, S., Xu, K.-M., Wong, T., Loeb, N. G., Rose, F. G., Trenberth, K. E., and Thorsen, T. J.: Investigation of the Residual in Column-Integrated Atmospheric Energy Balance Using Cloud Objects, Journal of Climate, 29, 7435–7452, doi:10.1175/JCLI-D-15-0782.1, 2016.

Keeble, J., Braesicke, P., Abraham, N. L., Roscoe, H. K., and Pyle, J. A.: The impact of polar stratospheric ozone loss on Southern Hemisphere stratospheric circulation and climate, Atmospheric Chemistry and Physics, 14, 13 705–13 717, doi:10.5194/acp-14-13705-2014, 2014.

Kiel, M.: Trace gas measurements from different spectral regions using FTIR spectroscopy, 2016.

Kley, D., III, J. M. R., and Phillips, C.: SPARC assessment of upper tropospheric and stratospheric water vapour, World Clim. Res. Program, SPARC Rep. 2, WMO/TD 1043, WCRP Rep. 113, Geneva, Switzerland, 2000.

Konopka, P., Grooß, J.-U., Hoppel, K. W., Steinhorst, H.-M., and Müller, R.: Mixing and Chemical Ozone Loss during and after the Antarctic Polar Vortex Major Warming in September 2002, Journal of the Atmospheric Sciences, 62, 848–859, doi:10.1175/JAS-3329.1, 2005.

Landgraf, J. and Crutzen, P.: An efficient method for online calculations of photolysis and heating rates, Journal of the atmospheric sciences, 55, 863–878, 1998.

Lary, D. and Pyle, J.: Diffuse radiation, twilight, and photochemistry, Journal of atmospheric chemistry, 13, 373–392, 1991.

Lean, J., Rottman, G., Harder, J., and Kopp, G.: SORCE Contributions to New Understanding of Global Change and Solar Variability, Solar Physics, 230, 27–53, doi:10.1007/s11207-005-1527-2, 2005.

Leuenberger, D., Koller, M., Fuhrer, O., and Schär, C.: A Generalization of the SLEVE Vertical Coordinate, Monthly Weather Review, 138, 3683–3689, doi:10.1175/2010MWR3307.1, 2010.

Lin, P. and Fu, Q.: Changes in various branches of the Brewer–Dobson circulation from an ensemble of chemistry climate models, Journal of Geophysical Research: Atmospheres, 118, 73–84, doi:10.1029/2012JD018813, 2013.

Liou, K.: An Introduction to Atmospheric Radiation, International Geophysics, Elsevier Science, 2002.

Liu, H., Crawford, J. H., Pierce, R. B., Norris, P., Platnick, S. E., Chen, G., Logan, J. A., Yantosca, R. M., Evans, M. J., Kittaka, C., Feng, Y., and Tie, X.: Radiative effect of clouds on tropospheric chemistry in a global three-dimensional chemical transport model, Journal of Geophysical Research: Atmospheres, 111, doi:10.1029/2005JD006403, d20303, 2006.

Liu, H., Crawford, J. H., Considine, D. B., Platnick, S., Norris, P. M., Duncan, B. N., Pierce, R. B., Chen, G., and Yantosca, R. M.: Sensitivity of photolysis frequencies and key tropospheric oxidants in a global model to cloud vertical distributions and optical properties, Journal of Geophysical Research: Atmospheres, 114, doi:10.1029/2008JD011503, d10305, 2009.

Liu, Y. S., Fueglistaler, S., and Haynes, P. H.: Advection-condensation paradigm for stratospheric water vapor, Journal of Geophysical Research: Atmospheres, 115, doi:10.1029/2010JD014352, d24307, 2010.

Loeb, N. G., Lyman, J. M., Johnson, G. C., Allan, R. P., Doelling, D. R., Wong, T., Soden, B. J., and Stephens, G. L.: Observed changes in top-of-the-atmosphere radiation and upper-ocean heating consistent within uncertainty, Nature Geoscience, 5, 110, 2012.

López-Puertas, M. and Taylor, F.: Non-LTE Radiative Transfer in the Atmosphere, Series on atmospheric, oceanic and planetary physics, World Scientific, 2001.

Madronich, S.: Photodissociation in the atmosphere: 1. Actinic flux and the effects of ground reflections and clouds, Journal of Geophysical Research: Atmospheres, 92, 9740–9752, doi:10.1029/JD092iD08p09740, 1987.

Madronich, S. and Flocke, S.: The role of solar radiation in atmospheric chemistry, in: Environmental photochemistry, 1–26, Springer, 1999.

Mahieu, E., Chipperfield, M. P., Notholt, J., Reddmann, T., Anderson, J., Bernath, P. F., Blumenstock, T., Coffey, M. T., Dhomse, S. S., Feng, W., Franco, B., Froidevaux, L., Griffith, D. W. T., Hannigan, J. W., Hase, F., Hossaini, R., Jones, N. B., Morino, I., Murata, I., Nakajima, H., Palm, M., Paton-Walsh, C., III, J. M. R., Schneider, M., Servais, C., Smale, D., and Walker, K. A.: Recent Northern Hemisphere stratospheric HCl increase due to atmospheric circulation changes, Nature, 515, 104–107, 2014.

Maiss, M. and Levin, I.: Global increase of SF6 observed in the atmosphere, Geophysical Research Letters, 21, 569–572, doi:10.1029/94GL00179, 1994.

Matsuno, T.: A Dynamical Model of the Stratospheric Sudden Warming, Journal of the Atmospheric Sciences, 28, 1479–1494, doi:10.1175/1520-0469(1971)028<1479:ADMOTS> 2.0.CO;2, 1971.

Maycock, A. C., Joshi, M. M., Shine, K. P., Davis, S. M., and Rosenlof, K. H.: The potential impact of changes in lower stratospheric water vapour on stratospheric temperatures over the past 30 years, Quarterly Journal of the Royal Meteorological Society, 140, 2176–2185, doi:10.1002/qj.2287, 2014.

McKenna, D. S., Konopka, P., Grooß, J.-U., Günther, G., Müller, R., Spang, R., Offermann, D., and Orsolini, Y.: A new Chemical Lagrangian Model of the Stratosphere (CLaMS) 1. Formulation of advection and mixing, Journal of Geophysical Research: Atmospheres, 107, ACH 15–1–ACH 15–15, doi:10.1029/2000JD000114, 2002.

McLinden, C. A., Olsen, S. C., Hannegan, B., Wild, O., Prather, M. J., and Sundet, J.: Stratospheric ozone in 3-D models: A simple chemistry and the cross-tropopause flux, Journal of Geophysical Research: Atmospheres, 105, 14 653–14 665, doi:10.1029/ 2000JD900124, 2000.

Meador, W. E. and Weaver, W. R.: Two-Stream Approximations to Radiative Transfer in Planetary Atmospheres: A Unified Description of Existing Methods and a New Improvement, Journal of the Atmospheric Sciences, 37, 630–643, doi:10.1175/1520-0469(1980) 037<0630:TSATRT>2.0.CO;2, 1980.

Mlawer, E. J., Taubman, S. J., Brown, P. D., Iacono, M. J., and Clough, S. A.: Radiative transfer for inhomogeneous atmospheres: RRTM, a validated correlated-k model for the longwave, Journal of Geophysical Research: Atmospheres, 102, 16 663–16 682, doi: 10.1029/97JD00237, 1997.

Molina, L. T. and Molina, M. J.: Production of chlorine oxide (Cl2O2) from the self-reaction of the chlorine oxide (ClO) radical, The Journal of Physical Chemistry, 91, 433–436, doi:10.1021/j100286a035, 1987.

Monge-Sanz, B. M., Chipperfield, M. P., Simmons, A. J., and Uppala, S. M.: Mean age of air and transport in a CTM: Comparison of different ECMWF analyses, Geophysical Research Letters, 34, doi:10.1029/2006GL028515, l04801, 2007.

Mote, P. W., Rosenlof, K. H., McIntyre, M. E., Carr, E. S., Gille, J. C., Holton, J. R., Kinnersley, J. S., Pumphrey, H. C., Russell, J. M., and Waters, J. W.: An atmospheric tape recorder: The imprint of tropical tropopause temperatures on stratospheric water vapor, Journal of Geophysical Research: Atmospheres, 101, 3989–4006, doi:10.1029/95JD03422, 1996.

Nash, E. R., Newman, P. A., Rosenfield, J. E., and Schoeberl, M. R.: An objective determination of the polar vortex using Ertel's potential vorticity, Journal of Geophysical Research: Atmospheres, 101, 9471–9478, doi:10.1029/96JD00066, 1996.

Newman, P. A. and Nash, E. R.: The Unusual Southern Hemisphere Stratosphere Winter of 2002, Journal of the Atmospheric Sciences, 62, 614–628, doi:10.1175/JAS-3323.1, 2005.

NOAA: Committee on Extension to the Standard Atmosphere, U.S. Standard Atmosphere, U.S. Government Printing Office, Washington, D.C., USA, 1976.

Nowack, P. J., Luke Abraham, N., Maycock, A. C., Braesicke, P., Gregory, J. M., Joshi, M. M., Osprey, A., and Pyle, J. A.: A large ozone-circulation feedback and its implications for global warming assessments, Nature Climate Change, 5, 41, 2014.

O'Connor, F. M., Johnson, C. E., Morgenstern, O., Abraham, N. L., Braesicke, P., Dalvi, M., Folberth, G. A., Sanderson, M. G., Telford, P. J., Voulgarakis, A., Young, P. J., Zeng, G., Collins, W. J., and Pyle, J. A.: Evaluation of the new UKCA climate-composition model Part 2: The Troposphere, Geoscientific Model Development, 7, 41–91, doi:10.5194/gmd-7-41-2014, 2014.

Orphal, J.: A critical review of the absorption cross-sections of O 3 and NO 2 in the ultraviolet and visible, Journal of Photochemistry and Photobiology A: Chemistry, 157, 185–209, 2003.

Petty, G.: A first course in atmospheric radiation, Sundog Pub., 2004.

Pincus, R. and Stevens, B.: Paths to accuracy for radiation parameterizations in atmospheric models, Journal of Advances in Modeling Earth Systems, 5, 225–233, doi:10.1002/jame.20027, 2013.

Prather, M. J.: Photolysis rates in correlated overlapping cloud fields: Cloud-J 7.3c, Geoscientific Model Development, 8, 2587–2595, doi:10.5194/gmd-8-2587-2015, 2015.

Randel, W. J., Wu, F., III, J. M. R., Roche, A., and Waters, J. W.: Seasonal Cycles and QBO Variations in Stratospheric CH4 and H2O Observed in UARS HALOE Data, Journal of the Atmospheric Sciences, 55, 163–185, doi:10.1175/1520-0469(1998)055<0163: SCAQVI>2.0.CO;2, 1998.

Raschendorfer, M.: The new turbulence parameterization of LM., COSMO Newsletter, 1: 89-97, available from http://www.cosmo-model.org, 2001.

Ravishankara, A. R., Solomon, S., Turnipseed, A. A., and Warren, R. F.: Atmospheric Lifetimes of Long-Lived Halogenated Species, Science, 259, 194–199, doi:10.1126/science. 259.5092.194, 1993.

Reddmann, T., Ruhnke, R., and Kouker, W.: Three-dimensional model simulations of SF6 with mesospheric chemistry, Journal of Geophysical Research: Atmospheres, 106, 14 525–14 537, doi:10.1029/2000JD900700, 2001.

Riahi, K., Grübler, A., and Nakicenovic, N.: Scenarios of long-term socio-economic and environmental development under climate stabilization, Technological Forecasting and Social Change, 74, 887 – 935, doi:http://dx.doi.org/10.1016/j.techfore.2006.05.026, greenhouse Gases - Integrated Assessment, 2007.

Rieger, D., Bangert, M., Bischoff-Gauss, I., Förstner, J., Lundgren, K., Reinert, D., Schröter, J., Vogel, H., Zängl, G., Ruhnke, R., and Vogel, B.: ICON-ART 1.0 – a new online-coupled model system from the global to regional scale, Geoscientific Model Development, 8, 1659–1676, doi:10.5194/gmd-8-1659-2015, 2015.

Roeckner, E., Brokopf, R., Esch, M., Giorgetta, M., Hagemann, S., Kornblueh, L., Manzini, E., Schlese, U., and Schulzweida, U.: Sensitivity of Simulated Climate to Horizontal and Vertical Resolution in the ECHAM5 Atmosphere Model, Journal of Climate, 19, 3771–3791, doi:10.1175/JCLI3824.1, 2006.

Roedel, W.: Physik unserer Umwelt: Die Atmosphäre, Springer Berlin Heidelberg, 2013.

Rosenlof, K. H.: Seasonal cycle of the residual mean meridional circulation in the stratosphere, Journal of Geophysical Research: Atmospheres, 100, 5173–5191, doi: 10.1029/94JD03122, 1995.

Rosenlof, K. H. and Reid, G. C.: Trends in the temperature and water vapor content of the tropical lower stratosphere: Sea surface connection, Journal of Geophysical Research: Atmospheres, 113, doi:10.1029/2007JD009109, d06107, 2008.

Rosenlof, K. H., Oltmans, S. J., Kley, D., Russell, J. M., Chiou, E.-W., Chu, W. P., Johnson, D. G., Kelly, K. K., Michelsen, H. A., Nedoluha, G. E., Remsberg, E. E., Toon, G. C., and McCormick, M. P.: Stratospheric water vapor increases over the past half-century, Geophysical Research Letters, 28, 1195–1198, doi:10.1029/2000GL012502, 2001.

Ruggaber, A., Forkel, R., and Dlugi, R.: Spectral actinic flux and its ratio to spectral irradiance by radiation transfer calculations, Journal of Geophysical Research: Atmospheres, 98, 1151–1162, doi:10.1029/92JD02392, 1993.

Röth, E.-P.: Description of the Anisotropic Radiation Transfer Model ART to determine photodissociation coefficients, Berichte des Forschungszentrums Jülich, Jül-3960, 2002.

Sadourny, R., Arakawa, A., and Mintz, Y.: Integration of the nondivergent barotropic vorticity equation with an icosahedral-hexagonal grid for the sphere, Citeseer, 1968.

Sander, R., Baumgaertner, A., Gromov, S., Harder, H., Jöckel, P., Kerkweg, A., Kubistin, D., Regelin, E., Riede, H., Sandu, A., Taraborrelli, D., Tost, H., and Xie, Z.-Q.: The atmospheric chemistry box model CAABA/MECCA-3.0, Geoscientific Model Development, 4, 373–380, doi:10.5194/gmd-4-373-2011, 2011a.

Sander, S., Friedl, R., DeMore, W., Ravishankara, A., Golden, D., Kolb, C., Kurylo, M., Hampson, R., Huie, R., Molina, M., et al.: Chemical Kinetics and Photochemical Data for Use in Stratospheric Modeling. Supplement to Evaluation No. 12-Update of Key Reactions and Evaluation No. 13, JPL Publication 00-3, Jet Propulsion Laboratory, California Institute of Technology, Pasadena, CA, 2000.

Sander, S., Friedl, R., Barker, J., Golden, D., rylo, M., Wine, P., Abbatt, J., Burkholder, J., Kolb, C.E. d Moortgat, G., Huie, R., and Orkin, V.: Chemical kinetics and photochemical data for use in atmospheric sudies: Evaluation No. 17, JPL Publication 10–6, Jet Propulsion Laboratory, Pasadena, USA, 2011b.

Sander, S. P., Friedl, R., Golden, D., Kurylo, M., Moortgat, G., Wine, P., Ravishankara, A., Kolb, C., Molina, M., Finlayson-Pitts, B., et al.: Chemical kinetics and photochemical data for use in atmospheric studies evaluation number 15, 2006.

Sandu, A. and Sander, R.: Technical note: Simulating chemical systems in Fortran90 and Matlab with the Kinetic PreProcessor KPP-2.1, Atmospheric Chemistry and Physics, 6, 187–195, doi:10.5194/acp-6-187-2006, 2006.

Sandu, A., Verwer, J., Blom, J., Spee, E., Carmichael, G., and Potra, F.: Benchmarking stiff ode solvers for atmospheric chemistry problems II: Rosenbrock solvers, Atmospheric Environment, 31, 3459 – 3472, doi:http://dx.doi.org/10.1016/S1352-2310(97)83212-8, 1997.

Santer, B. D., Painter, J. F., Mears, C. A., Doutriaux, C., Caldwell, P., Arblaster, J. M., Cameron-Smith, P. J., Gillett, N. P., Gleckler, P. J., Lanzante, J., Perlwitz, J., Solomon, S., Stott, P. A., Taylor, K. E., Terray, L., Thorne, P. W., Wehner, M. F., Wentz, F. J., Wigley, T. M. L., Wilcox, L. J., and Zou, C.-Z.: Identifying human influences on atmospheric temperature, Proceedings of the National Academy of Sciences, 110, 26–33, doi:10.1073/pnas.1210514109, 2013.

Schmidt, U. and Khedim, A.: In situ measurements of carbon dioxide in the winter Arctic vortex and at midlatitudes: An indicator of the 'age' of stratopheric air, Geophysical Research Letters, 18, 763–766, doi:10.1029/91GL00022, 1991.

Schoeberl, M. R., Dessler, A. E., and Wang, T.: Simulation of stratospheric water vapor and trends using three reanalyses, Atmospheric Chemistry and Physics, 12, 6475–6487, doi:10.5194/acp-12-6475-2012, 2012.

Schröter, J., Rieger, D., Stassen, C., Vogel, H., Weimer, M., Werchner, S., Förstner, J., Prill, F., Reinert, D., Zängl, G., Giorgetta, M., Ruhnke, R., Vogel, B., and Braesicke, P.: ICON-ART 2.1 – A flexible tracer framework and its application for composition studies in numerical weather forecasting and climate simulations, Geoscientific Model Development Discussions, 2018, 1–37, doi:10.5194/gmd-2017-286, 2018.

Schumann, U.: Atmospheric Physics: Background – Methods – Trends, Research Topics in Aerospace, Springer Berlin Heidelberg, 2012.

Schär, C., Leuenberger, D., Fuhrer, O., Lüthi, D., and Girard, C.: A New Terrain-Following Vertical Coordinate Formulation for Atmospheric Prediction Models, Monthly Weather Review, 130, 2459–2480, doi:10.1175/1520-0493(2002)130<2459:ANTFVC>2.0.CO;2, 2002.

Scott, D. W.: On optimal and data-based histograms, Biometrika, 66, 605–610, doi:10.1093/biomet/66.3.605, 1979.

Seinfeld, J. and Pandis, S.: Atmospheric Chemistry and Physics: From Air Pollution to Climate Change, A Wiley-Interscience publication, Wiley, Hoboken, New Jersey, 2006.

Shine, K. P., Cook, J., Highwood, E. J., and Joshi, M. M.: An alternative to radiative forcing for estimating the relative importance of climate change mechanisms, Geophysical Research Letters, 30, doi:10.1029/2003GL018141, 2047, 2003.

Simmons, A. J., Untch, A., Jakob, C., Kållberg, P., and Undén, P.: Stratospheric water vapour and tropical tropopause temperatures in Ecmwf analyses and multi-year simulations, Quarterly Journal of the Royal Meteorological Society, 125, 353–386, doi:10.1002/qj.49712555318, 1999.

Sinnhuber, B.-M., Weber, M., Amankwah, A., and Burrows, J. P.: Total ozone during the unusual Antarctic winter of 2002, Geophysical Research Letters, 30, doi:10.1029/2002GL016798, 1580, 2003.

Solomon, S., Young, P. J., and Hassler, B.: Uncertainties in the evolution of stratospheric ozone and implications for recent temperature changes in the tropical lower stratosphere, Geophysical Research Letters, 39, doi:10.1029/2012GL052723, l17706, 2012.

Stamnes, K., Tsay, S.-C., and Nakajima, T.: Computation of eigenvalues and eigenvectors for the discrete ordinate and matrix operator methods in radiative transfer, Journal of Quantitative Spectroscopy and Radiative Transfer, 39, 415 – 419, doi:http://dx.doi.org/10.1016/0022-4073(88)90107-0, 1988.

Staniforth, A. and Thuburn, J.: Horizontal grids for global weather and climate prediction models: a review, Quarterly Journal of the Royal Meteorological Society, 138, 1–26, doi:10.1002/qj.958, 2012.

Stenchikov, G., Hamilton, K., Robock, A., Ramaswamy, V., and Schwarzkopf, M. D.: Arctic oscillation response to the 1991 Pinatubo eruption in the SKYHI general circulation model with a realistic quasi-biennial oscillation, Journal of Geophysical Research: Atmospheres, 109, doi:10.1029/2003JD003699, d03112, 2004.

Stenchikov, G., Delworth, T. L., Ramaswamy, V., Stouffer, R. J., Wittenberg, A., and Zeng, F.: Volcanic signals in oceans, Journal of Geophysical Research: Atmospheres, 114, doi:10.1029/2008JD011673, d16104, 2009.

Stenchikov, G. L., Kirchner, I., Robock, A., Graf, H.-F., Antuña, J. C., Grainger, R. G., Lambert, A., and Thomason, L.: Radiative forcing from the 1991 Mount Pinatubo volcanic eruption, Journal of Geophysical Research: Atmospheres, 103, 13 837–13 857, doi:10.1029/98JD00693, 1998.

Stephens, G. L., Li, J., Wild, M., Clayson, C. A., Loeb, N., Kato, S., L'Ecuyer, T., Stackhouse Jr, P. W., Lebsock, M., and Andrews, T.: An update on Earth's energy balance in light of the latest global observations, Nature Geoscience, 5, 691, 2012.

Stiller, G. P., von Clarmann, T., Haenel, F., Funke, B., Glatthor, N., Grabowski, U., Kellmann, S., Kiefer, M., Linden, A., Lossow, S., and López-Puertas, M.: Observed temporal evolution of global mean age of stratospheric air for the 2002 to 2010 period, Atmospheric Chemistry and Physics, 12, 3311–3331, doi:10.5194/acp-12-3311-2012, 2012.

Taylor, K. E., Williamson, D., and Zwiers, F.: The sea surface temperature and sea-ice concentration boundary conditions for AMIP II simulations, Program for Climate Model

Diagnosis and Intercomparison, Lawrence Livermore National Laboratory, University of California, 2000.

Taylor, K. E., Stouffer, R. J., and Meehl, G. A.: An Overview of CMIP5 and the Experiment Design, Bulletin of the American Meteorological Society, 93, 485–498, doi:10.1175/BAMS-D-11-00094.1, 2012.

Telford, P. J., Abraham, N. L., Archibald, A. T., Braesicke, P., Dalvi, M., Morgenstern, O., O'Connor, F. M., Richards, N. A. D., and Pyle, J. A.: Implementation of the Fast-JX Photolysis scheme (v6.4) into the UKCA component of the MetUM chemistry-climate model (v7.3), Geoscientific Model Development, 6, 161–177, doi:10.5194/gmd-6-161-2013, 2013.

Thompson, A. M.: The effect of clouds on photolysis rates and ozone formation in the unpolluted troposphere, Journal of Geophysical Research: Atmospheres, 89, 1341–1349, doi:10.1029/JD089iD01p01341, 1984.

Tie, X., Madronich, S., Walters, S., Zhang, R., Rasch, P., and Collins, W.: Effect of clouds on photolysis and oxidants in the troposphere, Journal of Geophysical Research: Atmospheres, 108, doi:10.1029/2003JD003659, 4642, 2003.

TOMS Science Team: TOMS Earth-Probe Total Ozone (O3) Aerosol Index UV-Reflectivity UV-B Erythemal Irradiance Daily L3 Global 1 deg x 1.25 deg V008 Greenbelt, MD, Goddard Earth Sciences Data and Information Services Center (GES DISC), 2016.

Trenberth, K. E., Fasullo, J. T., and Kiehl, J.: Earth's Global Energy Budget, Bulletin of the American Meteorological Society, 90, 311–323, doi:10.1175/2008BAMS2634.1, 2009.

van Weele, M. and Duynkerke, P. G.: Effect of clouds on the photodissociation of NO2: Observations and modelling, Journal of Atmospheric Chemistry, 16, 231–255, doi:10.1007/BF00696898, 1993.

Vilà-Guerau de Arellano, J., Duynkerke, P. G., and van Weele, M.: Tethered-balloon measurements of actinic flux in a cloud-capped marine boundary layer, Journal of Geophysical Research: Atmospheres, 99, 3699–3705, doi:10.1029/93JD03090, 1994.

Wahner, A. and Moortgat, G.: Die Atmosphäre als photochemischer Reaktor, Chemie in unserer Zeit, 41, 192–198, doi:10.1002/ciuz.200700429, 2007.

Wan, H., Giorgetta, M. A., Zängl, G., Restelli, M., Majewski, D., Bonaventura, L., Fröhlich, K., Reinert, D., Rípodas, P., Kornblueh, L., and Förstner, J.: The ICON-1.2 hydrostatic atmospheric dynamical core on triangular grids â€" Part 1: Formulation

and performance of the baseline version, Geoscientific Model Development, 6, 735–763, doi:10.5194/gmd-6-735-2013, 2013.

Waugh, D. W. and Randel, W. J.: Climatology of Arctic and Antarctic Polar Vortices Using Elliptical Diagnostics, Journal of the Atmospheric Sciences, 56, 1594–1613, doi: 10.1175/1520-0469(1999)056<1594:COAAAP>2.0.CO;2, 1999.

Weimer, M., Schröter, J., Eckstein, J., Deetz, K., Neumaier, M., Fischbeck, G., Hu, L., Millet, D. B., Rieger, D., Vogel, H., Vogel, B., Reddmann, T., Kirner, O., Ruhnke, R., and Braesicke, P.: An emission module for ICON-ART 2.0: implementation and simulations of acetone, Geoscientific Model Development, 10, 2471–2494, doi:10.5194/gmd-10-2471-2017, 2017.

Wild, O., Zhu, X., and Prather, M.: Fast-J: Accurate Simulation of In- and Below-Cloud Photolysis in Tropospheric Chemical Models, Journal of Atmospheric Chemistry, 37, 245–282, doi:10.1023/A:1006415919030, 2000.

Zängl, G., Reinert, D., Rípodas, P., and Baldauf, M.: The ICON (ICOsahedral Non-hydrostatic) modelling framework of DWD and MPI-M: Description of the non-hydrostatic dynamical core, Quarterly Journal of the Royal Meteorological Society, 141, 563–579, doi:10.1002/qj.2378, 2015.

List of Figures

List of Tables

List of Acronyms

ICON   ICOsahedral Non-hydrostatic modelling framework

ART   Aerosols and Reactive Trace gases

ECHAM   EC(MWF)HAM(burg)

ERA   European Reanalysis

AMIP   Atmospheric Model Intercomparison Project

DWD   German Weather Service

SLEVE   Smooth Level Vertical

GME   Global Model Europa

COSMO   Consortium for Small-scale Modelling

ECMWF   European Centre for Medium-Range Weather Forecasts

TUV   Tropospheric and Ultraviolet and visible radiation model

RRTMG   Rapid-Radiative-Transfer-Model for General Circulation Model

GCM   General Circulation Model

TORERO   Tropical Ocean tRoposphere Exchange of reactive halogen species and Oxygenated VOC

VOC   Volatile organic compounds

GV-HIAPER   Gulfstream-V High-performance Instrumented Airborne Platform for Environmental Research

UTLS   Upper Troposphere Lower Stratosphere

MetUM   Met Office Unified Model

MLS   Microwave Limb Sounder

MERRA   Modern-Era Retrospective Analysis for research and Applications

IFS   Integrated Forecasting System

RMSE   Root Mean Square Error

SZA   Solar Zenith Angle

Acknowledgements

In der schwersten Zeit habe ich viel Verständnis, Unterstützung und Zusammenhalt von meiner Familie und Freunden erhalten. Einen sehr großen Teil des akademischen Weges bin ich mit dir, Dr. Matthäus Kiel gegangen. So viele Seiten beginnend bei Berichten zum physikalischen Praktikum bis hin zur letzten Seite meiner Dissertation hast du mir korrigiert. Danke für die vielen Jahre der Unterstützung und Geduld in vielen Lebenslagen. Danke, dass ich diese Zeit mit Dir verbringen durfte.

Uğur Çayoğlu, ich danke dir nicht nur für das Korrekturlesen, sondern auch für viel Unterstützung und die Zeit während und neben der Arbeit. Am Ende danke ich auch Dir, Johannes Goetze für ein immer offenes Ohr und eine lange gute Freundschaft.